SPECTRAL/HP LEAST-SQUARES FINITE ELEMENT ANALYSIS OF ISOTHERMAL AND NON-ISOTHERMAL FLOWS OF GENERALIZED NEWTONIAN FLUIDS

A Dissertation

by

NAMHEE KIM

Submitted to the Office of Graduate and Professional Studies of
Texas A&M University
in partial fulfillment of the requirements for the degree of

DOCTOR OF PHILOSOPHY

Chair of Committee,	J. N. Reddy
Committee Members,	Jean-Luc Guermond
	Alan Palazzolo
	Meinhard T. Schobeiri
Head of Department,	Andreas A. Polycarpou

May 2019

Major Subject: Mechanical Engineering

ABSTRACT

Mixed least-squares finite element models with spectral/hp approximations were developed for steady, incompressible, isothermal and non-isothermal flows of generalized-Newtonian fluids obeying the Carreau–Yasuda viscosity model. The finite element model for isothermal flows consists of velocity, pressure, and stress fields as independent variables, and the model for non-isothermal flows consists of temperature and heat flux in addition to the three fields. (hence, called a mixed model). Least-squares models offer an alternative variational setting to the conventional weak-form Galerkin models for the Navier–Stokes equations, and no compatibility conditions on the approximation spaces are necessary when the polynomial order (p) used is sufficiently high (say, $\mathrm{p} > 3$, as determined numerically). Also, the use of the high-order spectral/hp elements in conjunction with a least-squares formulation alleviates various forms of locking which often appear in low-order least-squares finite element models for incompressible viscous fluids, and accurate results can be obtained with exponential convergence. To verify and validate the present model, various benchmark problems of two- and three-dimensional flows are solved. In addition, the effect of different parameters of the Carreau–Yasuda constitutive model on the flow characteristics are studied parametrically.

DEDICATION

To God and my family and my advisor.

ACKNOWLEDGMENTS

I would like to express my sincere gratitude to my advisor Professor J. N. Reddy who has supported me academically and financially during my Ph.D. course at Texas A&M University. He is an excellent teacher who teaches the finite element method (FEM) with great passion, and it is through his courses and his text books that I have learned FEM. His extraordinary ability to teach difficult and challenging concepts in a very clear way enabled me to understand the course contents easily and motivated me to learn. His courses set the foundation for my doctoral research and gave me confidence that I can develop finite element models for various engineering problems. He is also a great advisor and mentor, who guided me with inspiration, encouragement, and patience to perform research for this dissertation topic that he chose for me. Before I took his courses, he accepted me as his graduate student, even though I had no experience with the FEM. Since I was not prepared for conducting research on FEM, I wanted to take both linear and nonlinear FEM courses at the same time. However, he urged me to take his courses sequentially, first linear and then nonlinear FEM. I am very grateful that he guided me to do so, because his nonlinear FEM course was very intensive and required computer programming which I was not familiar with at that time. When I was afraid to carry out research before taking the basic courses of FEM, he gave me courage with strong impression by saying "I understand." Then I started to study by modifying his former graduate student's computer code which was built upon his own finite element programs. After spending much time to be familiar with the computer code, I could obtain some numerical results from which we wrote our first manuscript for a journal publication. When I wrote and sent him a draft, he revised the draft with great care so that I could learn from him how to write a research paper with better quality. It was rare and precious experience for me. In addition to his excellence in teaching and mentoring, he is a very kind, thoughtful, and humble person. He often invited his graduate students for lunch or dinner, talking and sharing his photos that he took during his travels, making us all feel free and comfortable. In August 2015, the Department of Mechanical Engineering of Texas A&M University held a wonderful banquet for Professor Reddy to celebrate

him for being elected as a member of the National Academy of Engineering. He invited all of his former and current students although he could not invite his other acquaintances due to the limited space. In the beginning of the banquet, he introduced all of his graduate students to the guests through his presentation with his students' photos. Whenever he gives his research presentations in various places, he never forgets to introduce his students who worked with him and always says that he has been learning by working together with his students. I believe that he has been and is a role model to many student who has taken his courses, his own students, and those who came in contact with him professionally. I am very glad and very fortunate to have worked with Professor Reddy.

I would like to thank my dissertation committee members: Professor Alan Palazzolo, Professor M. T. Schobeiri, and Professor Jean-Luc Guermond who provided me with helpful advice and encouragement on my research. I am very grateful to Professor Palazzolo who helped me greatly when I was not in good health.

The numerical studies presented in this dissertation were performed using computing resources of Advanced Computational Mechanics Laboratory (ACML) and of High Performance Research Computing (HPRC) at Texas A&M University. My special thanks go to Dr. Michael Powell who managed ACML cluster and helped our ACML group members run their computer codes on it and also to Mr. Marinus Pennings who helped me run my computer code on HPRC's Ada cluster.

I am sincerely grateful to my lovely mother and father for their love, sacrifice, prayer, support, and encouragement. I owe them everything that I am now and this is not enough to express my gratitude for them. I must also thank to my two lovely sisters: Jayoung and Yanghee for their love and encouragement.

I would like to thank to Fathers at St. Mary's Catholic Center (College Station, TX) for their spiritual encouragement and prayers.

I am truly grateful to God who created the heavens and the earth (Genesis 1:1) and gave life to me. He pardons all my sins, and heals all my ills, redeems my life from the pit, and crowns me with mercy and compassion (Psalms 103:3-4).

CONTRIBUTORS AND FUNDING SOURCES

Contributors

This work was supported by a dissertation committee consisting of Professor J. N. Reddy and Professor Alan Palazzolo and Professor Meinhard T. Schobeiri of the Department of Mechanical Engineering and Professor Jean-Luc Guermond of the Department of Mathematics.

All other work conducted for the dissertation was completed by the student independently.

Funding Sources

Graduate study was supported by the Department of Defense (DoD) Award: SC130156 (W81XWH-14-1-0600) and the Oscar S. Wyatt Endowed Chair as well as the Aruna and J. N. Reddy Distinguished Fellow in Computational Mechanics and Charles Crawford '19 Fellowship from the Department of Mechanical Engineering at Texas A&M University.

TABLE OF CONTENTS

Page

LIST OF FIGURES

FIGURE Page

LIST OF TABLES

TABLE Page

1. INTRODUCTION *

1.1 Background

It is well known that the finite element method (FEM) is a general and powerful numerical procedure to analyze practical problems where complicate geometries, boundary conditions, nonlinearities, and/or coupled phenomena arise [3, 4]. Among the various types of finite element models, the weak-form Galerkin approach has been proven to be successful in the field of solid and structural mechanics, mainly due to its ideal setting for the finite element approximation which often referred to as *variational setting*. When the weak forms of governing differential equations are equivalent to the minimization of a quadratic functional, the finite element solutions are an orthogonal projection of the exact solution onto the trial space of a finite element discretization. The resulting numerical solution represents the best possible approximation of the exact solution as measured with the energy norm of the functional. Restrictive compatibility conditions between approximation spaces are not required and the linear algebraic system of finite element equations is symmetric positive-definite. Such a setting is called a *variational setting* and is ideal for finite element approximation [4, 5]. However, weak-form Galerkin finite element models often depart from this ideal setting when applied to the problems whose weak forms cannot be obtained through the minimization of a quadratic functional. In order to recover the favorable features of the variational setting for such problems, there has been a considerable amount of works for the modified Galerkin procedures such as SUPG [6, 7], penalty [8, 9], Galerkin least-squares [10], and so on. However, when these modified Galerkin approaches are applied to the governing equations having non-self-adjoint operators such as the Navier–Stokes equations, they are generally not the best approximation and do not lead to symmetric positive-definite coefficient matrices [5].

Another way to recover most of the features of variational setting is the least-squares based for-

mulation. In a least-square formulation, the sum of the squared norms of the residuals of governing equations are minimized. The finite element model obtained from least-squares formulation for any boundary-value problem is in a setting of unconstrained functional minimization, which is the variational setting [5]. Due to this, the finite element method based on least-squares formulation has been actively studied since the early 1970's and is known as an alternative way to the conventional weak-form Glaerkin finite element models especially in the analysis of non-self-adjoint problems as in fluid mechanics [11]. For the Navier–Stokes equations, least-squares finite element models offer theoretical and computational advantages over the conventional weak-form Galerkin finite element models. A least-squares finite element model (LSFEM) provides a variational framework for the Navier–Stokes equations, which have no underlying extremum variational principles, leading to a minimization problem. Since the formulation does not lead to the saddle-point structure of a problem, no compatibility conditions (known as inf-sup or Ladyzhenskaya–Babuska–Brezzi (LBB) condition), which force the use of different order approximation functions for different types of variables, are required. Therefore, the same but high-order interpolation functions can be used so that different variables have the possibility to adjust their respective orders to satisfy the interrelationship between them. On the contrary, the weak-form Galerkin finite element approach for the solution of the Navier–Stokes equations has a saddle-point behavior and the velocity and pressure approximations, especially lower order, are required, in general, to satisfy inf-sup condition. In other words, if one applies equal but lower-order approximations to all variables, the differential relationship between the variables is naturally violated, which may cause oscillations in the numerical solutions. These oscillations can be alleviated if high-order interpolation functions for all variables are used so that the differential relationship is satisfied. In addition, LSFEM does not require numerical diffusion (e.g., through the use of upwind schemes) which weak-form Galerkin formulations often need when applied to the Navier–Stokes equations. For linear partial differential equations, LSFEM always leads to symmetric positive-definite (SPD) coefficient matrices, regardless of symmetry in the governing equations. This makes it possible to use efficient iterative or direct solvers. Due to this feature, many researchers linearize their governing equations

prior to the minimization of the least-squares functional. [9, 12–14].

LSFEMs also have some deficiencies. Many engineering problems are governed by at least second-order spatial differential equations. Least-squares finite element models for such problems require higher regularity of the approximate solution than the weak-form Galerkin finite element models do, which negatively affects the conditioning of the coefficient matrix and the number of iterations for convergence of an iterative solution. This higher regularity can be avoided by recasting the governing equations into an equivalent lower-order system by introducing auxiliary variables. For the Navier–Stokes equations which are the second-order differential equations, we can reduce the order of the differentiability of the approximation functions in the least-squares finite element model by re-writing them as a set of equivalent first-order equations though the use of auxiliary variables such as vorticity, stresses, dilatation, or velocity gradient. By doing this, there is no need to use C^1-continuous functions for the velocity field which could be perceived as a practical disadvantage [4, 5, 15–34]. Although the size of the global system of equations is increased, this formulation is advantageous in that auxiliary variables often represent important physical quantities such as stress and vorticity [4, 13]. Other deficiency of least-squares models is that it is weak in local mass conservation for both steady and unsteady flow problems and poor in coupling between the velocity and pressure for unsteady flow problems [4, 5, 35, 36]. For transient flow problems, the poor coupling of velocity and pressure weakens the local mass conservations and causes instability in the finite element simulations [24]. Several works have been carried out to enhance the local mass conservation and the coupling of velocity and pressure. Deang and Gunzburger [37] weighted the residual of the continuity equation in the least-squares functional and Chang and Nelson [35] combined the Lagrange multipliers with the least-squares method in order to exactly enforce element-level mass conservation. Also, Pontaza [24] showed that higher polynomial order of approximation functions promises better mass conservation. Pontaza [38] demonstrated that a regularized form of the continuity equation in the least-squares formulation brings strong velocity-pressure coupling and as a result enhances the local mass conservation. Heys et al. [39] reformulated a least-squares functional based on a new first-order system of the Navier-

Stokes equations, where the mass conservation is improved by increasing the pressure-velocity coupling. The iterative penalty least-squares formulations proposed by Prabhakar and Reddy [30] and Prabhakar, Pontaza, and Reddy [31] and the modified unconstrained least-squares formulation equipped with normalized volumetric flow imbalance by Payette [5] also showed improvement in both mass conservation and velocity-pressure coupling.

For the least-squares formulations which are not $H^1(\Omega)$-norm equivalent in terms of the relevant a priori estimate [13, 14, 40] (where $H^1(\Omega)$ is a Sobolev space of order 1 on a domain Ω), least-squares finite element models with low-order approximations tend to lock when the coefficient matrices are evaluated using full integration. Jiang and coworkers [15, 16, 20] demonstrated that such problems may be averted for Navier–Stokes equations using selective reduced integration methods. In a different manner, the appropriate minimization of the least-square functional can be carried out by applying high-order approximations. Jiang and Sonnad [18], Bell and Surana [41, 42], Surana and Sandhu [43], Proot and Gerritsma [21, 22, 28], Pontaza and Reddy [23, 24], Pontaza, et al. [25], Prabhakar and Reddy [27, 30], Prabhakar, Pontaza, and Reddy [31], Payette and Reddy [32], Vallala, Sadr, and Reddy [34], and Kim and Reddy [44] showed numerically that hp-least-squares finite element models are able to give accurate results even when the least-squares functional is not H^1-norm equivalent in terms of the relevant a priori estimate [13, 14, 40].

The traditional high-order Lagrange interpolation functions (with equally-spaced nodes) tend to suffer from more oscillations, known as *Runge's phenomenon*, near the end points of the interval as the polynomial order goes beyond 4. For example, Figure 1.1 shows the one-dimensional C^0 Lagrange basis with equally-spaced nodes and spectral nodal basis (which is the Lagrange interpolation function with unequally-spaced nodes) having the common node at $\xi = 0$. As the polynomial order p of the traditional Lagrange interpolation functions is increased, they show more oscillations near the edges of the interval $-1 \leq \xi \leq 1$, which results in inaccurate solutions. On the other hand, the finite element models with spectral nodal interpolation functions are known to be accurate and exhibit exponential convergence [45–47]. The spectral interpolation functions are free of the *Runge's phenomenon*, as depicted in Figure 1.1. Thus, the finite element coefficient matrices

formulated with spectral basis functions are better conditioned, which makes them yield accurate results [5, 33]. Pontaza and Reddy [23, 24], Prabhakar and Reddy [27, 30], Payette and Reddy [32], Vallala, Sadr, and Reddy [34] and Kim and Reddy [44] employed spectral/hp approximations in the least-squares finite element models for the Navier–Stokes equations and demonstrated exponential decay (spectral convergence) of the L_2 least-squares functionals as the polynomial order of approximation functions increases, using the Kovasznay flow solution, a manufactured closed-form solution to the unsteady Navier–Stokes equations, and using other benchmark problems.

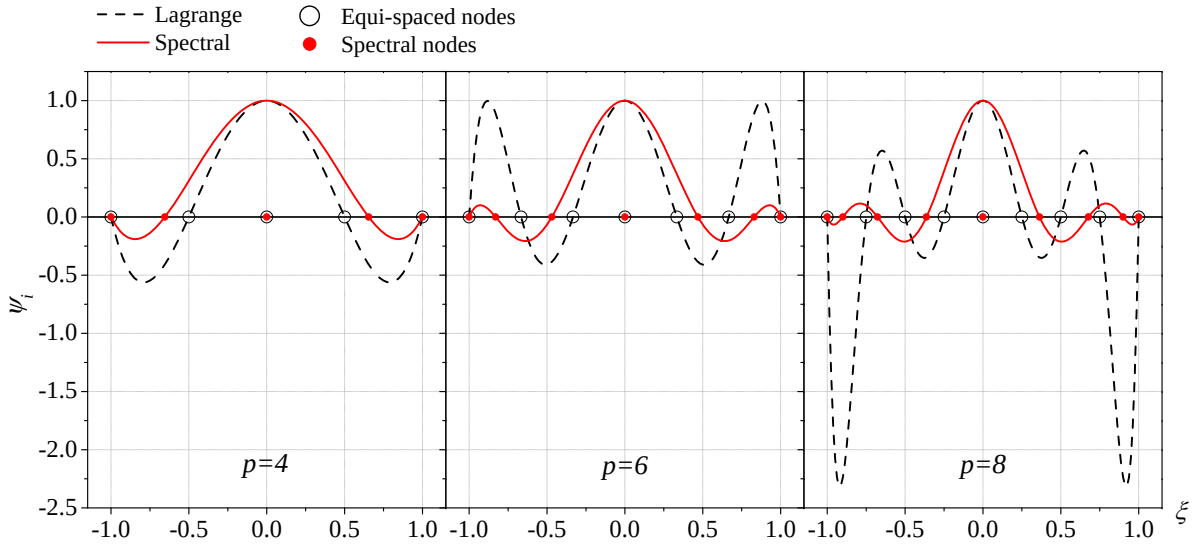

Figure 1.1: One-dimensional C^0 Lagrange interpolation functions ψ_i of $p = 4, 6,$ and 8, with equal and unequal nodal spacing having the common node at $\xi_i = 0$. The index i of ψ_i is equal to 3, 4, and 5 for $p = 4, 6, 8$, respectively.

1.2 Motivation and scope of the present study

As discussed previously, for the Navier–Stokes equations the least-squares finite element models with sufficiently high-order spectral/hp approximations have advantages over the conventional weak-form Galerkin finite element models in that they do not require compatibility restrictions between the approximation spaces, can avoid any type of locking, and yield accurate results with spectral convergence. Encouraged by these attractive features of the high-order spectral/hp least-

squares finite element models for the Navier–Stokes equations and by the previous works, the object of the current study is to develop least-squares finite element models with spectral/hp approximations for steady isothermal and non-isothermal flows of non-Newtonian fluids. In order to lower the order of differentiability of the approximation functions for the finite element models, the governing equations are re-written into the equivalent first-order system of equations by introducing the viscous stress and heat flux as auxiliary variables. Fluids can be classified into Newtonian and non-Newtonian fluids in terms of constitutive behavior. Newtonian fluids have linear relationship between shear stress and shear rate, that is, constant viscosity at given temperature and pressure such as air and water. Non-Newtonian fluids have non-linear relationship between shear stress and shear rate. Most fluids in our lives are non-Newtonian fluids and they can be categorized into generalized Newtonian fluids and viscoelastic fluids. Generalized Newtonian fluids, also called inelastic fluids, exhibit a shear rate dependent viscosity, while the motion of viscoelastic fluids depends on the deformation history of fluids in addition to the present stress state [9]. We studied generalized Newtonian fluids in the present research. Generalized Newtonian fluids can be subdivided into three types in terms of the relation between shear stress and shear rate [1]. The slope of a shear stress curve with respect to shear rate is called viscosity. For shear-thinning fluids, the viscosity decreases with increasing shear rate. Shear-thickening fluids have increasing viscosity as shear rate increases. Viscoplastic fluids have yield stress. When applied stress is below the yield stress no motion occurs, but when the stress exceeds the yield stress they flow either as Newtonian or as shear-thinning fluids. Among the three types, shear-thinning fluid is considered for this study. Common viscosity models for shear-thinning fluids include the Power-law model, Cross model, Carreau–Yasuda model and so on. Carreau–Yasuda model has more general form with five fitting parameters which are determined by experiment. The model is widely used to simulate the flows of polymer melts [48–54] and blood [55–59]. Due to its applicability and generalized form, Carreau–Yasuda model is used for our viscosity model. Although we chose the specific viscosity model, our finite element code is generic in that it is able to simulate other kinds of generalized Newtonian fluids having different viscosity models with slight modification of the code.

The contribution of the current study is novel and significant in the following four respects:

1. Mixed least-squares finite element models for three-dimensional, steady, isothermal and non-isothermal flows of Carreau–Yasuda fluids are developed (since the finite element models consist of field variables of different kinds of units, they are often termed as “mixed" formulations).

2. Spectral approximation functions are used to avoid locking.

3. Verification and validation results are included.

4. Two-dimensional and three-dimensional numerical studies are presented to bring out the parametric effects of the various parameters in the Carreau–Yasuda constitutive model.

The dissertation is organized as follows. From Section 2 to 4, we describe the steps involved in developing the least-squares finite element models with spectral/hp approximations for isothermal and non-isothermal flows of Carreau–Yasuda fluids (the governing equations in Section 2, the least-squares formulations in Section 3, and the finite element models in Section 4). In Section 5, we present the two-dimensional and three-dimensional numerical examples using several benchmark problems. For two-dimensional problems, Kovasznay flow, Jeffery-Hamel flow in a diverging channel, flow over a backward-facing step, flow in a lid-driven square cavity, flow past an unconfined circular cylinder, and fully-developed flow between parallel plates are considered. For three-dimensional problems, flow in a lid-driven cubic cavity, flow over a backward-facing step, and buoyancy-driven flow in a cubic cavity are considered. The numerical results of the present study are compared with the analytical, experimental, and numerical results of previous works available in literature. In addition, the parametric studies of the Carreua–Yasuda model are performed. In Section 6, we give concluding remarks.

2. GOVERNING EQUATIONS*

2.1 Isothermal generalized Newtonian flows

We consider steady, incompressible, isothermal flow of generalized Newtonian fluids in this section, and non-isothermal case in Section 2.2. A steady, incompressible, and isothermal flow of generalized Newtonian fluids is governed by Eq. (2.2) which are obtained by non-dimensionalizing the equations for conservation of mass and momentum using the following dimensionless variables [13, 60–63]:

$$\mathbf{x} = \frac{\hat{\mathbf{x}}}{L_0}, \quad \mathbf{v} = \frac{\hat{\mathbf{v}}}{v_0}, \quad p = \frac{\hat{p}}{\rho_0 {v_0}^2}, \tag{2.1}$$

where $\mathbf{x}$, $\mathbf{v}$ and p are the dimensionless coordinates, velocity vector and pressure, respectively, and the hat symbol denotes their physical counterparts. L_0, v_0, and ρ_0 are the reference length, velocity, and density, respectively.

$$\boldsymbol{\nabla} \cdot \mathbf{v} = 0 \qquad \text{in } \Omega \tag{2.2a}$$

$$\mathbf{v} \cdot \boldsymbol{\nabla}\mathbf{v} + \boldsymbol{\nabla} p - \boldsymbol{\nabla} \cdot \left[\mu(I_2)\left(\boldsymbol{\nabla}\mathbf{v} + \boldsymbol{\nabla}\mathbf{v}^{\mathrm{T}}\right)\right] = \mathbf{f} \qquad \text{in } \Omega \tag{2.2b}$$

The Navier–Stokes equations (Eq. (2.2b)) can be recast into the equivalent first-order form, Eq. (2.3b)–(2.3c), by introducing the viscous stress tensor $\underline{\boldsymbol{\tau}}$ as an auxiliary variable. This allows us to

*Reprinted with permission from "A spectral/hp least-squares finite element analysis of the Carreau–Yasuda fluids," by Namhee Kim and J. N. Reddy, 2016. International Journal for Numerical Methods in Fluids, Vol. 82, pp. 541–566. Copyright 2016 by John Wiley & Sons, Ltd.

use C^0 basis functions in the numerical implementation (see Reddy [4, 64]):

$$\boldsymbol{\nabla} \cdot \mathbf{v} = 0 \qquad \text{in } \Omega \tag{2.3a}$$

$$\mathbf{v} \cdot \boldsymbol{\nabla}\mathbf{v} + \boldsymbol{\nabla} p - \boldsymbol{\nabla} \cdot \underline{\boldsymbol{\tau}} = \mathbf{f} \qquad \text{in } \Omega \tag{2.3b}$$

$$\underline{\boldsymbol{\tau}} = \mu(I_2)\left(\boldsymbol{\nabla}\mathbf{v} + \boldsymbol{\nabla}\mathbf{v}^{\mathrm{T}}\right) \qquad \text{in } \Omega \tag{2.3c}$$

$$\mathbf{v} = \mathbf{v}^{\mathrm{s}} \qquad \text{on } \Gamma_v \tag{2.3d}$$

$$\hat{\mathbf{n}} \cdot \underline{\boldsymbol{\sigma}} = \mathbf{t}^{\mathrm{s}} \qquad \text{on } \Gamma_t, \tag{2.3e}$$

where $\boldsymbol{\nabla}$ is the vector differential operator, $\mathbf{v}$ is the velocity vector, p is the pressure, $\underline{\boldsymbol{\tau}}$ is the viscous stress tensor, $\mathbf{f}$ is the body force vector, $\mu(I_2)$ is the shear-rate dependent viscosity, $\underline{\boldsymbol{\sigma}}$ is the total stress tensor, and $\hat{\mathbf{n}}$ is the outward unit normal vector. $\mathbf{v}^{\mathrm{s}}$ and $\mathbf{t}^{\mathrm{s}}$ are the specified velocity on the boundary Γ_v and the specified traction on the boundary Γ_t, respectively. Γ is the total boundary enclosing the fluid domain Ω satisfying $\Gamma = \Gamma_v \cup \Gamma_t$ and $\emptyset = \Gamma_v \cap \Gamma_t$. For a generalized Newtonian fluid, the constitutive equation takes the form of Eq. (2.4)

$$\underline{\boldsymbol{\sigma}} = -p\underline{\mathbf{I}} + \underline{\boldsymbol{\tau}} = -p\underline{\mathbf{I}} + \mu(I_2)\left(\boldsymbol{\nabla}\mathbf{v} + \boldsymbol{\nabla}\mathbf{v}^{\mathrm{T}}\right). \tag{2.4}$$

We choose the Carreau–Yasuda model as the viscosity model which describes the fluid rheology as (in a dimensionless form)

$$\mu(I_2) = \frac{1}{\mathrm{Re}}\left[\mu_\infty + (\mu_0 - \mu_\infty)\left\{1 + \left(\lambda_{CY}\, {I_2}^{\frac{1}{2}}\right)^a\right\}^{\frac{n-1}{a}}\right]. \tag{2.5}$$

Here, I_2 is the second invariant of the tensor $\underline{\mathbf{A}}$ which is equal to twice the rate-of-strain tensor $\underline{\mathbf{D}} = \frac{1}{2}\left(\boldsymbol{\nabla}\mathbf{v} + \boldsymbol{\nabla}\mathbf{v}^{\mathrm{T}}\right)$.

$$I_2 = \frac{1}{2} tr\left(\underline{\mathbf{A}}^2\right) = \frac{1}{2}\sum_i \sum_j A_{ij} A_{ji}, \quad \underline{\mathbf{A}} = 2\underline{\mathbf{D}} = \boldsymbol{\nabla}\mathbf{v} + \boldsymbol{\nabla}\mathbf{v}^{\mathrm{T}}, \tag{2.6}$$

where tr denotes the trace. ${I_2}^{1/2}$ appearing in Eq. (2.5) is called the shear rate

$$ {I_2}^{\frac{1}{2}} = \sqrt{\frac{1}{2}\sum_i \sum_j A_{ij} A_{ji}}. \tag{2.7} $$

So, it is said that generalized Newtonian fluids have shear-rate dependent viscosity. The Carreau–Yasuda model, Eq. (2.5), is an empirical viscosity model having five parameters, (namely, μ_0, μ_∞, λ_{CY}, a, and n) which are fitted to experimental data. Equation (2.5) does not yield analytical solutions [65]. Figure 2.1 shows how these parameters affect the viscosity curve with respect to shear rate. μ_0 and μ_∞ are the dimensionless viscosities at zero and infinite shear rate, respectively ($\mu_0 = \hat{\mu}_0/\eta_0, \quad \mu_\infty = \hat{\mu}_\infty/\eta_0$, where η_0 is the reference dynamic viscosity). λ_{CY} is the dimensionless time constant which determines the shear rate at which the transition from the zero-shear-rate plateau to the power-law region arises. It also governs the location of transition from the power-law region to the infinite-shear-rate plateau. a, the shape parameter, defines the shape of transition region between the zero-shear-rate plateau and the power-law region. n is the power-law index describing the slope of the power-law region of the viscosity curve with respect to shear rate [48–51, 66]. The dimensionless time constant λ_{CY} which is called the Carreau number and Reynolds number, Re, are defined as [61]:

$$ \lambda_{CY} = \frac{\lambda v_0}{L_0}, \quad \text{Re} = \frac{\rho_0 v_0 L_0}{\eta_0} \tag{2.8} $$

where λ is the time constant and the quantities with subscript zero are the reference quantities whose meanings are mentioned before.

2.2 Non-isothermal generalized Newtonian flows

Two types of non-isothermal flows are considered. The first type (Type A) includes the viscous dissipation term in the energy balance equation and the second one (Type B) includes the buoyancy force term in the linear momentum balance equation. The two types are described separately, because they are non-dimensionalized with different reference quantities.

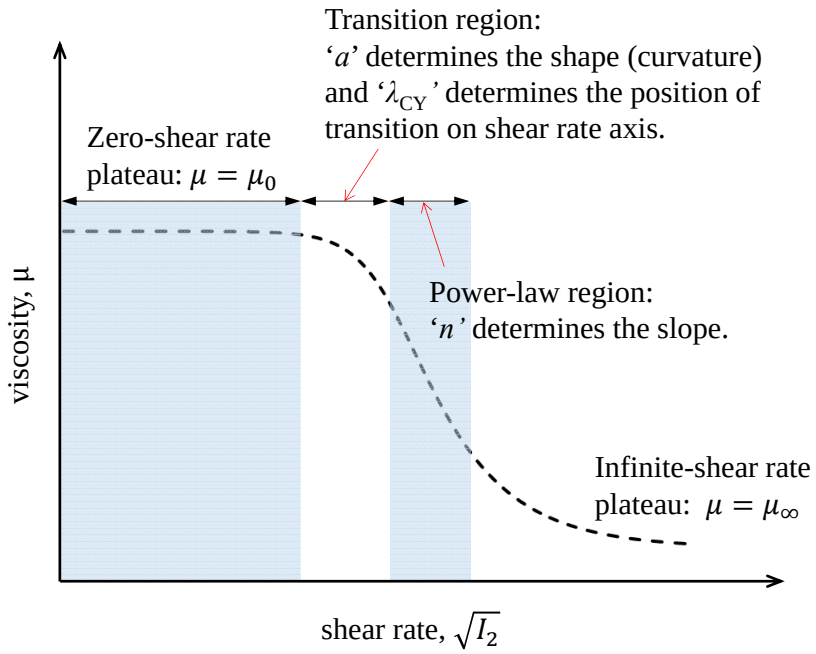

Figure 2.1: Typical viscosity curve for the Carreau–Yasuda model.

2.2.1 Type A: with viscous dissipation

For the first type, we consider a steady, incompressible, and non-isothermal flow of generalized Newtonian fluids, where viscous dissipation arises. The problem is governed by Eq. (2.10) which are obtained by non-dimensionalizing the equations for conservation of mass, momentum, and energy using the following dimensionless variables [13, 60, 62, 67–69]:

$$\mathbf{x} = \frac{\hat{\mathbf{x}}}{L_0}, \quad \mathbf{v} = \frac{\hat{\mathbf{v}}}{v_0}, \quad p = \frac{\hat{p}}{\rho_0 {v_0}^2}, \quad \theta = \frac{\hat{T} - T_0}{T_1 - T_0}, \tag{2.9}$$

where $\mathbf{x}$, $\mathbf{v}$, p and θ are the dimensionless coordinates, velocity vector, pressure and temperature, respectively, and the hat symbol denotes their physical counterparts. L_0, v_0, and ρ_0 are the reference length, velocity, and density, respectively. T_0 and T_1 are the reference wall temperature and bulk fluid temperature, respectively.

$$\boldsymbol{\nabla} \cdot \mathbf{v} = 0 \qquad \text{in } \Omega \qquad (2.10a)$$

$$\mathbf{v} \cdot \boldsymbol{\nabla}\mathbf{v} + \boldsymbol{\nabla} p - \boldsymbol{\nabla} \cdot \left[\mu(I_2)\left(\boldsymbol{\nabla}\mathbf{v} + \boldsymbol{\nabla}\mathbf{v}^{\mathrm{T}}\right)\right] = 0 \qquad \text{in } \Omega \qquad (2.10b)$$

$$\mathbf{v} \cdot \boldsymbol{\nabla}\theta - \frac{1}{\mathrm{Pe}}\Delta\theta - \frac{1}{2}\frac{\mathrm{Br}}{\mathrm{Pr}}\,\mu(I_2)\left(\boldsymbol{\nabla}\mathbf{v} + \boldsymbol{\nabla}\mathbf{v}^{\mathrm{T}}\right) : \left(\boldsymbol{\nabla}\mathbf{v} + \boldsymbol{\nabla}\mathbf{v}^{\mathrm{T}}\right) = 0 \qquad \text{in } \Omega \qquad (2.10c)$$

By introducing the viscous stress tensor $\underline{\boldsymbol{\tau}}$ and the heat flux vector $\mathbf{q}$ as auxiliary variables, the Navier–Stokes equations (Eq. (2.10b)) and the energy equation (Eq. (2.10c)) can be re-written into the equivalent first-order forms, Eq. (2.11b)–(2.11c) and Eq. (2.11d)–(2.11e), respectively. This makes it possible to use C^0 basis functions in the numerical implementation [4]:

$$\boldsymbol{\nabla} \cdot \mathbf{v} = 0 \qquad \text{in } \Omega \qquad (2.11a)$$

$$\mathbf{v} \cdot \boldsymbol{\nabla}\mathbf{v} + \boldsymbol{\nabla} p - \boldsymbol{\nabla} \cdot \underline{\boldsymbol{\tau}} = 0 \qquad \text{in } \Omega \qquad (2.11b)$$

$$\underline{\boldsymbol{\tau}} = \mu(I_2)\left(\boldsymbol{\nabla}\mathbf{v} + \boldsymbol{\nabla}\mathbf{v}^{\mathrm{T}}\right) \qquad \text{in } \Omega \qquad (2.11c)$$

$$\mathbf{v} \cdot \boldsymbol{\nabla}\theta + \boldsymbol{\nabla} \cdot \mathbf{q} - \frac{1}{2}\frac{\mathrm{Br}}{\mathrm{Pr}}\,\underline{\boldsymbol{\tau}} : \left(\boldsymbol{\nabla}\mathbf{v} + \boldsymbol{\nabla}\mathbf{v}^{\mathrm{T}}\right) = 0 \qquad \text{in } \Omega \qquad (2.11d)$$

$$\mathbf{q} = -\frac{1}{\mathrm{Pe}}\boldsymbol{\nabla}\theta \qquad \text{in } \Omega \qquad (2.11e)$$

$$\mathbf{v} = \mathbf{v}^{\mathrm{s}} \qquad \text{on } \Gamma_v \qquad (2.11f)$$

$$\hat{\mathbf{n}} \cdot \underline{\boldsymbol{\sigma}} = \mathbf{t}^{\mathrm{s}} \qquad \text{on } \Gamma_t \qquad (2.11g)$$

$$\theta = \theta^{\mathrm{s}} \qquad \text{on } \Gamma_\theta \qquad (2.11h)$$

$$\hat{\mathbf{n}} \cdot \mathbf{q} = q^{\mathrm{s}} \qquad \text{on } \Gamma_q \qquad (2.11i)$$

where $\boldsymbol{\nabla}$ is the vector differential operator, $\mathbf{v}$ is the velocity vector, p is the pressure, $\underline{\boldsymbol{\tau}}$ is the viscous stress tensor, θ is the temperature, $\mu(I_2)$ is the shear-rate dependent viscosity, $\mathbf{q}$ is the heat flux vector, $\underline{\boldsymbol{\sigma}}$ is the total stress tensor, and $\hat{\mathbf{n}}$ is the outward unit normal vector. The last term of

Eq. (2.11d) is called viscous dissipation, Φ,

$$\Phi = \underline{\boldsymbol{\tau}} : \underline{\mathbf{D}} = \underline{\boldsymbol{\tau}} : \frac{1}{2}\left(\boldsymbol{\nabla}\mathbf{v} + \boldsymbol{\nabla}\mathbf{v}^{\mathrm{T}}\right). \tag{2.12}$$

which is the amount of mechanical energy dissipated as heat due to the deformation caused by viscosity [60]. Equations (2.11f)–(2.11i) are the boundary conditions, where $\mathbf{v}^{\mathrm{s}}$, $\mathbf{t}^{\mathrm{s}}$, θ^{s} and q^{s} are the specified velocity on the boundary Γ_v, the specified traction on the boundary Γ_t, the specified temperature on the boundary Γ_θ and the specified heat flux on the boundary Γ_q, respectively. Γ is the total boundary enclosing the fluid domain Ω satisfying $\Gamma = \Gamma_v \cup \Gamma_t$, $\emptyset = \Gamma_v \cap \Gamma_t$, $\Gamma = \Gamma_\theta \cup \Gamma_q$ and $\emptyset = \Gamma_\theta \cap \Gamma_q$.

The dimensionless numbers appeared in Eq. (2.5) and (2.11) are defined as:

$$\text{Reynolds number:} \quad \mathrm{Re} = \frac{\rho_0 v_0 L_0}{\eta_0}, \quad \frac{\text{inertial force}}{\text{viscous force}} \tag{2.13a}$$

$$\text{Prandtle number:} \quad \mathrm{Pr} = \frac{\nu_0}{\alpha}, \quad \frac{\text{momentum diffusivity}}{\text{thermal diffusivity}} \tag{2.13b}$$

$$\text{Brinkman number:} \quad \mathrm{Br} = \frac{\eta_0 v_0^2}{k\left(T_1 - T_0\right)}, \quad \frac{\text{heat produced by viscous dissipation}}{\text{heat produced by molecular conduction}} \tag{2.13c}$$

$$\text{Peclet number:} \quad \mathrm{Pe} = \mathrm{Pr}\,\mathrm{Re} = \frac{v_0 L_0}{\alpha}, \quad \frac{\text{advection of heat}}{\text{diffusion of heat}}, \tag{2.13d}$$

where the meanings of ρ_0, v_0, L_0, T_0 and T_1 are described under the Eq. (2.9). η_0 and ν_0 $(= \eta_0/\rho_0)$ are the reference dynamic viscosity and kinematic viscosity, respectively. k is the thermal conductivity and α $(= k/\rho_0 c_p,$ where c_p is the specific heat capacity$)$ is the thermal diffusivity. As in the isothermal case, the constitutive equation for generalized Newtonian fluids is:

$$\underline{\boldsymbol{\sigma}} = -p\underline{\mathbf{I}} + \underline{\boldsymbol{\tau}} = -p\underline{\mathbf{I}} + \mu(I_2)\left(\boldsymbol{\nabla}\mathbf{v} + \boldsymbol{\nabla}\mathbf{v}^{\mathrm{T}}\right). \tag{2.14}$$

In this study, we assume that the viscosity does not depend on temperature, so the same Carreau–Yasuda model with the isothermal case given in Eq. (2.5) is considered.

2.2.2 Type B: with buoyancy force

The second type is for a steady, incompressible, and non-isothermal flow of generalized Newtonian fluids, where buoyancy force is included. The problem is governed by Eq. (2.16) which are obtained by non-dimensionalizing the equations for conservation of mass, momentum, and energy using the following dimensionless variables [13, 70]:

$$\mathbf{x} = \frac{\hat{\mathbf{x}}}{L_0}, \quad \mathbf{v} = \frac{\hat{\mathbf{v}}}{v_0}, \quad p = \frac{\hat{p}}{\rho_0 {v_0}^2}, \quad \theta = \frac{\hat{T} - T_0}{T_1 - T_0}, \tag{2.15}$$

where $\mathbf{x}$, $\mathbf{v}$, p and θ are the dimensionless coordinates, velocity vector, pressure and temperature, respectively, and the hat symbol denotes their physical counterparts. L_0, $v_0 = \sqrt{g\beta(T_1 - T_0)L_0}$, and ρ_0 are reference length, buoyant speed (as reference velocity), and reference density, respectively. T_0 and T_1 are reference temperatures.

$$\boldsymbol{\nabla} \cdot \mathbf{v} = 0 \qquad \text{in } \Omega \tag{2.16a}$$

$$\mathbf{v} \cdot \boldsymbol{\nabla}\mathbf{v} + \boldsymbol{\nabla} p - \boldsymbol{\nabla} \cdot \left[\mu(I_2)\left(\boldsymbol{\nabla}\mathbf{v} + \boldsymbol{\nabla}\mathbf{v}^{\mathrm{T}}\right)\right] + \frac{\mathbf{g}}{|\mathbf{g}|}\theta = 0 \qquad \text{in } \Omega \tag{2.16b}$$

$$\mathbf{v} \cdot \boldsymbol{\nabla}\theta - \frac{1}{\mathrm{Pe}}\Delta\theta = 0 \qquad \text{in } \Omega \tag{2.16c}$$

The Boussinesq approximation is used to include buoyancy force which is caused by temperature dependence of density and equal to $\rho_0 \mathbf{g}\beta(T_1 - T_0)$ in dimensional form. In this approximation, the density variation is neglected except for the term with gravitational acceleration, $\mathbf{g}$ [71]. By introducing the viscous stress tensor $\underline{\boldsymbol{\tau}}$ and the heat flux vector $\mathbf{q}$ as auxiliary variables, the Navier–Stokes equations (Eq. (2.16b)) and the energy equation (Eq. (2.16c)) can be recast into the equivalent first-order forms, Eq. (2.17b)–(2.17c) and Eq. (2.17d)–(2.17e), respectively. This makes it

possible to use C^0 basis functions in the numerical implementation [4]:

$$\boldsymbol{\nabla} \cdot \mathbf{v} = 0 \qquad \text{in } \Omega \tag{2.17a}$$

$$\mathbf{v} \cdot \boldsymbol{\nabla}\mathbf{v} + \boldsymbol{\nabla} p - \boldsymbol{\nabla} \cdot \underline{\boldsymbol{\tau}} + \frac{\mathbf{g}}{|\mathbf{g}|}\theta = 0 \qquad \text{in } \Omega \tag{2.17b}$$

$$\underline{\boldsymbol{\tau}} = \mu(I_2)\left(\boldsymbol{\nabla}\mathbf{v} + \boldsymbol{\nabla}\mathbf{v}^{\mathrm{T}}\right) \qquad \text{in } \Omega \tag{2.17c}$$

$$\mathbf{v} \cdot \boldsymbol{\nabla}\theta + \boldsymbol{\nabla} \cdot \mathbf{q} = 0 \qquad \text{in } \Omega \tag{2.17d}$$

$$\mathbf{q} = -\frac{1}{\mathrm{Pe}}\boldsymbol{\nabla}\theta \qquad \text{in } \Omega \tag{2.17e}$$

$$\mathbf{v} = \mathbf{v}^{\mathrm{s}} \qquad \text{on } \Gamma_v \tag{2.17f}$$

$$\hat{\mathbf{n}} \cdot \underline{\boldsymbol{\sigma}} = \mathbf{t}^{\mathrm{s}} \qquad \text{on } \Gamma_t \tag{2.17g}$$

$$\theta = \theta^{\mathrm{s}} \qquad \text{on } \Gamma_\theta \tag{2.17h}$$

$$\hat{\mathbf{n}} \cdot \mathbf{q} = q^{\mathrm{s}} \qquad \text{on } \Gamma_q \tag{2.17i}$$

where $\boldsymbol{\nabla}$ is vector differential operator, $\mathbf{v}$ is velocity vector, p is pressure, $\underline{\boldsymbol{\tau}}$ is viscous stress tensor, θ is temperature, $\mathbf{g}$ is gravitational acceleration vector, $\mu(I_2)$ is shear-rate dependent viscosity, $\mathbf{q}$ is heat flux vector, $\underline{\boldsymbol{\sigma}}$ is total stress tensor, and $\hat{\mathbf{n}}$ is outward unit normal vector. Equations (2.17f)–(2.17i) are the boundary conditions, where $\mathbf{v}^{\mathrm{s}}$, $\mathbf{t}^{\mathrm{s}}$, θ^{s} and q^{s} are the specified velocity on the boundary Γ_v, the specified traction on the boundary Γ_t, the specified temperature on the boundary Γ_θ and the specified heat flux on the boundary Γ_q, respectively. Γ is the total boundary enclosing the fluid domain Ω satisfying $\Gamma = \Gamma_v \cup \Gamma_t$, $\emptyset = \Gamma_v \cap \Gamma_t$, $\Gamma = \Gamma_\theta \cup \Gamma_q$ and $\emptyset = \Gamma_\theta \cap \Gamma_q$.

The dimensionless numbers used in Eq. (2.5) and (2.17) are defined as:

$$\text{Reynolds number:} \quad \mathrm{Re} = (\mathrm{Ra}/\mathrm{Pr})^{1/2} \tag{2.18a}$$

$$\text{Peclet number:} \quad \mathrm{Pe} = (\mathrm{Ra}\,\mathrm{Pr})^{1/2} \tag{2.18b}$$

$$\text{Prandtle number:} \quad \mathrm{Pr} = \frac{\nu_0}{\alpha}, \quad \frac{\text{momentum diffusivity}}{\text{thermal diffusivity}} \tag{2.18c}$$

$$\text{Grashof number:} \quad \mathrm{Gr} = \frac{\beta g L_0^3 (T_1 - T_0)}{\nu_0^2}, \quad \frac{\text{buoyancy force}}{\text{viscous force}} \tag{2.18d}$$

$$\text{Rayleigh number:} \quad \mathrm{Ra} = \mathrm{Gr}\,\mathrm{Pr} = \frac{\beta g L_0^3 (T_1 - T_0)}{\alpha\,\nu_0}, \tag{2.18e}$$

where the meanings of ρ_0, v_0, L_0, T_0 and T_1 are described under the Eq. (2.9). η_0 and $\nu_0\,(= \eta_0/\rho_0)$ are the reference dynamic viscosity and kinematic viscosity, respectively. k is the thermal conductivity and $\alpha\,(= k/\rho_0 c_p$, where c_p is the specific heat capacity$)$ is the thermal diffusivity. β is the volumetric thermal expansion coefficient and g is the gravitational acceleration. As in the isothermal case, the constitutive equation for generalized Newtonian fluids is:

$$\underline{\boldsymbol{\sigma}} = -p\underline{\mathbf{I}} + \underline{\boldsymbol{\tau}} = -p\underline{\mathbf{I}} + \mu(I_2)\left(\boldsymbol{\nabla}\mathbf{v} + \boldsymbol{\nabla}\mathbf{v}^{\mathrm{T}}\right). \tag{2.19}$$

We assume that the viscosity does not depend on temperature, so the same Carreau–Yasuda model with the isothermal case given in Eq. (2.5) is considered.

3. LEAST-SQUARES FORMULATION *

The least-squares formulations for the governing equations of isothermal flows (Eq. (2.3)) and of non-isothermal ones (Eq. (2.11) and (2.17)) are described in the separate sections. We use the standard notation for the Sobolev (or Hilbert) space of order $m \geq 0$, $H^m(\Omega)$, in the domain Ω. $\|\cdot\|_{\Omega,m}$ denotes the corresponding norm and $\mathbf{H}^m(\Omega) = [H^m(\Omega)]^n$ denotes the product spaces, where n is the number of dependent variables [4, 32].

3.1 Isothermal generalized Newtonian flows

The standard L_2-norm least-squares functional associated with the velocity–pressure–stress ($\mathbf{v} - p - \underline{\boldsymbol{\tau}}$) first-order system can be constructed by taking the sum of the squares of the L_2-norms of the residuals in the governing equations, Eq. (2.3a)–(2.3c):

$$\mathcal{J}(p, \mathbf{v}, \underline{\boldsymbol{\tau}}; \mathbf{f}) = \frac{1}{2}\left(\|R_1\|^2_{\Omega,0} + \|\mathbf{R_2}\|^2_{\Omega,0} + \|\underline{\mathbf{R_3}}\|^2_{\Omega,0}\right) \tag{3.1a}$$

$$R_1 = \boldsymbol{\nabla}\cdot\mathbf{v} \tag{3.1b}$$

$$\mathbf{R_2} = \mathbf{v}\cdot\boldsymbol{\nabla}\mathbf{v} + \boldsymbol{\nabla}p - \boldsymbol{\nabla}\cdot\underline{\boldsymbol{\tau}} - \mathbf{f} \tag{3.1c}$$

$$\underline{\mathbf{R_3}} = \underline{\boldsymbol{\tau}} - \mu(I_2)\left(\boldsymbol{\nabla}\mathbf{v} + \boldsymbol{\nabla}\mathbf{v}^{\mathrm{T}}\right). \tag{3.1d}$$

The residuals $\left(R_1, \mathbf{R_2}, \underline{\mathbf{R_3}}\right)$ are obtained after choosing and substituting the suitable finite element approximations for $(p, \mathbf{v}, \underline{\boldsymbol{\tau}})$ (described in Section 4.1). The minimization problem, $\delta\mathcal{J} = 0$, is to find $\mathbf{u} = (p, \mathbf{v}, \underline{\boldsymbol{\tau}}) \in \mathcal{V}$ such that for all $\delta\mathbf{u} = (\delta p, \delta\mathbf{v}, \delta\underline{\boldsymbol{\tau}}) \in \mathcal{V}$ the following equation holds:

$$\mathcal{B}(\mathbf{u}, \delta\mathbf{u}) = \mathcal{F}(\delta\mathbf{u}), \tag{3.2}$$

*Reprinted with permission from "A spectral/hp least-squares finite element analysis of the Carreau–Yasuda fluids," by Namhee Kim and J. N. Reddy, 2016. International Journal for Numerical Methods in Fluids, Vol. 82, pp. 541–566. Copyright 2016 by John Wiley & Sons, Ltd. and from "3-D least-squares finite element analysis of flows of generalized Newtonian fluids," by Namhee Kim and J. N. Reddy, 2019. *Journal of Non-Newtonian Fluid Mechanics*, Vol. 266, pp. 143–159. Copyright 2019 by Elsevier, B.V.

where $(\delta p, \delta\mathbf{v}, \delta\underline{\boldsymbol{\tau}})$ represent the corresponding weights for the set of variables $(p, \mathbf{v}, \underline{\boldsymbol{\tau}})$ and $\mathcal{V}$ is an appropriate function space. We employed the Newton's method as a linearization scheme before minimizing the least-squares functional, $\mathcal{J}$, and the resulting bilinear form ($\mathcal{B}(\cdot,\cdot)$) and linear form ($\mathcal{F}(\cdot,\cdot)$) are given as

$$\begin{aligned}
\mathcal{B}\left(\mathbf{u}, \delta\mathbf{u}\right) = \int_{\Omega} \Big[& \left(\boldsymbol{\nabla}\cdot\delta\mathbf{v}\right)\left(\boldsymbol{\nabla}\cdot\mathbf{v}\right) + \left(\delta\mathbf{v}\cdot\boldsymbol{\nabla}\mathbf{v}_0 + \mathbf{v}_0\cdot\boldsymbol{\nabla}\delta\mathbf{v} + \boldsymbol{\nabla}\delta p - \boldsymbol{\nabla}\cdot\delta\underline{\boldsymbol{\tau}}\right)\cdot \\
& \left(\mathbf{v}\cdot\boldsymbol{\nabla}\mathbf{v}_0 + \mathbf{v}_0\cdot\boldsymbol{\nabla}\mathbf{v} + \boldsymbol{\nabla}p - \boldsymbol{\nabla}\cdot\underline{\boldsymbol{\tau}}\right) \\
& + \left\{\delta\underline{\boldsymbol{\tau}} - {}^{\mathrm{v}_0}\boldsymbol{\nabla}\mu^0\cdot\delta\mathbf{v}\left(\boldsymbol{\nabla}\mathbf{v}_0 + \boldsymbol{\nabla}\mathbf{v}_0^{\mathrm{T}}\right) - \mu^0\left(\boldsymbol{\nabla}\delta\mathbf{v} + \boldsymbol{\nabla}\delta\mathbf{v}^{\mathrm{T}}\right)\right\} : \\
& \left\{\underline{\boldsymbol{\tau}} - {}^{\mathrm{v}_0}\boldsymbol{\nabla}\mu^0\cdot\mathbf{v}\left(\boldsymbol{\nabla}\mathbf{v}_0 + \boldsymbol{\nabla}\mathbf{v}_0^{\mathrm{T}}\right) - \mu^0\left(\boldsymbol{\nabla}\mathbf{v} + \boldsymbol{\nabla}\mathbf{v}^{\mathrm{T}}\right)\right\} \Big] d\Omega
\end{aligned} \tag{3.3}$$

$$\begin{aligned}
\mathcal{F}\left(\delta\mathbf{u}\right) = \int_{\Omega} \Big[& \left(\delta\mathbf{v}\cdot\boldsymbol{\nabla}\mathbf{v}_0 + \mathbf{v}_0\cdot\boldsymbol{\nabla}\delta\mathbf{v} + \boldsymbol{\nabla}\delta p - \boldsymbol{\nabla}\cdot\delta\underline{\boldsymbol{\tau}}\right)\cdot\left(\mathbf{v}_0\cdot\boldsymbol{\nabla}\mathbf{v}_0 + \mathbf{f}\right) \\
& - \left\{\delta\underline{\boldsymbol{\tau}} - {}^{\mathrm{v}_0}\boldsymbol{\nabla}\mu^0\cdot\delta\mathbf{v}\left(\boldsymbol{\nabla}\mathbf{v}_0 + \boldsymbol{\nabla}\mathbf{v}_0^{\mathrm{T}}\right) - \mu^0\left(\boldsymbol{\nabla}\delta\mathbf{v} + \boldsymbol{\nabla}\delta\mathbf{v}^{\mathrm{T}}\right)\right\} : \\
& {}^{\mathrm{v}_0}\boldsymbol{\nabla}\mu^0\cdot\mathbf{v}_0\left(\boldsymbol{\nabla}\mathbf{v}_0 + \boldsymbol{\nabla}\mathbf{v}_0^{\mathrm{T}}\right) \Big] d\Omega.
\end{aligned} \tag{3.4}$$

$\mathbf{v}_0$, p_0, and μ^0 are characteristic states where the solutions are linearized and they are known quantities from the previous iteration in the numerical implementation. In Eq. (3.3)–(3.4), ${}^{\mathrm{v}_0}\boldsymbol{\nabla}$ is the gradient operator acting with respect to $\mathbf{v}_0$.

3.2 Non-isothermal generalized Newtonian flows

3.2.1 Type A: with viscous dissipation

For non-isothermal flows with viscous dissipation, the standard L_2-norm least-squares functional associated with the velocity–pressure–stress–temperature–heat flux ($\mathbf{v} - p - \underline{\boldsymbol{\tau}} - \theta - \mathbf{q}$) first-order system can be constructed by taking the sum of the squares of the L_2-norms of the

residuals in the governing equations, Eq. (2.11a)–(2.11e):

$$\mathcal{J}\left(p, \mathbf{v}, \underline{\boldsymbol{\tau}}, \theta, \mathbf{q}\right) = \frac{1}{2}\left(\|R_1\|^2_{\Omega,0} + \|\mathbf{R_2}\|^2_{\Omega,0} + \|\underline{\mathbf{R_3}}\|^2_{\Omega,0} + \|R_4\|^2_{\Omega,0} + \|\mathbf{R_5}\|^2_{\Omega,0}\right) \tag{3.5a}$$

$$R_1 = \boldsymbol{\nabla} \cdot \mathbf{v} \tag{3.5b}$$

$$\mathbf{R_2} = \mathbf{v} \cdot \boldsymbol{\nabla}\mathbf{v} + \boldsymbol{\nabla} p - \boldsymbol{\nabla} \cdot \underline{\boldsymbol{\tau}} \tag{3.5c}$$

$$\underline{\mathbf{R_3}} = \underline{\boldsymbol{\tau}} - \mu(I_2)\left(\boldsymbol{\nabla}\mathbf{v} + \boldsymbol{\nabla}\mathbf{v}^{\mathrm{T}}\right) \tag{3.5d}$$

$$R_4 = \mathbf{v} \cdot \boldsymbol{\nabla}\theta + \boldsymbol{\nabla} \cdot \mathbf{q} - \frac{1}{2}\frac{\mathrm{Br}}{\mathrm{Pr}}\underline{\boldsymbol{\tau}} : \left(\boldsymbol{\nabla}\mathbf{v} + \boldsymbol{\nabla}\mathbf{v}^{\mathrm{T}}\right) \tag{3.5e}$$

$$\mathbf{R_5} = \mathbf{q} + \frac{1}{\mathrm{Pe}}\boldsymbol{\nabla}\theta. \tag{3.5f}$$

The residuals $\left(R_1, \mathbf{R_2}, \underline{\mathbf{R_3}}, R_4, \mathbf{R_5}\right)$ are obtained after choosing and substituting the suitable finite element approximations for $(p, \mathbf{v}, \underline{\boldsymbol{\tau}}, \theta, \mathbf{q})$ (described in Section 4.2). The minimization problem, $\delta\mathcal{J} = 0$, is to find $\mathbf{u} = (p, \mathbf{v}, \underline{\boldsymbol{\tau}}, \theta, \mathbf{q}) \in \mathcal{V}$ such that for all $\delta\mathbf{u} = (\delta p, \delta\mathbf{v}, \delta\underline{\boldsymbol{\tau}}, \delta\theta, \delta\mathbf{q}) \in \mathcal{V}$ the following equation holds:

$$\mathcal{B}\left(\mathbf{u}, \delta\mathbf{u}\right) = \mathcal{F}\left(\delta\mathbf{u}\right), \tag{3.6}$$

where $(\delta p, \delta\mathbf{v}, \delta\underline{\boldsymbol{\tau}}, \delta\theta, \delta\mathbf{q})$ represent the corresponding weights for the set of variables $(p, \mathbf{v}, \underline{\boldsymbol{\tau}}, \theta, \mathbf{q})$ and $\mathcal{V}$ is an appropriate function space. We employed the Newton's method as a linearization scheme before minimizing the least-squares functional, $\mathcal{J}$, and the resulting bilinear form ($\mathcal{B}(\cdot,\cdot)$) and linear form ($\mathcal{F}(\cdot,\cdot)$) are given as

$$
\begin{aligned}
&\mathcal{B}\left(\mathbf{u}, \delta\mathbf{u}\right) \\
&= \int_{\Omega} \Bigg[\left(\boldsymbol{\nabla} \cdot \delta\mathbf{v}\right)\left(\boldsymbol{\nabla} \cdot \mathbf{v}\right) + \left(\delta\mathbf{v} \cdot \boldsymbol{\nabla}\mathbf{v}_0 + \mathbf{v}_0 \cdot \boldsymbol{\nabla}\delta\mathbf{v} + \boldsymbol{\nabla}\delta p - \boldsymbol{\nabla} \cdot \delta\underline{\boldsymbol{\tau}}\right) \cdot \\
&\qquad \left(\mathbf{v} \cdot \boldsymbol{\nabla}\mathbf{v}_0 + \mathbf{v}_0 \cdot \boldsymbol{\nabla}\mathbf{v} + \boldsymbol{\nabla}p - \boldsymbol{\nabla} \cdot \underline{\boldsymbol{\tau}}\right) \\
&\qquad + \left\{ \delta\underline{\boldsymbol{\tau}} - \left({}^{\mathrm{v}_0}\boldsymbol{\nabla}\mu^0 \cdot \delta\mathbf{v} + \frac{\partial \mu^0}{\partial \theta_0}\delta\theta \right)\left(\boldsymbol{\nabla}\mathbf{v}_0 + \boldsymbol{\nabla}\mathbf{v}_0^{\mathrm{T}}\right) - \mu^0\left(\boldsymbol{\nabla}\delta\mathbf{v} + \boldsymbol{\nabla}\delta\mathbf{v}^{\mathrm{T}}\right) \right\} : \\
&\qquad \left\{ \underline{\boldsymbol{\tau}} - \left({}^{\mathrm{v}_0}\boldsymbol{\nabla}\mu^0 \cdot \mathbf{v} + \frac{\partial \mu^0}{\partial \theta_0}\theta \right)\left(\boldsymbol{\nabla}\mathbf{v}_0 + \boldsymbol{\nabla}\mathbf{v}_0^{\mathrm{T}}\right) - \mu^0\left(\boldsymbol{\nabla}\mathbf{v} + \boldsymbol{\nabla}\mathbf{v}^{\mathrm{T}}\right) \right\} \\
&\qquad + \left\{ \delta\mathbf{v} \cdot \boldsymbol{\nabla}\theta_0 + \mathbf{v}_0 \cdot \boldsymbol{\nabla}\delta\theta + \boldsymbol{\nabla} \cdot \delta\mathbf{q} - \frac{1}{2}\frac{\mathrm{Br}}{\mathrm{Pr}} \left[\delta\underline{\boldsymbol{\tau}} : \left(\boldsymbol{\nabla}\mathbf{v}_0 + \boldsymbol{\nabla}\mathbf{v}_0^{\mathrm{T}}\right) \right. \right. \\
&\qquad \left. \left. + \underline{\boldsymbol{\tau}}_0 : \left(\boldsymbol{\nabla}\delta\mathbf{v} + \boldsymbol{\nabla}\delta\mathbf{v}^{\mathrm{T}}\right) \right] \right\} \left\{ \mathbf{v} \cdot \boldsymbol{\nabla}\theta_0 + \mathbf{v}_0 \cdot \boldsymbol{\nabla}\theta + \boldsymbol{\nabla} \cdot \mathbf{q} \right. \\
&\qquad \left. - \frac{1}{2}\frac{\mathrm{Br}}{\mathrm{Pr}} \left[\underline{\boldsymbol{\tau}} : \left(\boldsymbol{\nabla}\mathbf{v}_0 + \boldsymbol{\nabla}\mathbf{v}_0^{\mathrm{T}}\right) + \underline{\boldsymbol{\tau}}_0 : \left(\boldsymbol{\nabla}\mathbf{v} + \boldsymbol{\nabla}\mathbf{v}^{\mathrm{T}}\right) \right] \right\} \\
&\qquad + \left(\delta\mathbf{q} + \frac{1}{\mathrm{Pe}}\boldsymbol{\nabla}\delta\theta \right) \cdot \left(\mathbf{q} + \frac{1}{\mathrm{Pe}}\boldsymbol{\nabla}\theta \right) \Bigg] d\Omega
\end{aligned} \tag{3.7}
$$

$$
\begin{aligned}
&\mathcal{F}\left(\delta\mathbf{u}\right) \\
&= \int_{\Omega} \Bigg[\left(\delta\mathbf{v} \cdot \boldsymbol{\nabla}\mathbf{v}_0 + \mathbf{v}_0 \cdot \boldsymbol{\nabla}\delta\mathbf{v} + \boldsymbol{\nabla}\delta p - \boldsymbol{\nabla} \cdot \delta\underline{\boldsymbol{\tau}}\right) \cdot \left(\mathbf{v}_0 \cdot \boldsymbol{\nabla}\mathbf{v}_0\right) \\
&\qquad - \left\{ \delta\underline{\boldsymbol{\tau}} - \left({}^{\mathrm{v}_0}\boldsymbol{\nabla}\mu^0 \cdot \delta\mathbf{v} + \frac{\partial \mu^0}{\partial \theta_0}\delta\theta \right)\left(\boldsymbol{\nabla}\mathbf{v}_0 + \boldsymbol{\nabla}\mathbf{v}_0^{\mathrm{T}}\right) - \mu^0\left(\boldsymbol{\nabla}\delta\mathbf{v} + \boldsymbol{\nabla}\delta\mathbf{v}^{\mathrm{T}}\right) \right\} : \\
&\qquad \left({}^{\mathrm{v}_0}\boldsymbol{\nabla}\mu^0 \cdot \mathbf{v}_0 + \frac{\partial \mu^0}{\partial \theta_0}\theta_0 \right)\left(\boldsymbol{\nabla}\mathbf{v}_0 + \boldsymbol{\nabla}\mathbf{v}_0^{\mathrm{T}}\right) \\
&\qquad + \left\{ \delta\mathbf{v} \cdot \boldsymbol{\nabla}\theta_0 + \mathbf{v}_0 \cdot \boldsymbol{\nabla}\delta\theta + \boldsymbol{\nabla} \cdot \delta\mathbf{q} - \frac{1}{2}\frac{\mathrm{Br}}{\mathrm{Pr}} \left[\delta\underline{\boldsymbol{\tau}} : \left(\boldsymbol{\nabla}\mathbf{v}_0 + \boldsymbol{\nabla}\mathbf{v}_0^{\mathrm{T}}\right) \right. \right. \\
&\qquad \left. \left. + \underline{\boldsymbol{\tau}}_0 : \left(\boldsymbol{\nabla}\delta\mathbf{v} + \boldsymbol{\nabla}\delta\mathbf{v}^{\mathrm{T}}\right) \right] \right\} \left\{ \mathbf{v}_0 \cdot \boldsymbol{\nabla}\theta_0 - \frac{1}{2}\frac{\mathrm{Br}}{\mathrm{Pr}}\, \delta\underline{\boldsymbol{\tau}}_0 : \left(\boldsymbol{\nabla}\mathbf{v}_0 + \boldsymbol{\nabla}\mathbf{v}_0^{\mathrm{T}}\right) \right\} \Bigg] d\Omega
\end{aligned} \tag{3.8}
$$

where $\mathbf{v}_0$, p_0, $\underline{\boldsymbol{\tau}}_0$, θ_0, $\mathbf{q}_0$ and μ^0 are characteristic states where the solutions are linearized and they are known quantities from the previous iteration in the numerical implementation. In Eq. (3.7)–(3.8), ${}^{\mathrm{v}_0}\boldsymbol{\nabla}$ denotes the gradient operator acting with respect to $\mathbf{v}_0$.

3.2.2 Type B: with buoyancy force

For non-isothermal flows with buoyancy force, the standard L_2-norm least-squares functional associated with the velocity–pressure–stress–temperature–heat flux ($\mathbf{v} - p - \underline{\boldsymbol{\tau}} - \theta - \mathbf{q}$) first-order system can be constructed by taking the sum of the squares of the L_2-norms of the residuals in the governing equations, Eq. (2.17a)–(2.17e):

$$\mathcal{J}\left(p, \mathbf{v}, \underline{\boldsymbol{\tau}}, \theta, \mathbf{q}\right) = \frac{1}{2}\left(\|R_1\|^2_{\Omega,0} + \|\mathbf{R_2}\|^2_{\Omega,0} + \|\underline{\mathbf{R_3}}\|^2_{\Omega,0} + \|R_4\|^2_{\Omega,0} + \|\mathbf{R_5}\|^2_{\Omega,0}\right) \tag{3.9a}$$

$$R_1 = \boldsymbol{\nabla} \cdot \mathbf{v} \tag{3.9b}$$

$$\mathbf{R_2} = \mathbf{v} \cdot \boldsymbol{\nabla}\mathbf{v} + \boldsymbol{\nabla} p - \boldsymbol{\nabla} \cdot \underline{\boldsymbol{\tau}} + \frac{\mathbf{g}}{|\mathbf{g}|}\theta \tag{3.9c}$$

$$\underline{\mathbf{R_3}} = \underline{\boldsymbol{\tau}} - \mu(I_2)\left(\boldsymbol{\nabla}\mathbf{v} + \boldsymbol{\nabla}\mathbf{v}^{\mathrm{T}}\right) \tag{3.9d}$$

$$R_4 = \mathbf{v} \cdot \boldsymbol{\nabla}\theta + \boldsymbol{\nabla} \cdot \mathbf{q} \tag{3.9e}$$

$$\mathbf{R_5} = \mathbf{q} + \frac{1}{\mathrm{Pe}}\boldsymbol{\nabla}\theta. \tag{3.9f}$$

The residuals $\left(R_1, \mathbf{R_2}, \underline{\mathbf{R_3}}, R_4, \mathbf{R_5}\right)$ are obtained after choosing and substituting the suitable finite element approximations for $(p, \mathbf{v}, \underline{\boldsymbol{\tau}}, \theta, \mathbf{q})$ (described in Section 4.2). The minimization problem, $\delta\mathcal{J} = 0$, is to find $\mathbf{u} = (p, \mathbf{v}, \underline{\boldsymbol{\tau}}, \theta, \mathbf{q}) \in \mathcal{V}$ such that for all $\delta\mathbf{u} = (\delta p, \delta\mathbf{v}, \delta\underline{\boldsymbol{\tau}}, \delta\theta, \delta\mathbf{q}) \in \mathcal{V}$ the following equation holds:

$$\mathcal{B}\left(\mathbf{u}, \delta\mathbf{u}\right) = \mathcal{F}\left(\delta\mathbf{u}\right), \tag{3.10}$$

where $(\delta p, \delta\mathbf{v}, \delta\underline{\boldsymbol{\tau}}, \delta\theta, \delta\mathbf{q})$ represent the corresponding weights for the set of variables $(p, \mathbf{v}, \underline{\boldsymbol{\tau}}, \theta, \mathbf{q})$ and $\mathcal{V}$ is an appropriate function space. We employed the Newton's method as a linearization scheme before minimizing the least-squares functional, $\mathcal{J}$, and the resulting bilinear form ($\mathcal{B}(\cdot,\cdot)$) and linear form ($\mathcal{F}(\cdot,\cdot)$) are given as

$$
\begin{aligned}
&\mathcal{B}\left(\mathbf{u}, \delta\mathbf{u}\right) \\
&= \int_{\Omega} \Bigg[\left(\boldsymbol{\nabla} \cdot \delta\mathbf{v}\right)\left(\boldsymbol{\nabla} \cdot \mathbf{v}\right) + \left(\delta\mathbf{v} \cdot \boldsymbol{\nabla}\mathbf{v}_0 + \mathbf{v}_0 \cdot \boldsymbol{\nabla}\delta\mathbf{v} + \boldsymbol{\nabla}\delta p - \boldsymbol{\nabla} \cdot \delta\underline{\boldsymbol{\tau}} + \frac{\mathbf{g}}{|\mathbf{g}|}\delta\theta \right) \cdot \\
&\qquad \left(\mathbf{v} \cdot \boldsymbol{\nabla}\mathbf{v}_0 + \mathbf{v}_0 \cdot \boldsymbol{\nabla}\mathbf{v} + \boldsymbol{\nabla} p - \boldsymbol{\nabla} \cdot \underline{\boldsymbol{\tau}} + \frac{\mathbf{g}}{|\mathbf{g}|}\theta \right) \\
&\qquad + \left\{ \delta\underline{\boldsymbol{\tau}} - \left({}^{\mathrm{v}_0}\boldsymbol{\nabla}\mu^0 \cdot \delta\mathbf{v} + \frac{\partial \mu^0}{\partial \theta_0}\delta\theta \right) \left(\boldsymbol{\nabla}\mathbf{v}_0 + \boldsymbol{\nabla}\mathbf{v}_0^{\mathrm{T}} \right) - \mu^0 \left(\boldsymbol{\nabla}\delta\mathbf{v} + \boldsymbol{\nabla}\delta\mathbf{v}^{\mathrm{T}} \right) \right\} : \\
&\qquad \left\{ \underline{\boldsymbol{\tau}} - \left({}^{\mathrm{v}_0}\boldsymbol{\nabla}\mu^0 \cdot \mathbf{v} + \frac{\partial \mu^0}{\partial \theta_0}\theta \right) \left(\boldsymbol{\nabla}\mathbf{v}_0 + \boldsymbol{\nabla}\mathbf{v}_0^{\mathrm{T}} \right) - \mu^0 \left(\boldsymbol{\nabla}\mathbf{v} + \boldsymbol{\nabla}\mathbf{v}^{\mathrm{T}} \right) \right\} \\
&\qquad + \left\{ \delta\mathbf{v} \cdot \boldsymbol{\nabla}\theta_0 + \mathbf{v}_0 \cdot \boldsymbol{\nabla}\delta\theta + \boldsymbol{\nabla} \cdot \delta\mathbf{q} \right\} \left\{ \mathbf{v} \cdot \boldsymbol{\nabla}\theta_0 + \mathbf{v}_0 \cdot \boldsymbol{\nabla}\theta + \boldsymbol{\nabla} \cdot \mathbf{q} \right\} \\
&\qquad + \left(\delta\mathbf{q} + \frac{1}{\mathrm{Pe}}\boldsymbol{\nabla}\delta\theta \right) \cdot \left(\mathbf{q} + \frac{1}{\mathrm{Pe}}\boldsymbol{\nabla}\theta \right) \Bigg] d\Omega
\end{aligned} \tag{3.11}
$$

$$
\begin{aligned}
&\mathcal{F}\left(\delta\mathbf{u}\right) \\
&= \int_{\Omega} \Bigg[\left(\delta\mathbf{v} \cdot \boldsymbol{\nabla}\mathbf{v}_0 + \mathbf{v}_0 \cdot \boldsymbol{\nabla}\delta\mathbf{v} + \boldsymbol{\nabla}\delta p - \boldsymbol{\nabla} \cdot \delta\underline{\boldsymbol{\tau}} \right) \cdot \left(\mathbf{v}_0 \cdot \boldsymbol{\nabla}\mathbf{v}_0 \right) \\
&\qquad - \left\{ \delta\underline{\boldsymbol{\tau}} - \left({}^{\mathrm{v}_0}\boldsymbol{\nabla}\mu^0 \cdot \delta\mathbf{v} + \frac{\partial \mu^0}{\partial \theta_0}\delta\theta \right) \left(\boldsymbol{\nabla}\mathbf{v}_0 + \boldsymbol{\nabla}\mathbf{v}_0^{\mathrm{T}} \right) - \mu^0 \left(\boldsymbol{\nabla}\delta\mathbf{v} + \boldsymbol{\nabla}\delta\mathbf{v}^{\mathrm{T}} \right) \right\} : \\
&\qquad \left({}^{\mathrm{v}_0}\boldsymbol{\nabla}\mu^0 \cdot \mathbf{v}_0 + \frac{\partial \mu^0}{\partial \theta_0}\theta_0 \right) \left(\boldsymbol{\nabla}\mathbf{v}_0 + \boldsymbol{\nabla}\mathbf{v}_0^{\mathrm{T}} \right) \\
&\qquad + \left\{ \delta\mathbf{v} \cdot \boldsymbol{\nabla}\theta_0 + \mathbf{v}_0 \cdot \boldsymbol{\nabla}\delta\theta + \boldsymbol{\nabla} \cdot \delta\mathbf{q} \right\} \left(\mathbf{v}_0 \cdot \boldsymbol{\nabla}\theta_0 \right) \Bigg] d\Omega
\end{aligned} \tag{3.12}
$$

where $\mathbf{v}_0$, p_0, $\underline{\boldsymbol{\tau}}_0$, θ_0, $\mathbf{q}_0$ and μ^0 are characteristic states where the solutions are linearized and they are known quantities from the previous iteration in the numerical implementation. In Eq. (3.11)–(3.12), ${}^{\mathrm{v}_0}\boldsymbol{\nabla}$ denotes the gradient operator acting with respect to $\mathbf{v}_0$.

4. FINITE ELEMENT MODEL *

4.1 Isothermal generalized Newtonian flows

To develop the least-squares finite element model for isothermal generalized Newtonian flows described in Section 2.1, we define the least-squares functional of Eq. (3.1) over a typical element Ω^e in place of the total domain Ω. Ω is supposed to be divided into a set of non-overlapping subdomains (that is, finite elements), Ω^e. The isoparametric bijective mapping from the master element $\hat{\Omega}^e$ to the physical element Ω^e is used. Since the three-dimensional model includes all the variables of the two-dimensional model, we describe the three-dimensional model here. For a three-dimensional, steady, isothermal flow, we have ten field variables $(p, v_x, v_y, v_z, \tau_{xx}, \tau_{xy}, \tau_{xz}, \tau_{yy}, \tau_{yz}, \tau_{zz})$ and each variable is approximated by the expansion of the form:

$$u\left(x,y,z\right)=\sum_{i=1}^{n}u_i\psi_i\left(x,y,z\right) \tag{4.1}$$

where u represents any typical field variable from the list of ten variables and u_i are the nodal values of corresponding field variable; ψ_i denotes nodal interpolation functions. Since the minimum polynomial degree requirement on the approximation functions for the variables in Eq. (3.3)–(3.4) is linear, C^0 nodal basis functions can be used. Also, we can use the same basis functions of sufficiently higher order for all field variables of the formulation, as a high-order LSFEM is free of compatibility restrictions (that is, inf-sup or LBB condition) placed between the approximation spaces used. The C^0 spectral nodal interpolation functions, which were originally developed by

*Reprinted with permission from "A spectral/hp least-squares finite element analysis of the Carreau–Yasuda fluids," by Namhee Kim and J. N. Reddy, 2016. International Journal for Numerical Methods in Fluids, Vol. 82, pp. 541–566. Copyright 2016 by John Wiley & Sons, Ltd. and from "3-D least-squares finite element analysis of flows of generalized Newtonian fluids," by Namhee Kim and J. N. Reddy, 2019. *Journal of Non-Newtonian Fluid Mechanics*, Vol. 266, pp. 143–159. Copyright 2019 by Elsevier, B.V.

Patera [45], are used for ψ_i. One-dimensional C^0 spectral nodal basis is given by [46, 47]:

$$\hat{\psi}_i(\xi) = \begin{cases} 1, & \text{if } \xi = \xi_i \\ \frac{(\xi-1)(\xi+1)L'_{\mathrm{p}}(\xi)}{\mathrm{p}(\mathrm{p}+1)L_{\mathrm{p}}(\xi_i)(\xi-\xi_i)}, & \text{otherwise,} \end{cases} \tag{4.2}$$

where $-1 \leq \xi \leq 1$ and $L_{\mathrm{p}}(\xi)$ is the Legendre polynomials of order, p:

$$L_{\mathrm{p}}(\xi) = \frac{(-1)^{\mathrm{p}}}{2^{\mathrm{p}}\mathrm{p}!}\frac{d^{\mathrm{p}}}{dx^{\mathrm{p}}}\left[(1-\xi)^{\mathrm{p}}(1+\xi)^{\mathrm{p}}\right]. \tag{4.3}$$

The one-dimensional spectral interpolations functions in Eq. (4.2) of pth degree (i.e., there are $p+1$ nodes in the 1-D element) can regarded as the standard Lagrange interpolation functions with unevenly-spaced nodes, ξ_i, given by the roots of the following equation:

$$(\xi - 1)(\xi + 1) L'_{\mathrm{p}}(\xi) = 0. \tag{4.4}$$

These points are known as the Gauss–Lobatto–Legendre (GLL) points. By taking tensor product of the one-dimensional spectral bases of Eq. (4.2), we obtain three-dimensional spectral bases as Eq. (4.5) which is used for ψ_i in Eq. (4.1).

$$\psi_i(\xi,\eta,\zeta) = \hat{\psi}_j(\xi)\hat{\psi}_k(\eta)\hat{\psi}_l(\zeta), \quad -1 \leq (\xi,\eta,\zeta) \leq 1, \tag{4.5}$$

where $i = j + [k - 1 + (l-1)(\mathrm{p}+1)](\mathrm{p}+1)$ and $j,k,l = 1,...,\mathrm{p}+1$. The finite element equations are generated by substituting the finite element approximation (Eq. (4.1)) into the minimization problem (Eq. (3.3)–(3.4)) defined over an element Ω^e in place of the total domain Ω and

can be expressed in the matrix form as:

$$\begin{bmatrix} [K^{11}] & [K^{12}] & \dots & [K^{1,10}] \\ [K^{21}] & [K^{22}] & \dots & [K^{2,10}] \\ \vdots & \vdots & \ddots & \vdots \\ [K^{10,1}] & [K^{10,2}] & \dots & [K^{10,10}] \end{bmatrix} \begin{Bmatrix} \{p\} \\ \{v_x\} \\ \vdots \\ \{\tau_{zz}\} \end{Bmatrix} = \begin{Bmatrix} \{F^1\} \\ \{F^2\} \\ \vdots \\ \{F^{10}\} \end{Bmatrix} \tag{4.6}$$

Equation (4.6) is often termed as a *mixed* model because velocities are mixed with stresses in developing the finite element model [4]. The Gauss-Legendre quadrature rules are applied in the numerical integrations of the element coefficient matrices and force vectors in Eq. (4.6), and we used full integration to evaluate the integrals. At each Newton step, we build the element coefficient matrices and force vectors and perform element-level static node condensation to implicitly eliminate interior degrees of freedom. Then the global system of equations which is constructed from the assembly of the condensed finite element equations is solved utilizing the direct solver library called UMFPACK that has a set of subroutines to solve sparse linear systems directly using the unsymmetric-pattern multi-frontal method [5, 33, 72–75].

4.2 Non-isothermal generalized Newtonian flows

The steps for developing the least-squares finite element model for non-isothermal generalized Newtonian flows are the same with those for isothermal flows which are described in Section 4.1. We first define the least-squares functional, Eq. (3.5) or Eq. (3.9), over a typical element Ω^e in place of the total domain Ω. Ω is supposed to be divided into a set of non-overlapping sub-domains, that is, finite elements Ω^e. The isoparametric bijective mapping from the master element $\hat{\Omega}^e$ to the physical element Ω^e is used. For a three-dimensional, steady, non-isothermal flow, we have fourteen field variables $(p, v_x, v_y, v_z, \tau_{xx}, \tau_{xy}, \tau_{xz}, \tau_{yy}, \tau_{yz}, \tau_{zz}, \theta, q_x, q_y, q_z)$ and each field variable is approximated by the expansion of the form:

$$u\left(x, y, z\right) = \sum_{i=1}^{n} u_i \psi_i \left(x, y, z\right) \tag{4.7}$$

where u and u_i denote each field variable and the nodal values of corresponding field variable, respectively. Since the minimum regularity requirement on the approximation functions for the variables in Eq. (3.7)–(3.8) or in Eq. (3.11)–(3.12) is C^0-continuity, C^0 nodal basis can be applied. Also, we can use the same basis functions of sufficiently higher order for all field variables of the formulation, as a high-order LSFEM are free of compatibility restrictions (that is, inf-sup or LBB condition) placed between the approximation spaces used. ψ_i are the three-dimensional C^0 spectral nodal interpolation functions defined in Eq. (4.5).

The finite element equations are generated by substituting the finite element approximation (Eq. (4.7)) into the minimization problem (Eq. (3.7)–(3.8) or Eq. (3.11)–(3.12)) defined over an element Ω^e in place of the total domain Ω and can be expressed in the matrix form as:

$$\begin{bmatrix} [K^{11}] & [K^{12}] & \dots & [K^{1,14}] \\ [K^{21}] & [K^{22}] & \dots & [K^{2,14}] \\ \vdots & \vdots & \ddots & \vdots \\ [K^{14,1}] & [K^{14,2}] & \dots & [K^{14,14}] \end{bmatrix} \begin{Bmatrix} \{p\} \\ \{v_x\} \\ \vdots \\ \{q_z\} \end{Bmatrix} = \begin{Bmatrix} \{F^1\} \\ \{F^2\} \\ \vdots \\ \{F^{14}\} \end{Bmatrix} \tag{4.8}$$

Equation (4.8) is often termed as a *mixed* model, since velocities are mixed with stresses and temperature is mixed with heat-fluxes in developing the finite element model [4]. The Gauss-Legendre quadrature rules are applied in the numerical integrations of the element coefficient matrices and force vectors in Eq. (4.8), and we used full integration to evaluate the integrals. At each Newton step, we build the element coefficient matrices and force vectors and perform element-level static node condensation to implicitly eliminate interior degrees of freedom. Then the global system of equations which is constructed from the assembly of the condensed finite element equations is solved utilizing the direct solver library called UMFPACK that has a set of subroutines to solve sparse linear systems directly using the unsymmetric-pattern multi-frontal method [5, 33, 72–75].

5. NUMERICAL EXAMPLES *

Here, we present the numerical results for six separate two-dimensional steady flow problems, (Kovasznay flow, Jeffery-Hamel flow in a diverging channel, flow over a backward-facing step, flow in a lid-driven square cavity, flow past an unconfined circular cylinder, and fully-developed flow between parallel plates) and four separate three-dimensional steady flow problems (method of manufactured solutions, flow in a lid-driven cubic cavity, flow over a backward-facing step, and buoyancy-driven flow in a cubic cavity) using the developed least-squares finite element model. Using the analytical solution of Kovasznay flow problem (2-D) for isothermal Newtonian fluids, the exponential convergence of the developed LSFEM was verified and the convergence was compared with the other LSFEM which employs conventional Lagrange interpolation functions. Jeffery-Hamel flow (2-D) in a diverging channel which also possesses analytical solutions for Newtonian fluids is solved and the exponential convergence of the developed LSFEM was demonstrated. Also, the method of manufactured solutions for a 3-D flow was used to demonstrated exponential decay of the solution errors and least-squares functionals as the polynomial order increases. The other seven benchmark problems (i.e., 2-D and 3-D flow over a backward-facing step, 2-D flow in a lid-driven square cavity, 3-D flow in a lid-driven cubic cavity, 2-D flow past an unconfined circular cylinder, 2-D fully-developed flow between parallel plates, and 3-D buoyancy-driven flow in a cubic cavity) are used to verify and validate the present finite element models for isothermal and non-isothermal flows by comparing with the existing numerical, analytical and experimental studies available in the literature. In addition, a parametric study of the Carreau–Yasuda constitutive model for these problems is performed to examine the effect of change in parameters on the flow behaviors.

*Reprinted with permission from "A spectral/hp least-squares finite element analysis of the Carreau–Yasuda fluids," by Namhee Kim and J. N. Reddy, 2016. International Journal for Numerical Methods in Fluids, Vol. 82, pp. 541–566. Copyright 2016 by John Wiley & Sons, Ltd., from "Least-squares finite element analysis of flow of a generalized Newtonian fluid past a circular cylinder," by Namhee Kim and J. N. Reddy, 2018. Mechanics of Advanced Materials and Structures, Vol. 25, pp. 1186–1196. Copyright 2018 by Taylor & Francis, LLC and from "3-D least-squares finite element analysis of flows of generalized Newtonian fluids," by Namhee Kim and J. N. Reddy, 2019. *Journal of Non-Newtonian Fluid Mechanics*, Vol. 266, pp. 143–159. Copyright 2019 by Elsevier, B.V.

5.1 Kovasznay flow

We consider a two-dimensional steady incompressible flow with a periodicity in one direction on a square region of $\bar{\Omega} = [-0.5, 1.5] \times [-0.5, 1.5]$ which may represent the wake behind a periodic array of cylinders (see Figure 5.1). The analytical solution of Kovasznay [76] is given by

$$v_x = 1 - e^{\lambda x}\cos(2\pi y), \quad v_y = \frac{\lambda}{2\pi} e^{\lambda x}\sin(2\pi y), \quad p = p_{ref} - \frac{1}{2}e^{2\lambda x}. \tag{5.1}$$

The parameter λ is defined as $\lambda = \frac{\mathrm{Re}}{2} - \left(\frac{\mathrm{Re}^2}{4} + 4\pi^2\right)^{1/2}$ and p_{ref} is a reference pressure which is set to zero in this study. The computational domain is discretized into a uniform 4×4 mesh of rectangular elements as in Figure 5.1. The velocity boundary conditions are specified along the whole boundary using the exact solutions for velocity components ($v_x,\ v_y$) given by Eq. (5.1). The pressure is prescribed at the single point $\mathbf{x} = (0.5, -0.5)$. The convergence was declared when the relative Euclidean norm of the difference between two consecutive iteration solutions is less than 10^{-4}. The numerical solution of horizontal velocity (v_x) contour for Re = 40 is shown in Figure 5.2, where the polynomial order of 11 is used. In Figure 5.3, we present how the square root of the L_2 least-squares functional (Eq. (3.1)) and L_2 norm of the difference between the exact solution and numerical solution for each field variable (velocity, pressure, and stress) decay as the polynomial order, p, is increased (not to be confused with pressure p, different font style is used for the polynomial order). Each variable with superscript hp in Figure 5.3 denotes numerical solutions. We can observe that the present least-squares finite element model of stress-based first-order system can achieve spectral convergence even though the least-squares functional is not H^1-norm equivalent according to the relevant a priori estimate. Also, to confirm the conservations of mass and momentum, we plot the least-squares functionals for the continuity equation ($\mathcal{J}_{mass}$), for the momentum equation ($\mathcal{J}_{mom}$), for the stress equation ($\mathcal{J}_{stress}$), and for all equations ($\mathcal{J}$ of

Eq. (3.1)) with increasing polynomial order in Figure 5.4, where

$$\mathcal{J}_{mass} = \frac{1}{2} \left\| \boldsymbol{\nabla} \cdot \mathbf{v} \right\|^2_{\Omega,0} \tag{5.2a}$$

$$\mathcal{J}_{mom} = \frac{1}{2} \left\| \mathbf{v} \cdot \boldsymbol{\nabla} \mathbf{v} + \boldsymbol{\nabla} p - \boldsymbol{\nabla} \cdot \underline{\boldsymbol{\tau}} \right\|^2_{\Omega,0} \tag{5.2b}$$

$$\mathcal{J}_{stress} = \frac{1}{2} \left\| \underline{\boldsymbol{\tau}} - \mu \left(\boldsymbol{\nabla} \mathbf{v} + \boldsymbol{\nabla} \mathbf{v}^{\mathrm{T}} \right) \right\|^2_{\Omega,0} . \tag{5.2c}$$

All the least-squares functionals are decayed exponentially under p-refinement, which shows that higher p-level can improve mass and momentum conservation.

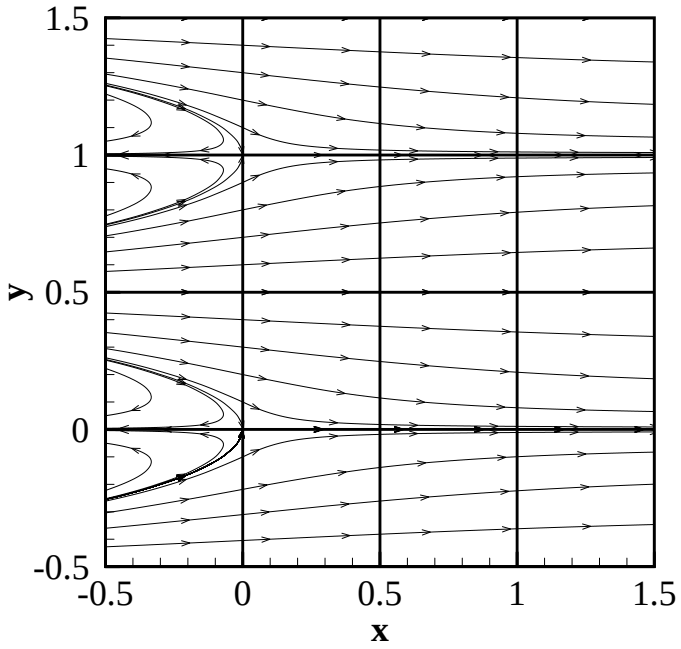

Figure 5.1: Mesh for the problem and numerical result of the streamlines for Re=40.

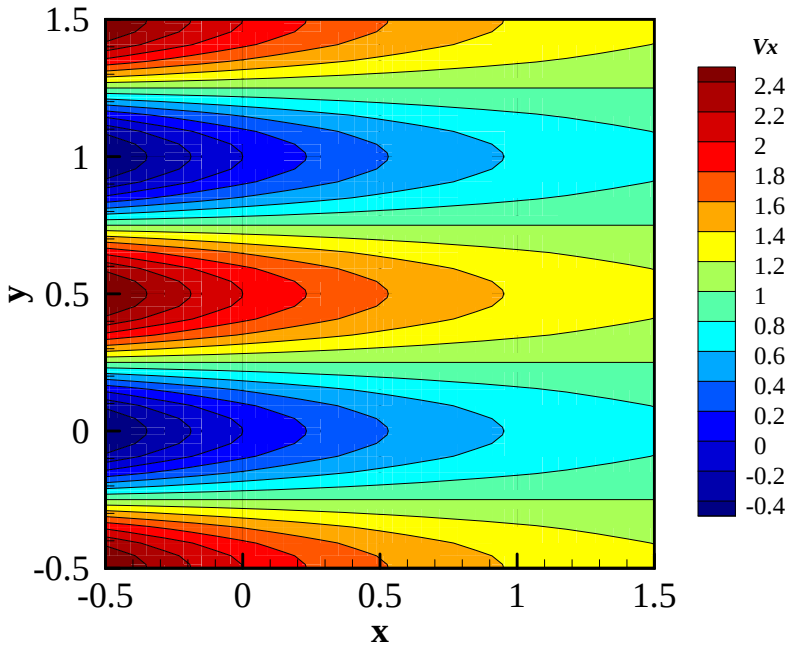

Figure 5.2: Numerical result of horizontal velocity (v_x) contour for Re=40.

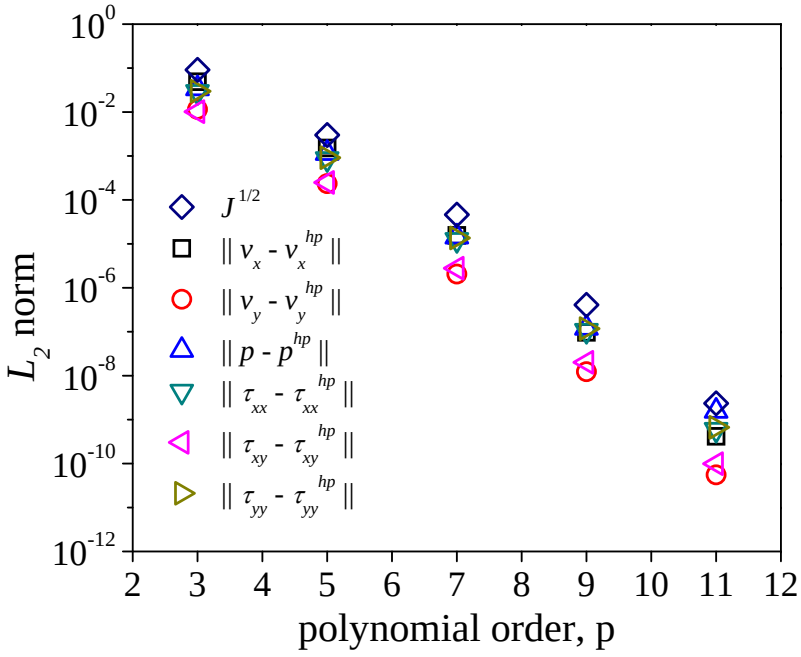

Figure 5.3: Convergence of velocity, pressure, and stress field to the exact solution of Kovasznay flow for Re=40.

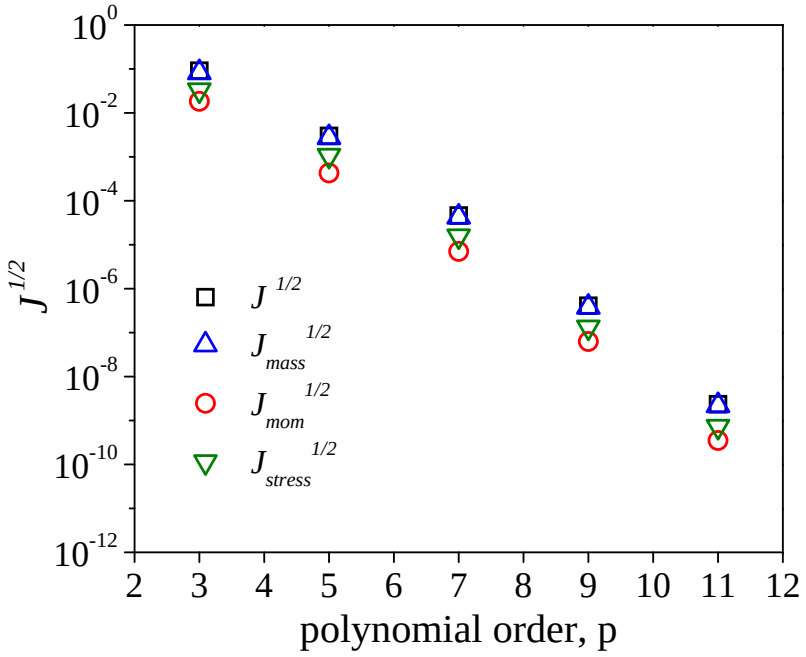

Figure 5.4: Decay of the square root of least-squares functionals for continuity (J_{mass}), momentum (J_{mom}), stress (J_{stress}), and all equations (J).

Using the Kovasznay solution with the same mesh of Figure 5.1, we compared the present stress-based LSFEM having spectral basis with that having traditional Lagrange basis (of equally-spaced nodes). Figure 5.5 presents the L_2 norm of the difference between the analytical solution and numerical solution for all field variables, $\|\Delta - \Delta^{hp}\|$, as a function of polynomial order, p, where

$$\|\Delta - \Delta^{hp}\| = \big(|v_x - v_x^{hp}|^2 + |v_y - v_y^{hp}|^2 + |p - p^{hp}|^2 + |\tau_{xx} - \tau_{xx}^{hp}|^2 + |\tau_{xy} - \tau_{xy}^{hp}|^2 + |\tau_{yy} - \tau_{yy}^{hp}|^2\big)^{1/2}. \tag{5.3}$$

The finite element model with spectral basis shows exponential decay under p-refinement. However, for the finite element model with Lagrange basis, the error grows when p is larger than 8, which is related to the increasing interpolation error of higher p-level. Thus, we can see that the LSFEM with spectral basis can yield more accurate results compared to that with Lagrange basis for higher polynomial orders.

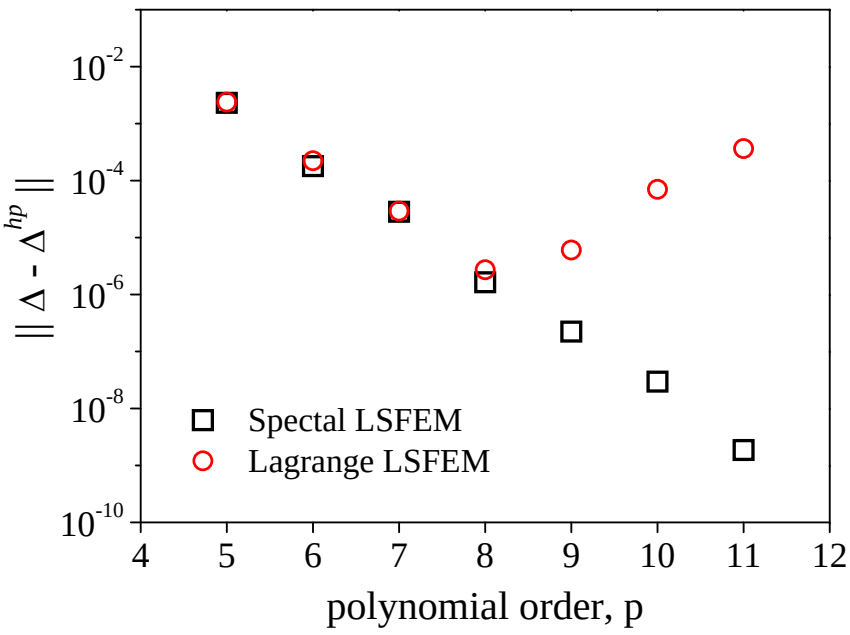

Figure 5.5: Convergence of the field variables to the exact solution of Kovasznay flow for Re=40.

5.2 Jeffery-Hamel flow in a diverging channel

We studied another example having an analytical solution. The flow of a viscous incompressible fluid between nonparallel plane walls possesses exact solution which Jeffery [77] and Hamel [78] found independently, and it is called Jeffery-Hamel flow. For the flow between asymmetric curved walls, exact solutions was found by Schobeiri [79, 80]. Jeffery-Hamel flow has two types of flow; the flow in a diverging channel and the one in a converging channel. The diverging flow is assumed to have a line source at the intersection of walls and the converging flow is assumed to have a line sink at the intersection of walls [81]. The flow is purely radial and the velocity profile is self-similar at all radii when normalized with respect to the centerline velocity at a given radius [82, 83]. We considered a flow in a diverging channel as shown in Figure 5.6. The divergence $\alpha = 5^{\circ}$ is the angle between the centerline and wall. Reynolds number of 684 is used for which the velocity profile is symmetric about the centerline and thus only half of the domain is considered as shown in Figure 5.7.

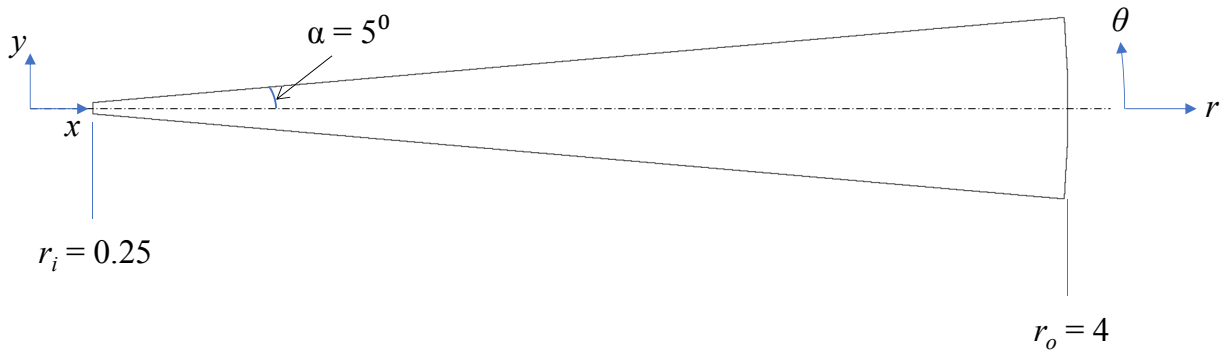

Figure 5.6: Schematic of Jeffery-Hamel flow in a diverging channel.

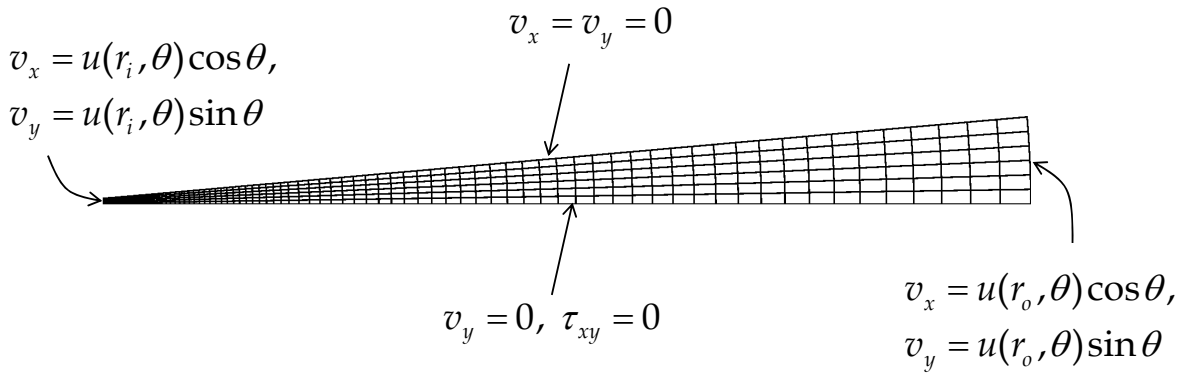

Figure 5.7: Boundary conditions and mesh for the problem.

For the boundary conditions in Figure 5.7, the analytical solution given by Eq. (5.4) was imposed across both inlet and outlet of the channel [81, 84].

$$u(r,\theta) = \frac{F(\theta)}{F_o}\frac{1}{\alpha r}, \quad \frac{F(\theta)}{F_o} = 1 - \frac{6m^2k^2sn^2(m\theta,k)}{6m^2k^2sn^2(m\alpha,k)}, \tag{5.4}$$

where $m = \left(\frac{1+\mathrm{Re}/2}{1+k^2}\right)^{1/2}$, $\mathrm{Re} = \frac{u_0 r}{\nu}$ with u_0 being the centerline velocity and ν kinematic viscosity. sn denotes a Jacobian elliptic function and k is an elliptic modulus which is a solution

of transcendental equation given by

$$sn^2(m\alpha, k) = \frac{1+k^2}{3k^2\,(1+2/\mathrm{Re})}. \tag{5.5}$$

The detailed procedure of obtaining the analytical solution of the problem is well described in [81]. No-slip condition ($v_x = v_y = 0$) was applied to the wall. On the centerline, vertical velocity (v_y) and viscous shear stress (τ_{xy}) are set to zero. Pressure is specified ($p = 0$) at one point which is located at the intersection of the wall and outlet. The computational domain is discretized into non-uniform 126 elements as in Figure 5.7. The convergence was declared when the relative Euclidean norm of the difference between two consecutive iteration solutions is less than 10^{-3}. The numerical result for velocity of Re = 684 is presented in Figure 5.8, where the polynomial order of 7 is used. The numerical result shows very good agreement with the exact solution. To examine the conservations of mass and momentum, we plot the least-squares functionals for the continuity equation ($\mathcal{J}_{mass}$), for the momentum equation ($\mathcal{J}_{mom}$), for the stress equation ($\mathcal{J}_{stress}$), and for all equations ($\mathcal{J}$ of Eq. (3.1)) with increasing polynomial order in Figure 5.9. All the least-squares functionals are decayed exponentially under p-refinement, which tells that higher p-level can improve mass and momentum conservation.

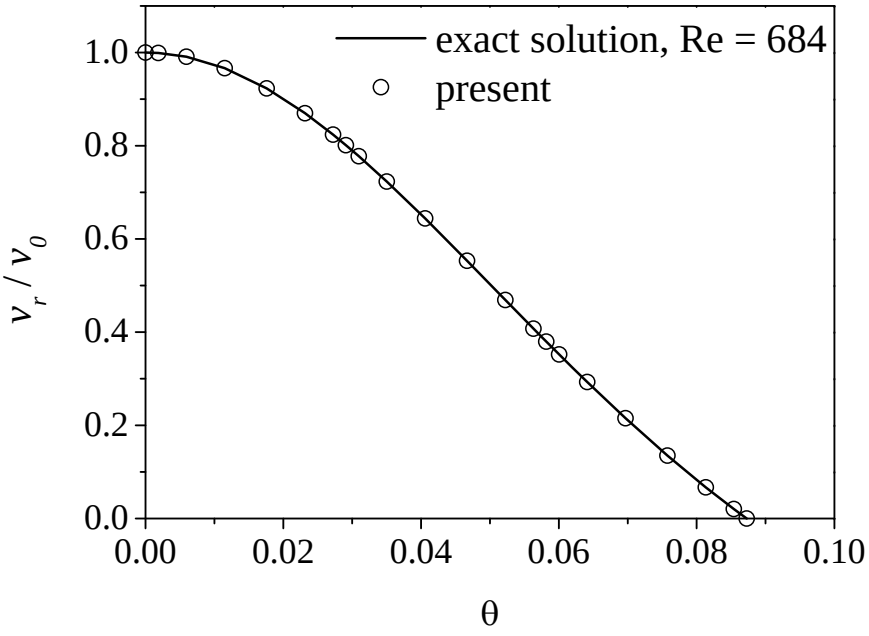

Figure 5.8: Velocity profile at $r = 1$ for Re=684.

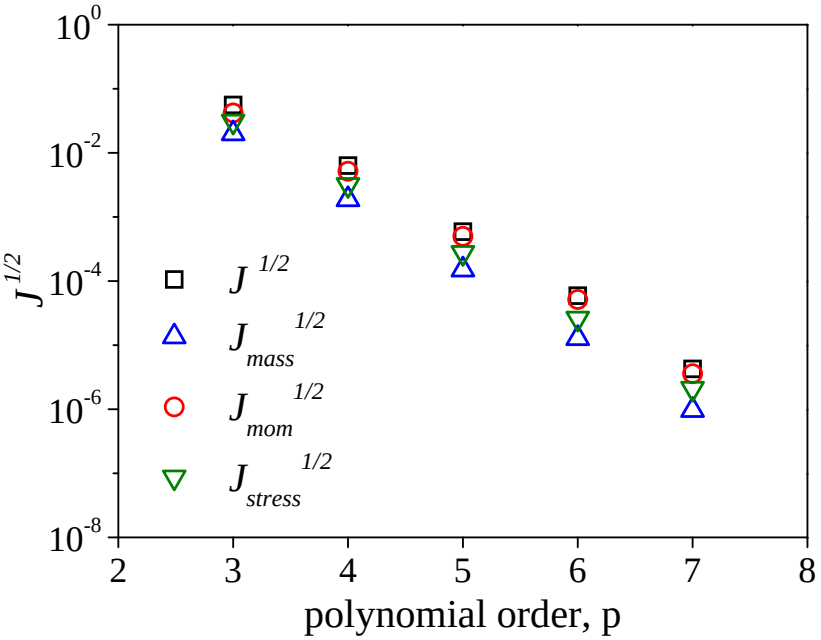

Figure 5.9: Decay of the square root of least-squares functionals for continuity (J_{mass}), momentum (J_{mom}), stress (J_{stress}), and all equations (J).

5.3 Method of manufactured solutions

The method of manufactured solutions (MMS) was used to verify exponential convergence of the present LSFEM for Newtonian fluid flows. In MMS, one manufactures a solution, which is smooth, and applies it to a partial differential equation or a set of partial differential equations to find the source terms [85]. We consider the following manufactured solution of 3-D steady incompressible flow.

$$\begin{aligned} v_x(x,y,z) &= u_0 \left[\sin\left(x^2+2y^2+3z^2\right)+\epsilon\right] \\ v_y(x,y,z) &= v_0 \left[\cos\left(x^2+2y^2+3z^2\right)+\epsilon\right] \\ v_z(x,y,z) &= w_0 \left[\cos\left(3x^2+y^2+2z^2\right)+\epsilon\right] \\ p(x,y,z) &= p_0 \left[\sin\left(3x^2+y^2+2z^2\right)+2.0\right], \end{aligned} \tag{5.6}$$

where the constants used are $u_0 = 1.0$, $v_0 = 1.0$, $w_0 = 1.0$, $p_0 = 1.0$, and $\epsilon = 0.001$. The solution given in Eq. (5.6) is a similar form with 2-D manufactured solutions of Salari and Patrick [85]. Since the manufactured solution does not satisfy the conservation of mass and momentum, substituting Eq. (5.6) into the governing equations of Eq. (2.3) (with $\mathbf{f} = 0$) leads to residual terms, which are treated as source terms. The source terms for the continuity equation (S_{mass}) and for the momentum equation ($\mathbf{S}_{mom}$) are generated using Maple, which is a symbolic manipulation tool. Then, we implement these source terms within the finite element code and seek the finite element solutions of Eq. (2.3) added with the source terms. Then the difference between the numerical solution and the manufactured solution is evaluated. The computational domain of $\bar{\Omega} = [-0.1, 0.7] \times [0.2, 0.8] \times [0.0, 0.4]$ is used to avoid symmetry in the solution. $\bar{\Omega}$ is discretized into a uniform $4 \times 3 \times 2$ mesh of rectangular elements as in Figure 5.10. The Dirichlet boundary condition is imposed along the whole boundary and the values are computed from the manufactured solution, Eq. (5.6). The convergence was declared when the relative Euclidean norm of the difference between two consecutive iteration solutions, γ, is less than 10^{-4}.

$$\gamma = \frac{\|\Delta^{(k)} - \Delta^{(k-1)}\|}{\|\Delta^{(k)}\|}, \tag{5.7}$$

where $\|\cdot\|$ denotes the Euclidean norm, $\Delta^{(k)}$ is the current solution, and $\Delta^{(k-1)}$ is the solution known from the previous iteration.

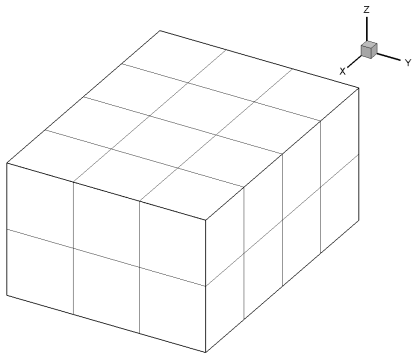

Figure 5.10: Mesh for the problem.

In Figure 5.11, we present the L_2 norm of the difference between the manufactured solution and the numerical solution for each and all field variables, $\|\Delta - \Delta^{hp}\|$, with respect to polynomial order, p (not to be confused with pressure p, different font style is used for the polynomial order), where

$$\begin{aligned}\|\Delta - \Delta^{hp}\| = \big(&|v_x - v_x^{hp}|^2 + |v_y - v_y^{hp}|^2 + |v_z - v_z^{hp}|^2 + |p - p^{hp}|^2 + \\ &|\tau_{xx} - \tau_{xx}^{hp}|^2 + |\tau_{xy} - \tau_{xy}^{hp}|^2 + |\tau_{xz} - \tau_{xz}^{hp}|^2 \\ &|\tau_{yy} - \tau_{yy}^{hp}|^2 + |\tau_{yz} - \tau_{yz}^{hp}|^2 + |\tau_{zz} - \tau_{zz}^{hp}|^2\big)^{1/2}.\end{aligned} \tag{5.8}$$

Each variable with superscript hp in (5.8) denotes numerical solutions. Figure 5.11 shows that the present 3-D LSFEM of stress-based first-order system can achieve exponential convergence. Figure 5.12 presents the least-squares functionals for the continuity equation ($\mathcal{J}_{mass}$), for the momentum equation ($\mathcal{J}_{mom}$), for the stress equation ($\mathcal{J}_{stress}$), and for all equations $\mathcal{J}$ with increasing

polynomial order, where

$$\mathcal{J} = \mathcal{J}_{mass} + \mathcal{J}_{mom} + \mathcal{J}_{stress} \tag{5.9a}$$

$$\mathcal{J}_{mass} = \frac{1}{2} \left\| \boldsymbol{\nabla} \cdot \mathbf{v} - S_{mass} \right\|^2_{\Omega,0} \tag{5.9b}$$

$$\mathcal{J}_{mom} = \frac{1}{2} \left\| \mathbf{v} \cdot \boldsymbol{\nabla}\mathbf{v} + \boldsymbol{\nabla} p - \boldsymbol{\nabla} \cdot \underline{\boldsymbol{\tau}} - \mathbf{S}_{mom} \right\|^2_{\Omega,0} \tag{5.9c}$$

$$\mathcal{J}_{stress} = \frac{1}{2} \left\| \underline{\boldsymbol{\tau}} - \mu \left(\boldsymbol{\nabla}\mathbf{v} + \boldsymbol{\nabla}\mathbf{v}^{\mathrm{T}} \right) \right\|^2_{\Omega,0} . \tag{5.9d}$$

S_{mass} and $\mathbf{S}_{mom}$ are the source terms generated by substituting the manufactured solution into the mass and momentum equations, respectively. We can see that the least-squares functionals decay exponentially under p-refinement, which shows that higher p-level can improve mass and momentum conservation. Figure 5.12 also shows that the values of $\sqrt{\mathcal{J}}$ and L_2 error of Eq. (5.8) are similar and they decay at the same rate. A least-squares functional can be used as a measure of error to the true solution. In terms of the a priori estimate relevant to least-squares models, which are well described in Bochev and Gunzburger [40], Jiang [13], and Bochev and Gunzburger [14], the least-squares functional given in Eq. (3.1) is not H^1-norm equivalent regardless of the choice of boundary conditions. However, the exponential convergence of the present model (Figure 5.12) demonstrates that the optimality of a model cannot be de termined a priori using the standard elliptic theory. Pontaza and Reddy [23] reported the similar observations using the LSFEM based on velocity-pressure-vorticity formulation.

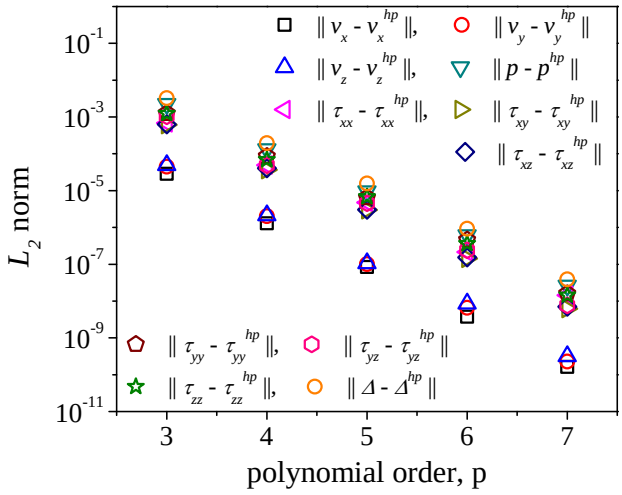

Figure 5.11: Convergence of velocity, pressure, and stress fields to the manufactured solution.

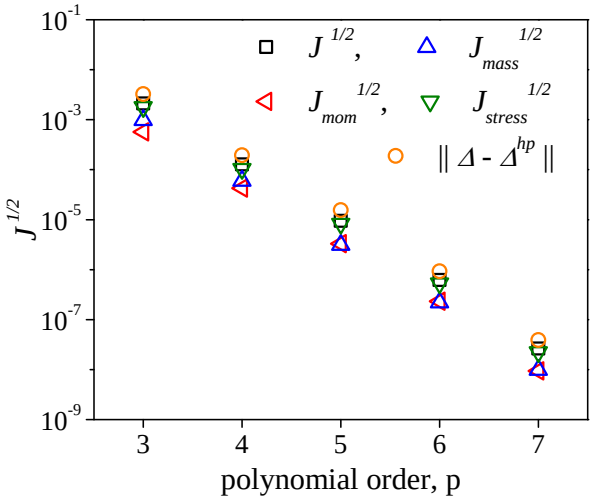

Figure 5.12: Decay of the square root of least-squares functionals for continuity (J_{mass}), momentum (J_{mom}), stress (J_{stress}), all equations (J), and L_2 norm of Eq. (5.8).

5.4 Lid-driven cavity flow

5.4.1 Problem description

The lid-driven cavity flow problem is one of the most studied benchmark problems for fluid mechanics because of its simple geometry but with complex flow phenomena of recirculation [86–88]. We present here two- and three-dimensional flows in a lid-driven cavity.

5.4.1.1 Two-dimensional simulation

The geometry of the computational domain and the boundary conditions for 2-D lid-driven cavity flow are shown in Figure 5.13. The square cavity is bounded by three fixed walls, where the velocity components in x- and y-directions are taken to be zero, and the top boundary (i.e., lid) is assumed to move with the horizontal velocity $v_x = u(x)$ ($v_y = 0$) described by

$$u\left(x\right) = \begin{cases} \tanh\left(50x\right), & \text{if } 0 \leq x \leq 0.5 \\ -\tanh\left(50x - 50\right), & \text{if } 0.5 \leq x \leq 1.0 \end{cases} . \tag{5.10}$$

This hyperbolic tangent approximation makes the velocity profile smooth from zero to unity at the top corners of the cavity where the lid and walls meet, as shown in Figure 5.15. By applying this boundary condition to the lid, we can avoid singularities in the solution to which high-order models are sensitive [5, 33]. In this problem, the characteristic quantities for the Reynolds number and Carreau number of Eq. (2.8) are $v_0 = 1.0$ and $L_0 = L = 1.0$, where v_0 is the lid velocity of Eq. (5.11) when it reaches unity and a is the horizontal dimension of the cavity. The computational domain is discretized into a non-uniform 10×10 mesh of rectangular elements, as shown in Figure 5.14. The mesh is graded such that the boundary layer thickness is resolved. Nonlinear convergence is declared when the Euclidean norm of the difference between two consecutive iteration solutions is less than 10^{-3}.

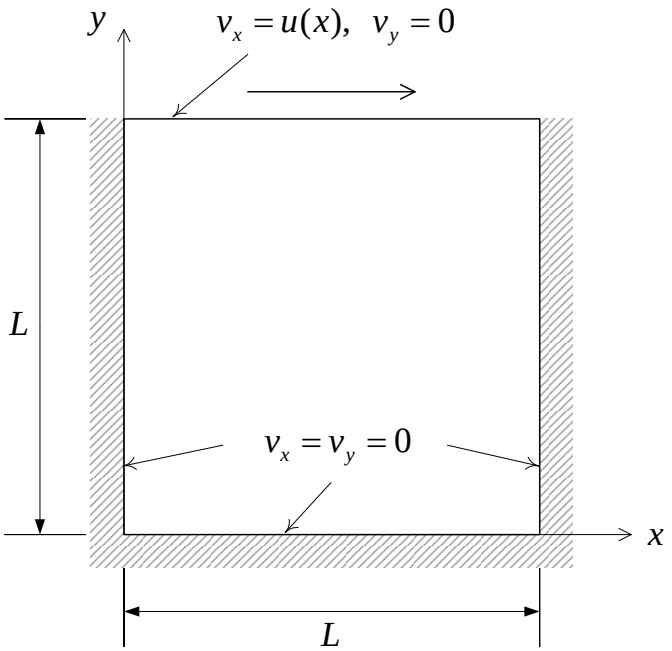

Figure 5.13: Schematic for the problem of lid-driven square cavity flow ($L = 1.0$).

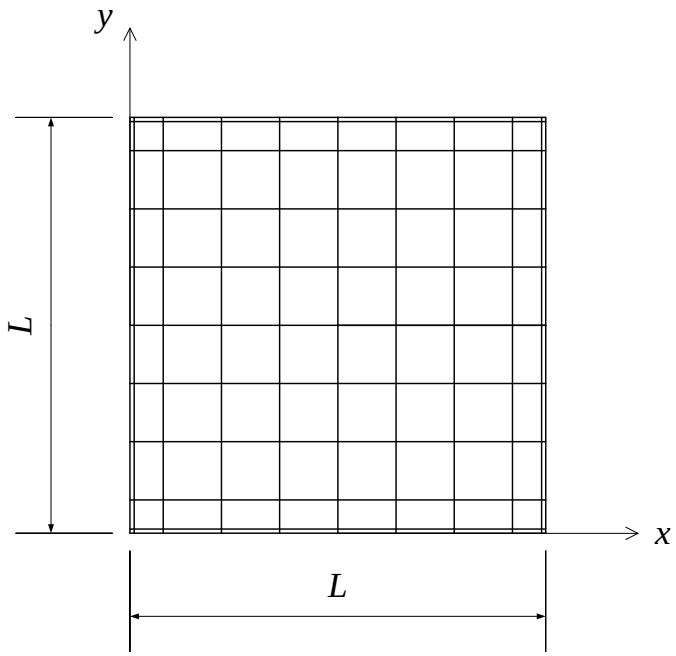

Figure 5.14: Mesh for the problem of lid-driven square cavity flow ($L = 1.0$).

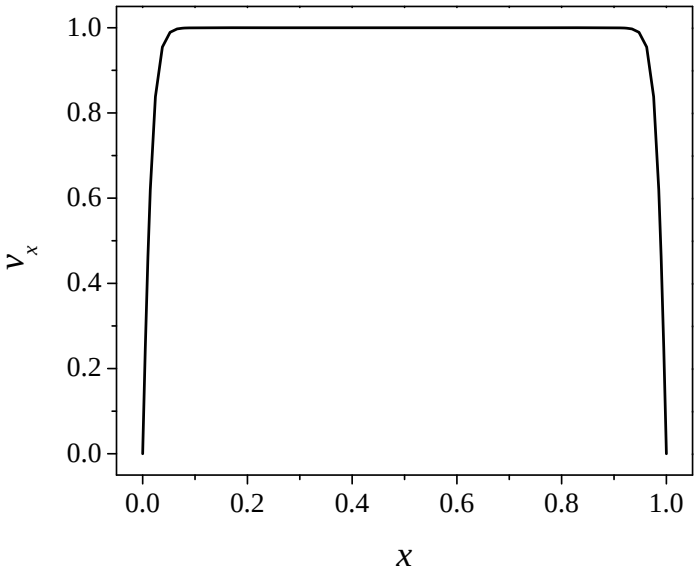

Figure 5.15: Horizontal velocity profile at $y = 1.0$ approximated by hyperbolic tangent.

5.4.1.2 Three-dimensional simulation

The schematic for the problem of 3-D lid-driven cavity flow is shown in Figure 5.16. Fluid is in a cubic cavity, $[-0.5, 0.5] \times [-0.5, 0.5] \times [-0.5, 0.5]$, and the flow is driven by a moving lid at the top. Since the flow is symmetric about the mid-xy-plane (whose edges are red in Figure 5.16)), only half of the domain is considered as shown in Figure 5.17. At the symmetry plane ($z = 0.0$), v_z and shear stresses (τ_{xz} and τ_{yz}) are zero. The top boundary (i.e., lid) is assumed to move with the horizontal velocity $v_x = u(x, z)$ (with $v_y = v_z = 0$) described by

$$u\left(x,z\right) = U_0 \left\{1 - \left(\frac{x}{h}\right)^{18}\right\}^2 \left\{1 - \left(\frac{z}{h}\right)^{18}\right\}^2, \tag{5.11}$$

where the moving lid is at $y = h = 0.5$ and $U_0 = 1.0$ is the maximum lid velocity [89]. This polynomial approximation makes the velocity profile smooth from zero to unity at the top corners of the cavity where the lid and walls meet. By applying this boundary condition to the lid, we can avoid singularities in the solution to which high-order models are sensitive [5, 33]. Other remaining walls have no-slip condition and pressure is specified at one point. In this problem, the

characteristic quantities for the Reynolds number and Carreau number of Eq. (2.8) are $v_0 = U_0 = 1.0$ and $L_0 = 2h = 1.0$, where v_0 is the maximum lid velocity and L_0 is the horizontal dimension of the cavity. The computational domain is discretized into a non-uniform $10 \times 10 \times 5$ mesh of rectangular parallelepiped elements (see Figure 5.17). The mesh is graded such that the flow near the boundaries is resolved. Nonlinear convergence is declared when the Euclidean norm of the difference between two consecutive iteration solutions is less than 10^{-3}.

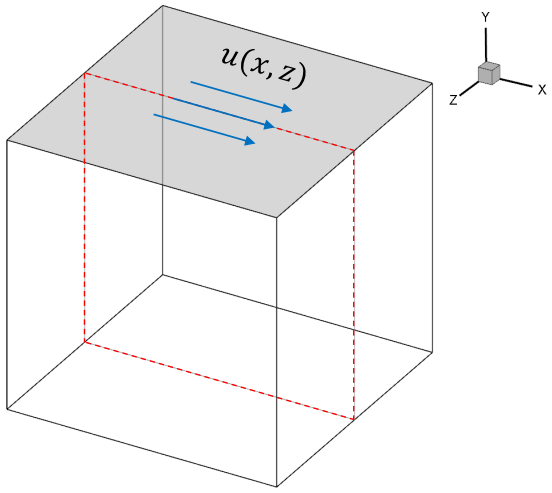

Figure 5.16: Schematic for the problem of lid-driven cubic cavity flow ($[-0.5, 0.5] \times [-0.5, 0.5] \times [-0.5, 0.5]$).

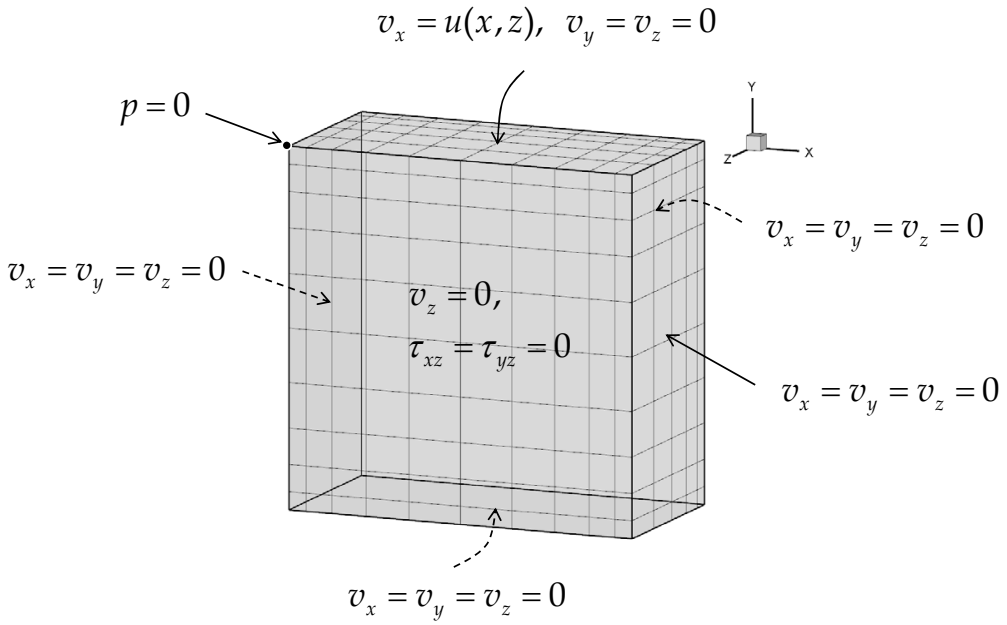

Figure 5.17: Boundary conditions for the problem of lid-driven cubic cavity flow ($[-0.5, 0.5] \times [-0.5, 0.5] \times [-0.5, 0.0]$).

5.4.2 Verification and validation tests

5.4.2.1 Two-dimensional simulation

To verify the present solution for 2-D flow, we compared our results with the previous numerical study of Ghia, Ghia, and Shin [90] for Newtonian fluids first and then compare with Surana and coworkers [61] for non-Newtonian (generalized Newtonian) fluids. By comparing with the work of Ghia, Ghia, and Shin [90] who used a finite difference approximation, we demonstrate the dependency of numerical solutions on polynomial order p. Since it is for Newtonian fluids, we set $n = 1$ in Eq. (2.5), which makes the viscosity constant ($\mu = \mu_0$). Figure 5.18–5.23 show the the horizontal and vertical velocity profiles along the line at $x = 0.5$ and $y = 0.5$ of the cavity, respectively, for several Reynolds numbers (Re = 100, 400, and 1000). For Re = 100 and 400, all velocity profiles are independent of p-levels considered, and are well agreement with the results of Ghia, Ghia, and Shin [90]. For Re = 1000, the velocity curves approach p-independence when p is larger than 5; the velocity curves of p = 5 are slightly different from others around the

lowest values of v_x and around the highest and lowest values of v_y. The converged curves of p = 6, 7, and 8 show good agreement with [90]. Based on these tests, polynomial order of 7 is used for the comparison with the work of Surana and coworkers [61] and for the parameter study of Carreau–Yasuda fluids in the following section. In Figure 5.24–5.25, we plotted the horizontal and vertical velocity curves of present study with those of Surana and coworkers [61] who developed a k-version LSFEM for generalized Newtonian fluids. The parameters applied in Eq. (2.5) are $n = 0.756$, $a = 2.0$, $\lambda_{\text{CY}} = 1.85$, $\mu_0 = 0.45$ and $\mu_\infty = 0$ which are used in [61]. The plots show that the present results are virtually the same as those in [61].

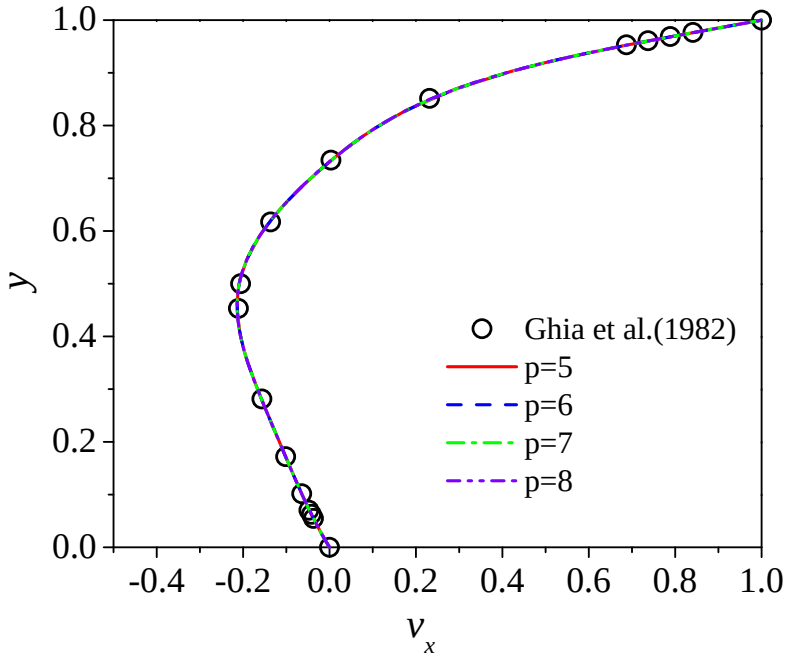

Figure 5.18: Horizontal velocity v_x along the line $x = 0.5$ of the cavity at Re = 100 for Newtonian fluid ($n = 1$).

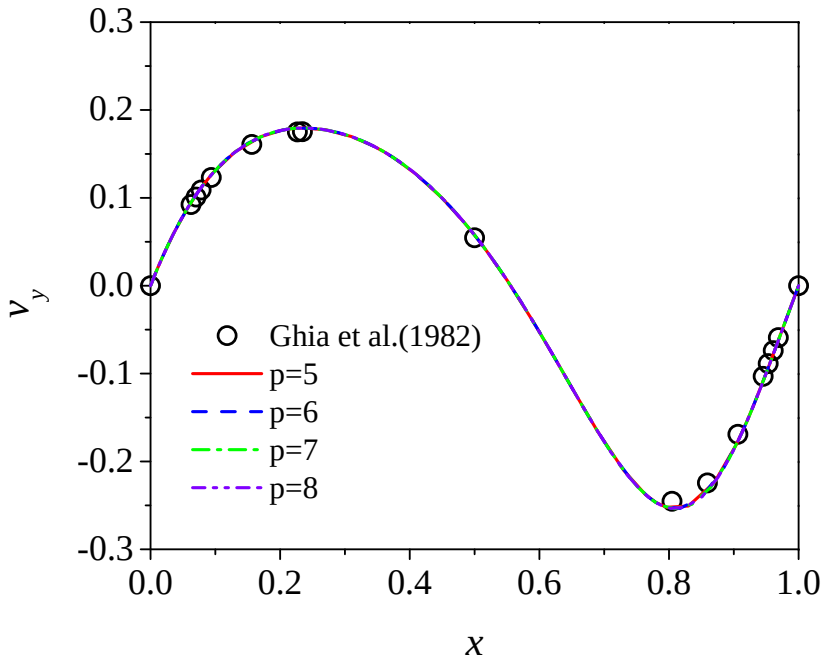

Figure 5.19: Vertical velocity v_y along the line $y = 0.5$ of the cavity at Re = 100 for Newtonian fluid ($n = 1$).

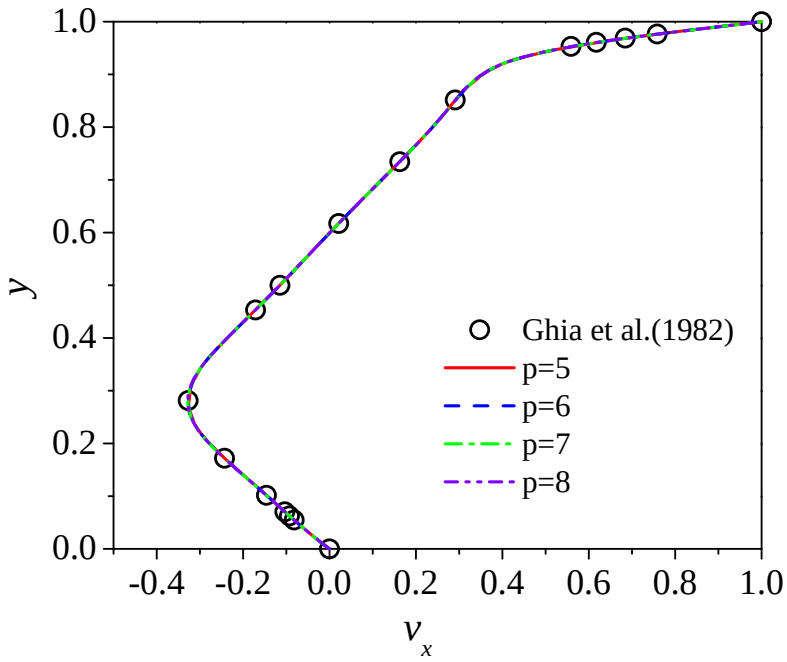

Figure 5.20: Horizontal velocity v_x along the line $x = 0.5$ of the cavity at Re = 400 for Newtonian fluid ($n = 1$).

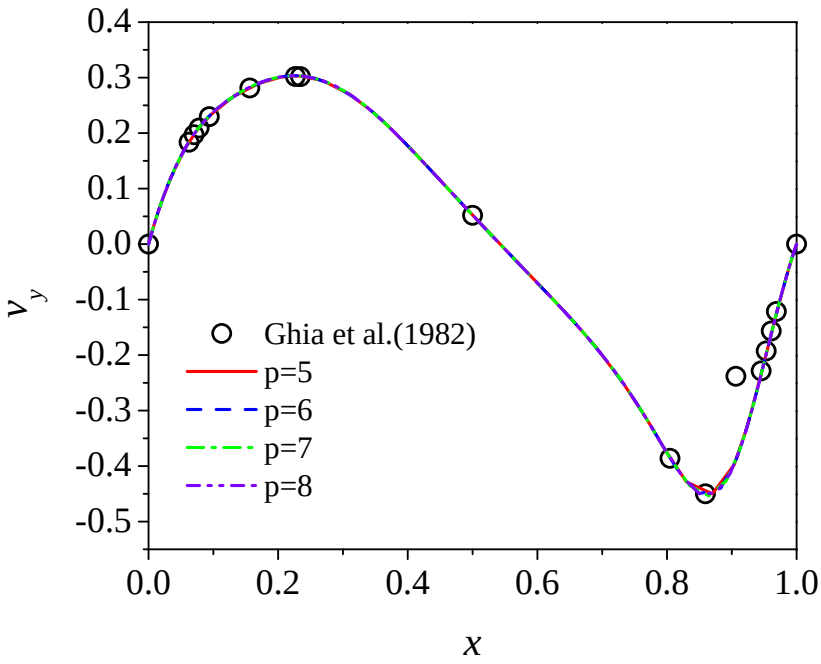

Figure 5.21: Vertical velocity v_y along the line $y = 0.5$ of the cavity at Re = 400 for Newtonian fluid ($n = 1$).

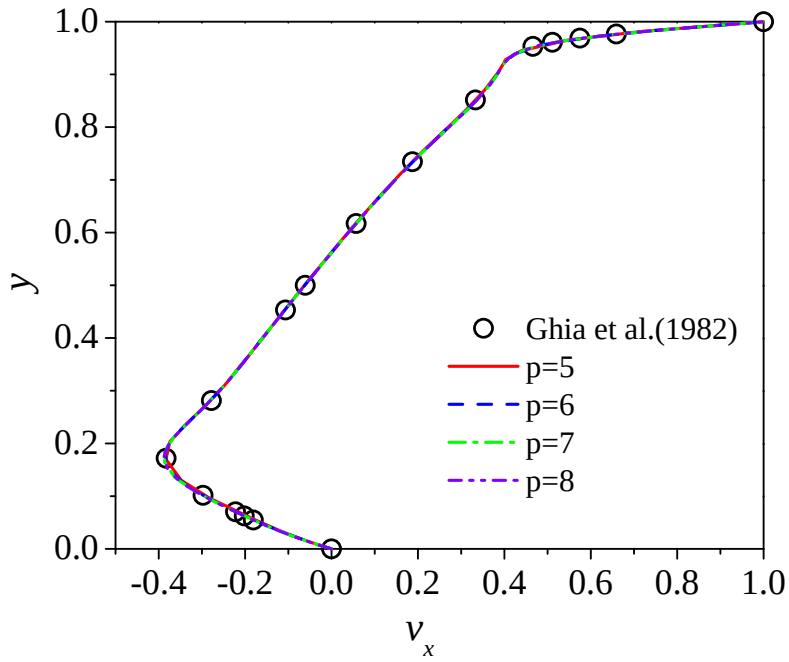

Figure 5.22: Horizontal velocity v_x along the line $x = 0.5$ of the cavity at Re = 1000 for Newtonian fluid ($n = 1$).

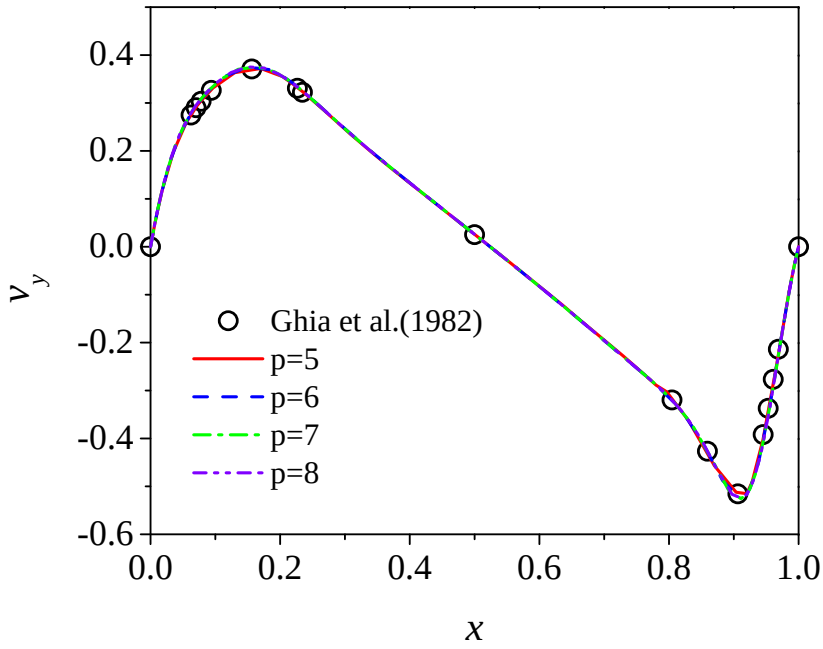

Figure 5.23: Vertical velocity v_y along the line $y = 0.5$ of the cavity at Re = 1000 for Newtonian fluid ($n = 1$).

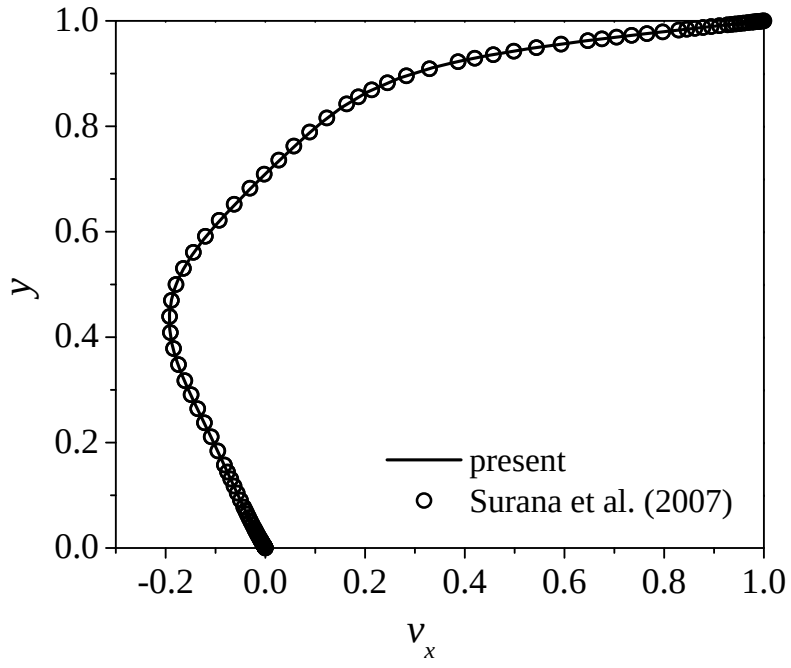

Figure 5.24: Horizontal velocity v_x along the line $x = 0.5$ of the cavity at Re = 100 for non-Newtonian fluid ($n = 0.756, a = 2.0, \lambda_{\text{CY}} = 1.85, \mu_0 = 0.45, \mu_\infty = 0$).

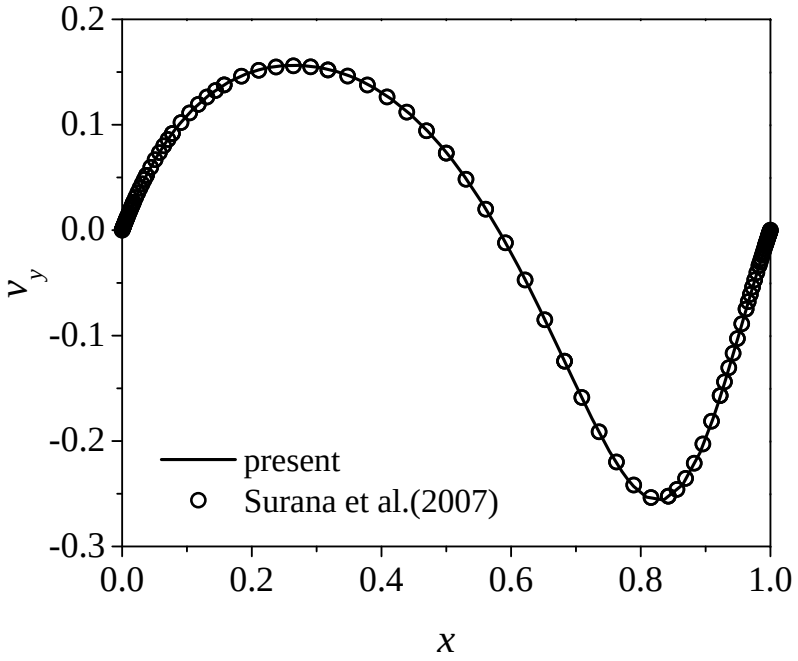

Figure 5.25: Vertical velocity v_y along the line $y = 0.5$ of the cavity at Re = 100 for non-Newtonian fluid ($n = 0.756, a = 2.0, \lambda_{\text{CY}} = 1.85, \mu_0 = 0.45, \mu_\infty = 0$).

5.4.2.2 Three-dimensional simulation

We compared our results with the previous numerical study of Jiang, Lin, and Povinelli [17] for Newtonian fluids. By comparing with the work of Jiang, Lin, and Povinelli [17] who developed a LSFEM based on velocity-pressure-vorticity formulation with $50 \times 52 \times 50$ trilinear elements, we demonstrate the dependency of numerical solutions on polynomial order p. Since it is for Newtonian fluids, we set $n = 1$ in Eq. (2.5), which makes the viscosity constant ($\mu = \mu_0$). Figures 5.26–5.27 show that the horizontal velocity profiles along the line at $x = 0.0$ on the symmetric plane ($z = 0.0$) of the cavity, for two different Reynolds numbers (Re = 100, 400). For Re = 100, all velocity profiles are independent of p-levels considered, and are well agreement with the results of Jiang, Lin, and Povinelli [17]. For Re = 400, the velocity curves approach p-independence when p is larger than 3; the velocity curves of p = 3 are slightly different from others around the lowest values of v_x. The converged curves of p = 4 and 5 show good agreement with [17]. Figures 5.28–5.30 show streamlines on different planes for Re = 100 and 400. p = 5 was used for these results.

In each figure, the red arrow shows the moving direction of the lid. On the planes $z = 0$ (Figure 5.28) and $x = 0$ (Figure 5.29), the main vortices of Re = 400 are located in the lower part than those of Re = 100, and Re = 400 case has the larger secondary vortices at corners (right bottom corner of plane $z = 0$ and right top corer of plane $x = 0$). On the plane $y = 0$ (Figure 5.30), we cannot see any vortex for Re = 100 while there is a vortex near the right upper corner of the plane for Re = 400.

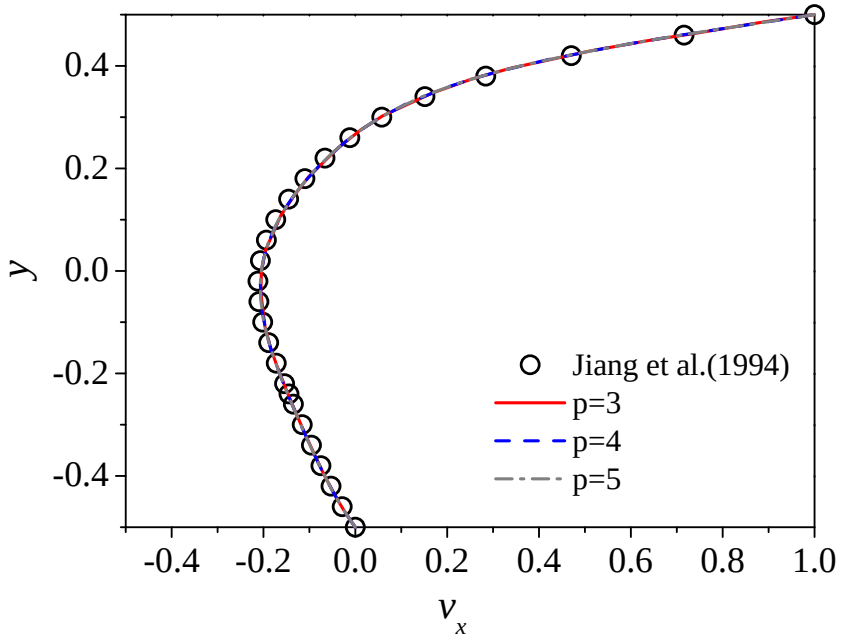

Figure 5.26: Horizontal velocity v_x along the line $x = 0$ on the symmetric plane ($z = 0$) of the cavity at Re = 100 for Newtonian fluid ($n = 1$).

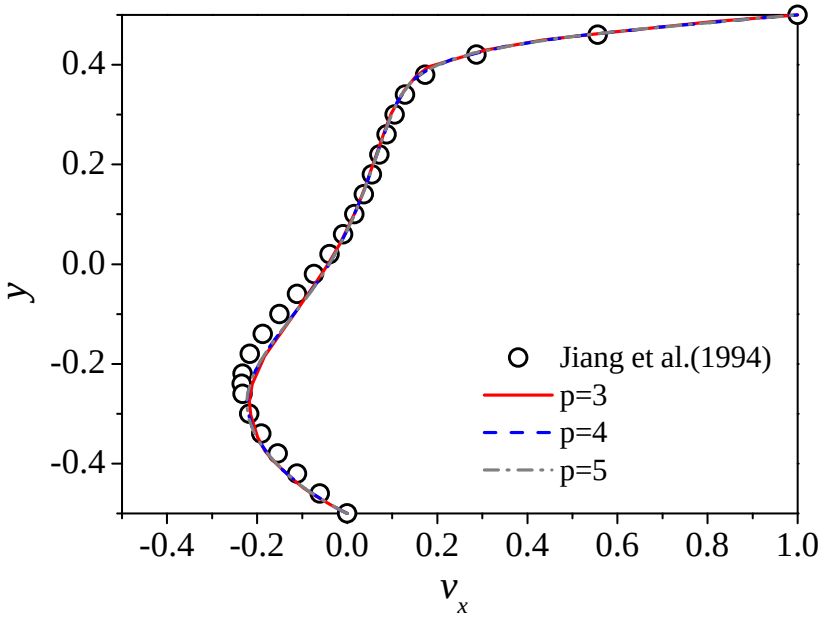

Figure 5.27: Horizontal velocity v_x along the line $x = 0$ on the symmetric plane of the cavity ($z = 0$) at Re = 400 for Newtonian fluid ($n = 1$).

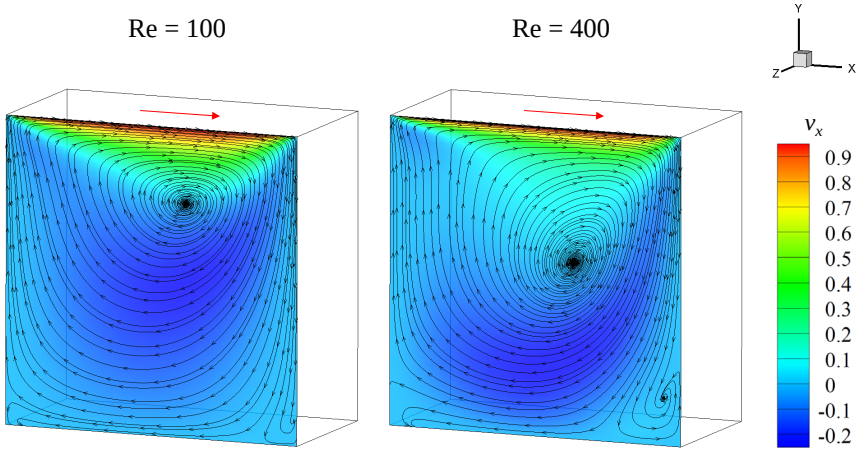

Figure 5.28: Streamlines on plane $z = 0$ at Re = 100 and Re = 400 for Newtonian fluid (with p = 5).

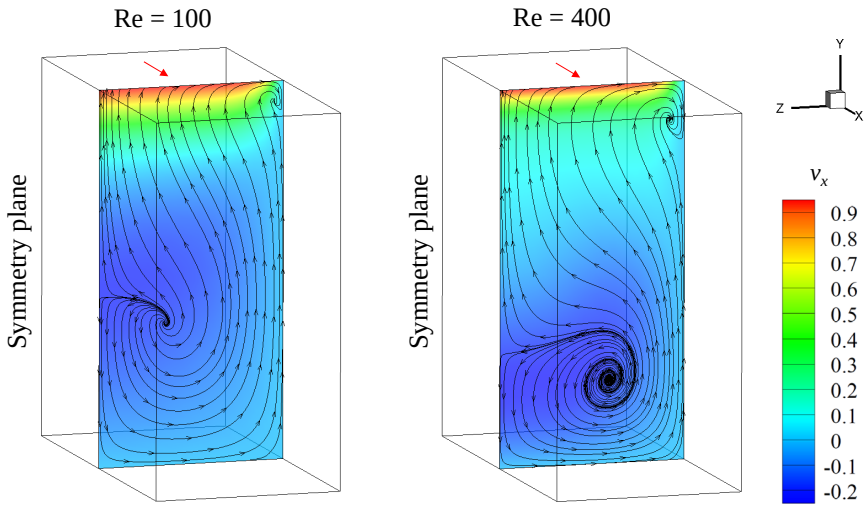

Figure 5.29: Streamlines on plane $x = 0$ at Re = 100 and Re = 400 for Newtonian fluid (with p = 5).

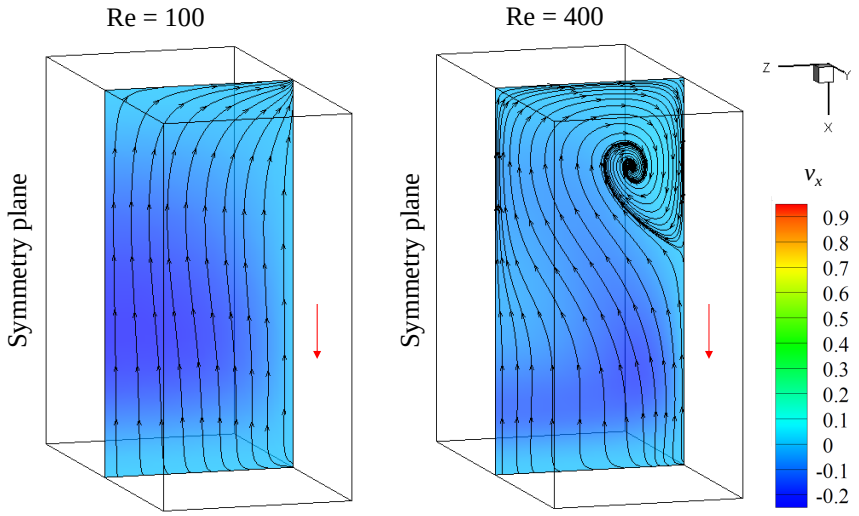

Figure 5.30: Streamlines on plane $y = 0$ at Re = 100 and Re = 400 for Newtonian fluid (with p = 5).

5.4.3 Parametric study of Carreau–Yasuda fluids

In this section, the effects of the three parameters $(a,\ n,\ \lambda_{\mathrm{CY}})$ in the Carreau-Yasuda model, Eq. (2.5), on the flow behavior in a lid-driven square cavity are presented. Since the flow behavior on the symmetry plane of 3-D cavity is similar with that of 2-D cavity, we performed 2-D analysis for parametric study. We focus on the change of horizontal and vertical velocity profiles at the vertical and horizontal mid-lines of the cavity, respectively, by variation of these parameters. The limiting viscosities in Eq. (2.5) are set as $\mu_0 = 100\mu_\infty$. Figures 5.31–5.32, 5.35–5.36, and 5.39–5.40 show that how the cavity flows are affected by the change of $a,\ n$, and λ_{CY}, respectively. In Figs. 5.33–5.34, 5.37–5.38, and 5.41–5.42, the viscosity curves are plotted as a function of shear rate for various $a,\ n$, and λ_{CY}, respectively, and the viscosities at lines $x = 0.5$ and $y = 0.5$ are highlighted by thickening the curves. In Figs. 5.31–5.32, the rate of change in the shapes of the horizontal and vertical velocity profiles, v_x and v_y, grows as a decreases. The reason for this can be explained using Figs. 5.33–5.34, where the rate of change in the shape of viscosity curves at each mid-line ($x = 0.5,\ y = 0.5$) becomes greater with decrease in a, and it causes the flow behavior to be varied accordingly as shown in Figs. 5.31–5.32. Figures 5.35–5.36 present that as n decreases, v_x and v_y deviate more from the Newtonian fluid ($n = 1$) since the slope of power-law region (see Figure 2.1) in viscosity curves for smaller n is more different from that for $n = 1$ (see Figs. 5.37 and 5.38). For the Carreau number (λ_{CY}), increase in λ_{CY} shifts the transition region (transition from the zero-shear-rate plateau to power-law region; see Figure 2.1) of a viscosity curve to lower shear rate, ${I_2}^{1/2}$. This results in the variation of the horizontal and vertical velocities (see Figure 5.39 and 5.40).

Next, let us consider the near-lid-region ($y \sim 1$) at line $x = 0.5$, where the applied horizontal velocity is constant as 1.0 and shear rate is relatively very high. Instead of the lid moving in positive x-direction, we can think conversely that the fluid moves in negative x-direction with the constant velocity beneath the fixed lid where a boundary layer forms. A boundary layer thickness is affected by fluid viscosity; it is reduced as the viscosity decreases. Then, the viscosity at the highest shear rate of each thickened curve (which denotes the viscosity near the lid) in Figs. 5.33, 5.37, and 5.41

can explain the reason of the change in boundary layer thickness due to variation of the parameters a, n, and λ_{CY}. In Figure 5.33, the viscosity of $a = 0.2$ at the highest shear rate is smaller than the others which are relatively close to each other. This leads to the smaller boundary layer thickness near $y = 1$ for $a = 0.2$ than those for $0.5 \leq a \leq 10.0$ whose boundary layer thicknesses near $y = 1$ are almost the same with each other as in Figure 5.31. For the parameter n, the viscosity at the highest shear rate in Figure 5.37 becomes less with decrease in n and, consequently, the boundary layer thickness near $y = 1$ reduces as n decreases (see Figure 5.35). For the Carreau number (λ_{CY}), the viscosity at the highest shear rate in Figure 5.41 is smaller for larger λ_{CY}, which results in the decrease of the boundary layer thickness near $y = 1$ with increasing λ_{CY} (see Figure 5.39).

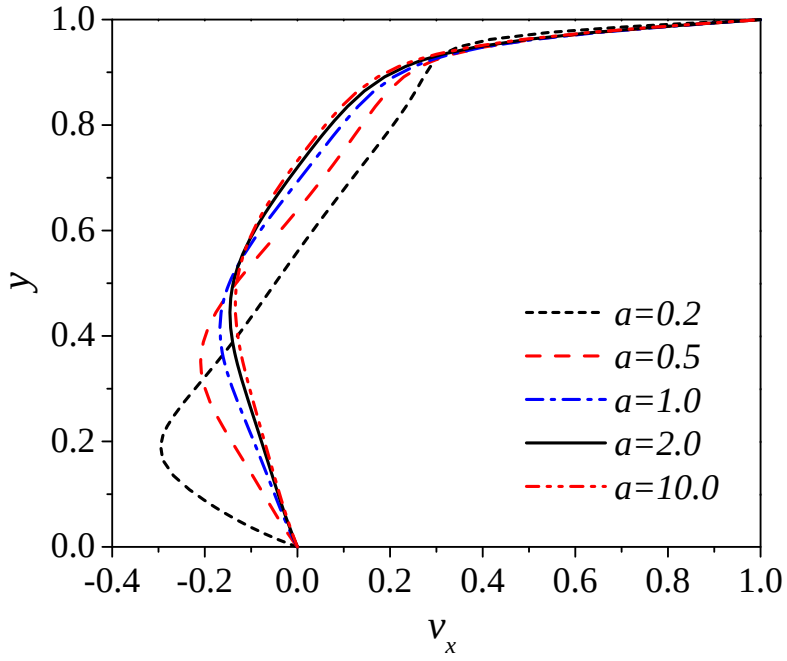

Figure 5.31: Effect of the parameter a on the horizontal velocity v_x at line $x = 0.5$ of the cavity ($n = 0.5$, Re = 100, $\lambda_{\text{CY}} = 1.0$).

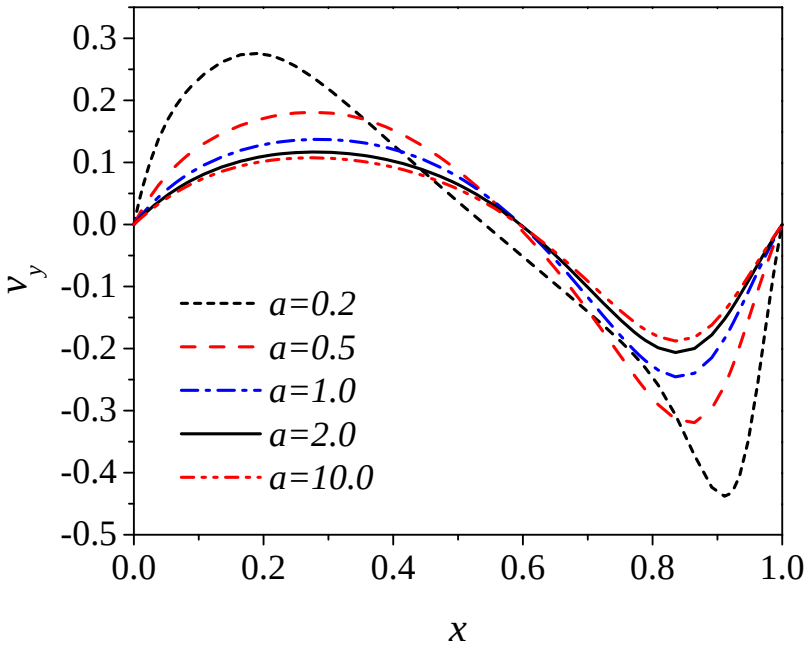

Figure 5.32: Effect of the parameter a on the vertical velocity v_y at line $y = 0.5$ of the cavity ($n = 0.5$, Re = 100, $\lambda_{\mathrm{CY}} = 1.0$).

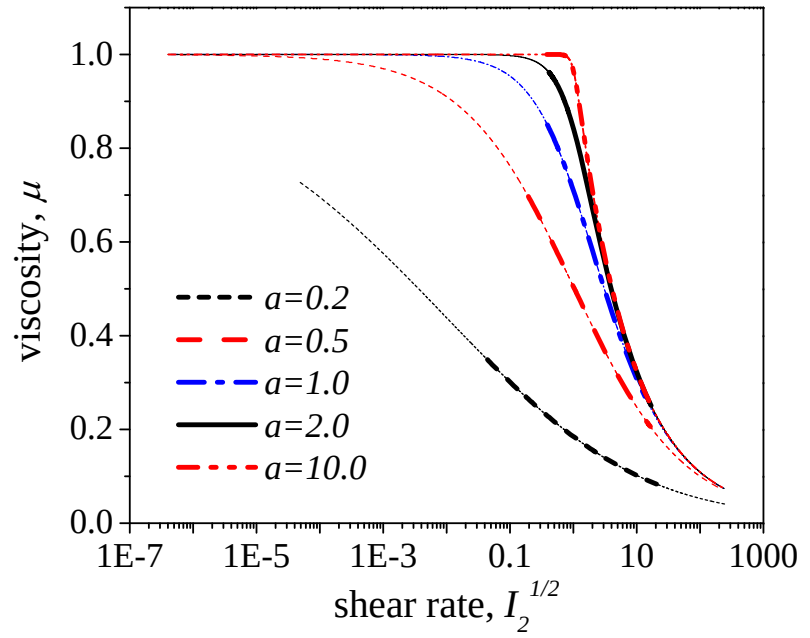

Figure 5.33: Effect of the parameter a on the viscosity at line $x = 0.5$ ($n = 0.5$, Re = 100, $\lambda_{\mathrm{CY}} = 1.0$).

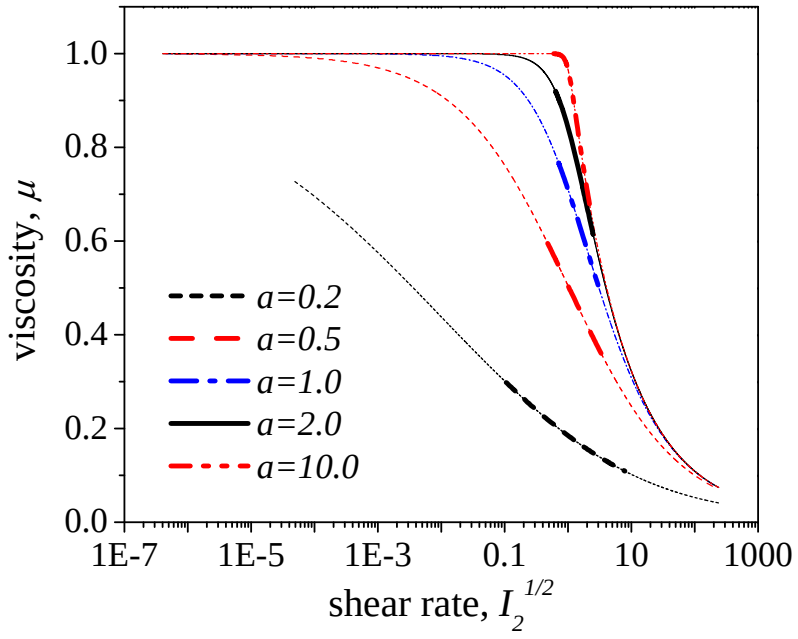

Figure 5.34: Effect of the parameter a on the viscosity at line $y = 0.5$ ($n = 0.5$, Re = 100, $\lambda_{\text{CY}} = 1.0$).

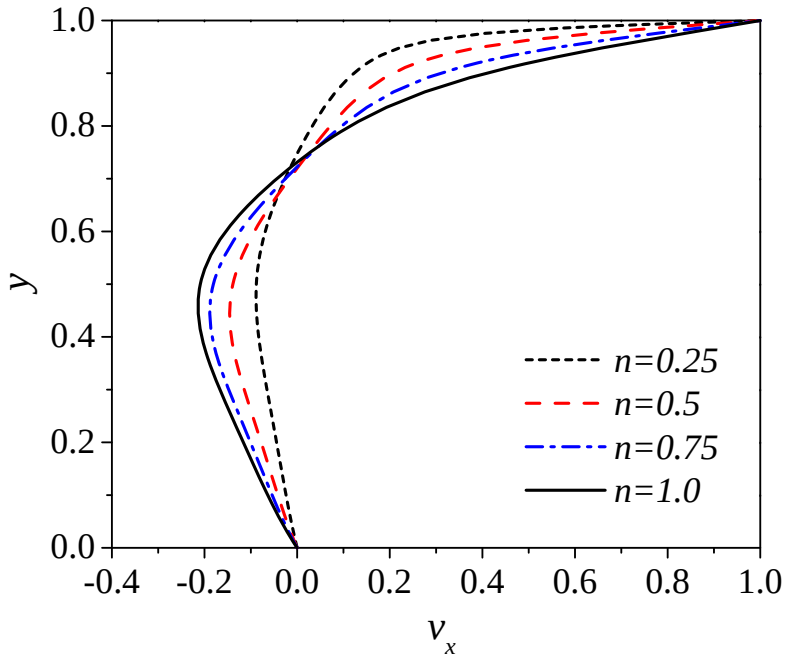

Figure 5.35: Effect of the parameter n on the horizontal velocity v_x at line $x = 0.5$ of the cavity ($a = 2.0$, Re = 100, $\lambda_{\text{CY}} = 1.0$).

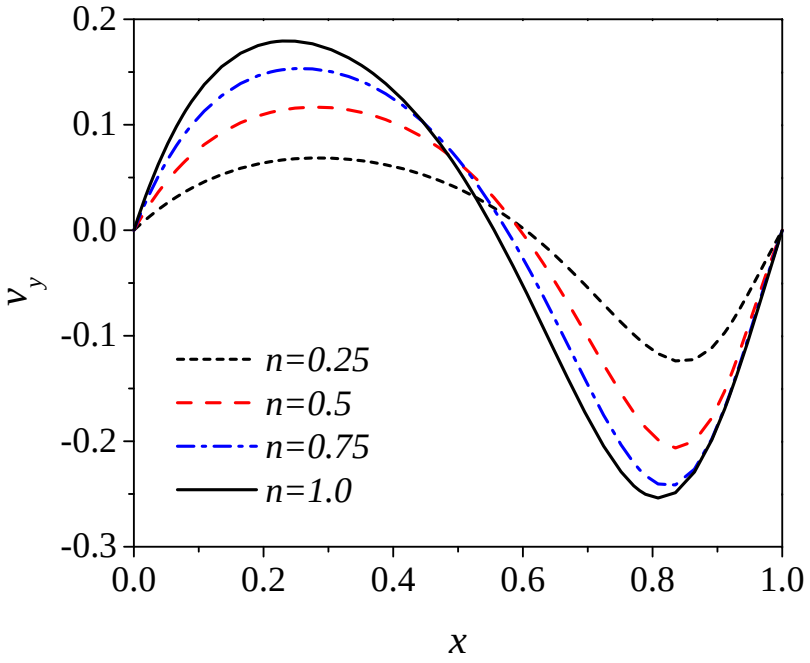

Figure 5.36: Effect of the parameter n on the vertical velocity v_y at line $y = 0.5$ of the cavity ($a = 2.0$, Re = 100, $\lambda_{\text{CY}} = 1.0$).

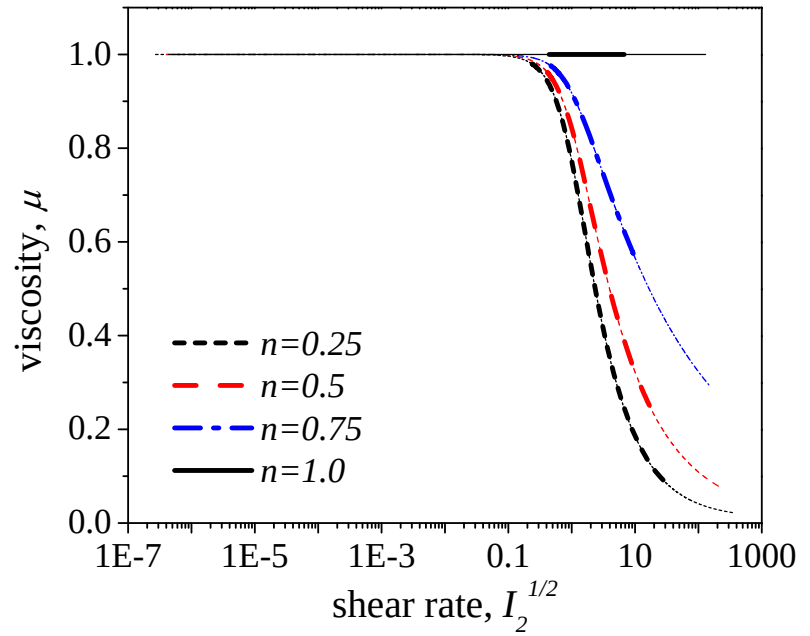

Figure 5.37: Effect of the parameter n on the viscosity at line $x = 0.5$ ($a = 2.0$, Re = 100, $\lambda_{\text{CY}} = 1.0$).

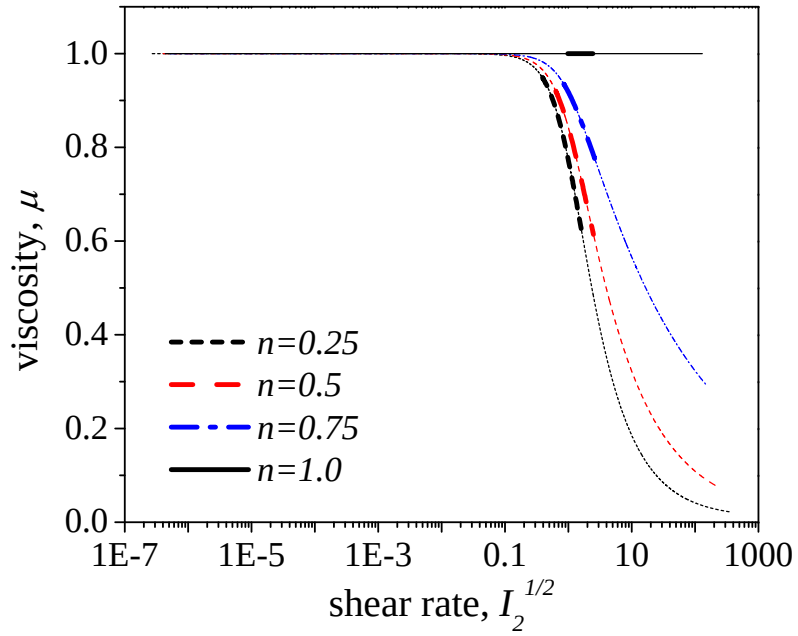

Figure 5.38: Effect of the parameter n on the viscosity at line $y = 0.5$ ($a = 2.0$, Re = 100, $\lambda_{\text{CY}} = 1.0$).

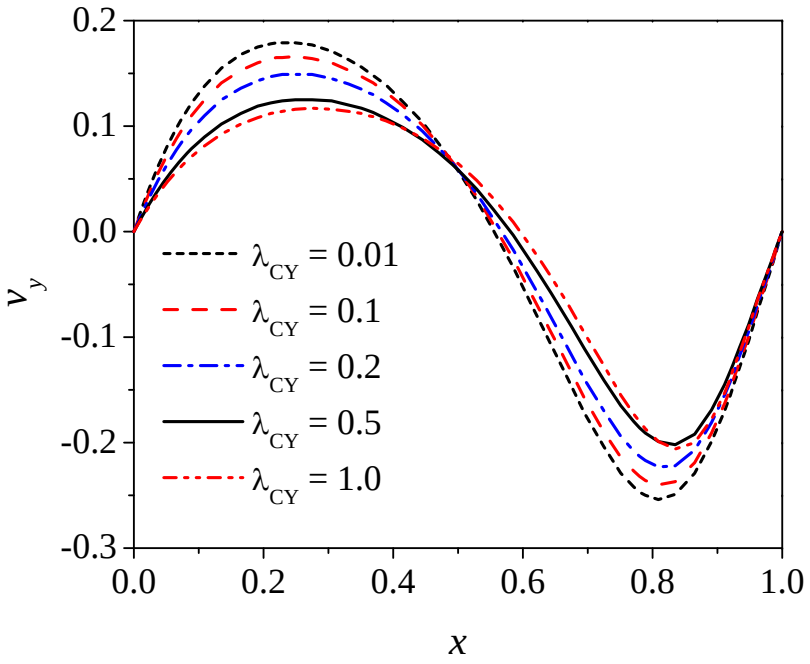

Figure 5.39: Effect of the parameter λ_{CY} on the horizontal velocity v_x at line $x = 0.5$ of the cavity ($a = 2.0$, $n = 0.5$, Re = 100).

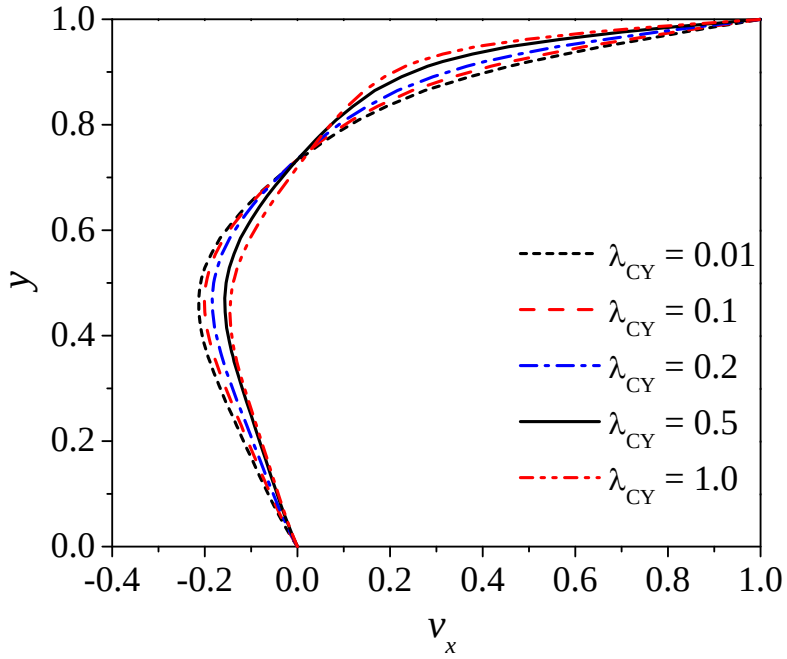

Figure 5.40: Effect of the parameter λ_{CY} on the vertical velocity v_y at line $y = 0.5$ of the cavity ($a = 2.0$, $n = 0.5$, Re = 100).

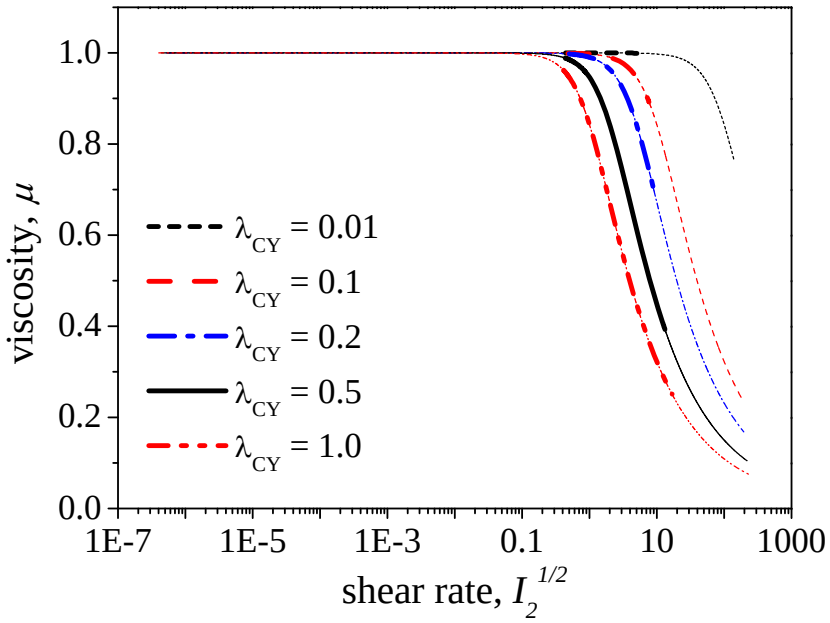

Figure 5.41: Effect of the Carreau number λ_{CY} on the viscosity at line $x = 0.5$ ($a = 2.0$, $n = 0.5$, Re = 100).

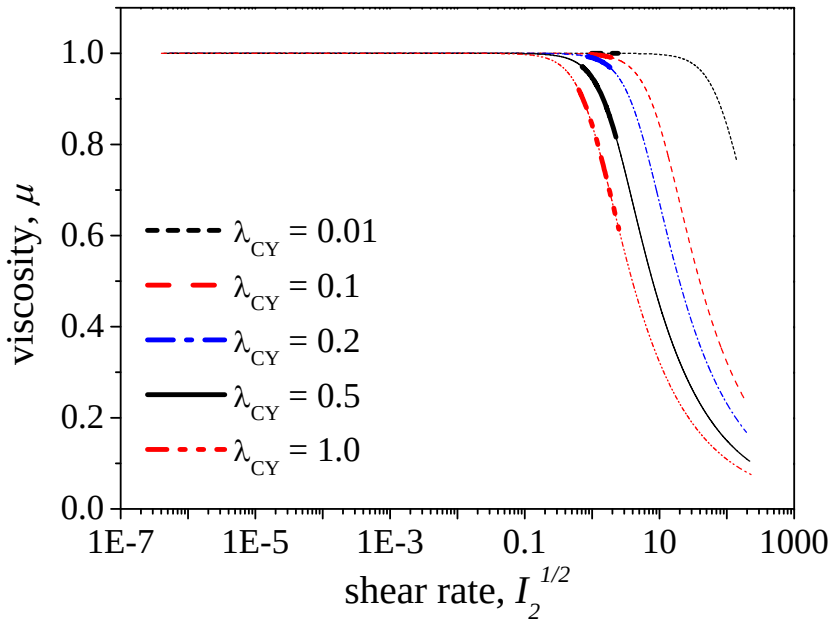

Figure 5.42: Effect of the Carreau number λ_{CY} on the viscosity at line $y = 0.5$ ($a = 2.0$, $n = 0.5$, Re = 100).

5.5 Flow over a backward-facing step

5.5.1 Problem description

The problem of flow over a backward-facing step has been studied by many authors since it is one of the excellent benchmark problems for the accuracy and stability of numerical methods for fluid dynamics. The feature of the problem is that the existence of a backward-facing step induces a recirculation zone downstream of the step and the size of the recirculation zone depends on the Reynolds number [91–94]. We studied two- and three-dimensional flows for this problem.

5.5.1.1 Two-dimensional simulation

The geometry of the computational domain and the boundary conditions for 2-D flows of the problem are taken from the work of Gartling [95] and are shown in Figure 5.43. h and S denote the height of the inlet channel and that of the step, respectively. When comparing with the work of Gartling [95], we set $S = h$ and have the expansion ratio of $(S + h)/h = 2$. When comparing with the work of Armaly et al. [96], we set $S = 0.9423h$ and have the expansion ratio of $(S + h)/h =$

1.9423. The downstream channel length is taken to be $L = 60h$. The fluid entering the inlet channel ($h \leq y \leq S + h$) is assumed as a parallel flow with a horizontal velocity of $v_x = u(y)$ (with $v_y = 0$) given by

$$u(y) = \begin{cases} b_0 + b_1 y + b_2 y^2, & \text{if } S \leq y \leq S + h \\ 0, & \text{if } 0 \leq y \leq S. \end{cases} \tag{5.12}$$

When comparing the present numerical results with the experimental data (v_x for Re=100) of Armaly et al. [96], the coefficients (b_0, b_1, b_2) of Eq. (5.12) were obtained by fitting the experimental data. Otherwise, we assumed that $\bar{v}_x(y) = 24(y - 0.5)(1 - y)$ with (b_0, b_1, b_2) = (-12, 36, -24) as in the work of Gartling [95]. The x- and y-components of velocity are taken to be zero along the top and bottom walls by the no-slip condition. The outflow was assumed to be parallel and to have zero total stress normal to the boundary by taking $v_y = 0$ and $\sigma_{xx} = -p + \tau_{xx} = 0$. Since $\partial v_x/\partial x$ is negligible at the outflow station (i.e., fully developed flow), we take $\tau_{xx} = 0$ and $p = 0$ so that $\sigma_{xx} = 0$. At the top and bottom corners of the outflow station, we set $v_x = v_y = 0$. In this problem, the characteristic quantities for the Reynolds number and the Carreau number of Eq. (2.8) are $v_0 = v_b$ and $L_0 = D_H = 2h$, where v_b is the bulk velocity of the inlet flow, which is equal to two-thirds of the maximum inlet velocity for the laminar flow. D_H is the hydraulic diameter of the inlet channel ($h \leq y \leq 2h$), which is equal to two times the height of inlet channel ($D_H = 2h$), if we assume that the inlet channel has the rectangular cross section with $w \gg h$, w being the width of the channel into the plane of the page. The fluid domain is discretized into a non-uniform 20×2 mesh of rectangular elements as shown in Figure 5.44. The majority of the elements are positioned within $30h$ units of the channel to ensure the accurate resolution of recirculation zone downstream of the step [5, 33]. The convergence is declared when the Euclidean norm of the difference between two consecutive iteration solutions is less than 10^{-3}.

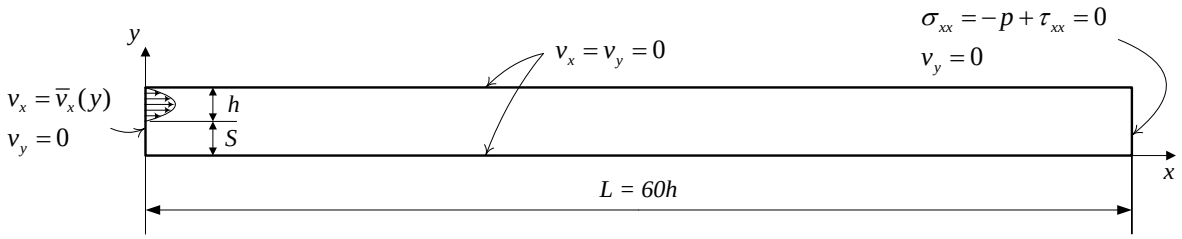

Figure 5.43: Schematic for the problem of backward-facing step flow.

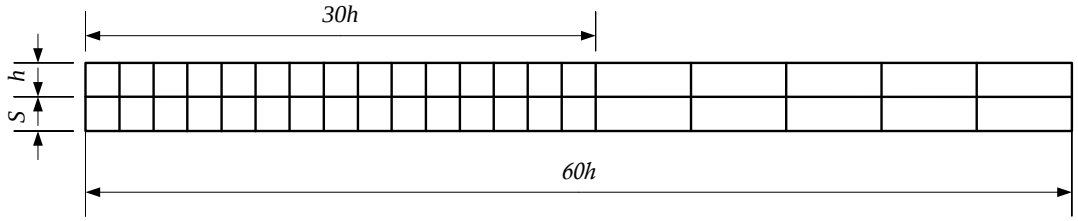

Figure 5.44: Mesh for the problem of backward-facing step flow.

5.5.1.2 Three-dimensional simulation

The schematic for the 3-D flows over the backward-facing step is depicted in Figure 5.45. h and S denote the height of the inlet channel and that of the step, respectively. To compare with the work of Armaly et al. [96], we set $S = 0.9423h$ and so the expansion ratio is $(S + h)/h = 1.9423$. The downstream channel length is $L = 60h$ and the width of the channel is $W = 35h$. Since the flow is symmetric about mid-xy-plane (whose edges are red in Figure 5.45), the half of domain is considered as in Figure 5.46. For the boundary conditions (Figure 5.46), the fluid entering the inlet channel $(h \leq y \leq S + h)$ is assumed as a parallel flow with a horizontal velocity of $v_x = u(y, z)$ (with $v_y = v_z = 0$) given by

$$u(y,z) = \begin{cases} b_0 (y - S) \{y - (S + h)\} \tanh(\beta z), & \text{if } S \leq y \leq S + h \\ 0, & \text{if } 0 \leq y \leq S. \end{cases} \tag{5.13}$$

We have $\beta = 4$, which was obtained by fitting the experimental data for Re=648 in [96]. Since the inlet velocity profile with respect to z-direction was available only at Re=648, we used the fitted value of $\beta = 4$ for the range of Reynolds number ($100 \leq$ Re ≤ 800) in the test. Likewise, the inlet velocity profiles with respect to y-direction were not available for all Re values considered, we used $b_0 = -6/h^2$ as in the work of Gartling [95] for the range of Reynolds number ($100 \leq$ Re ≤ 800). All velocity components are taken to be zero along the top, bottom, and side walls by the no-slip condition. The outflow is assumed to be parallel and to have zero total stress normal to the boundary with $v_y = v_z = 0$ and $\sigma_{xx} = -p + \tau_{xx} = 0$. Since $\partial v_x/\partial x$ is negligible at the outflow station (i.e., fully developed flow), we take $\tau_{xx} = 0$ and $p = 0$ so that $\sigma_{xx} = 0$. At the top and bottom corners of the outflow station, we set $v_x = v_y = v_z = 0$. On the symmetry plane ($z = 8.575$), $v_z = 0$ and $\tau_{xz} = \tau_{yz} = 0$ are imposed. In this problem, the characteristic quantities for the Reynolds number and the Carreau number of Eq. (2.8) are $v_0 = v_b$ and $L_0 = D_H = 2h$, where v_b is the bulk velocity of the inlet flow, which is equal to two-thirds of the maximum inlet velocity for the laminar flow. D_H is the hydraulic diameter of the inlet channel ($h \leq y \leq 2h$), which is equal to two times the height of inlet channel ($D_H = 2h$), assuming that $W(= 35h) \gg h$. The fluid domain is discretized into a non-uniform $16 \times 2 \times 4$ mesh of rectangular parallelepiped elements (see Figure 5.47). The majority of the elements are positioned within left half of the channel to ensure the accurate resolution of recirculation zone downstream of the step [5, 33]. The convergence is declared when the Euclidean norm of the difference between two consecutive iteration solutions is less than 10^{-3}.

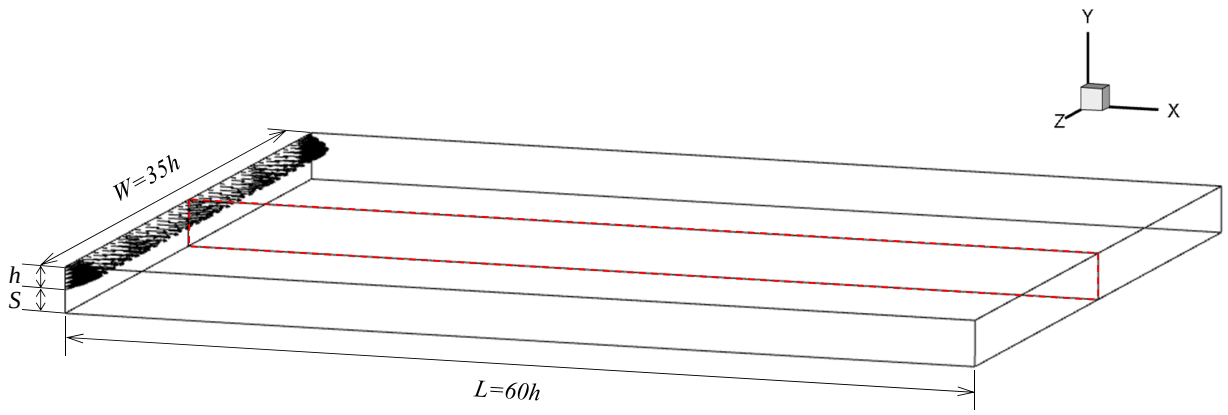

Figure 5.45: Schematic for the problem of 3-D backward-facing step flow.

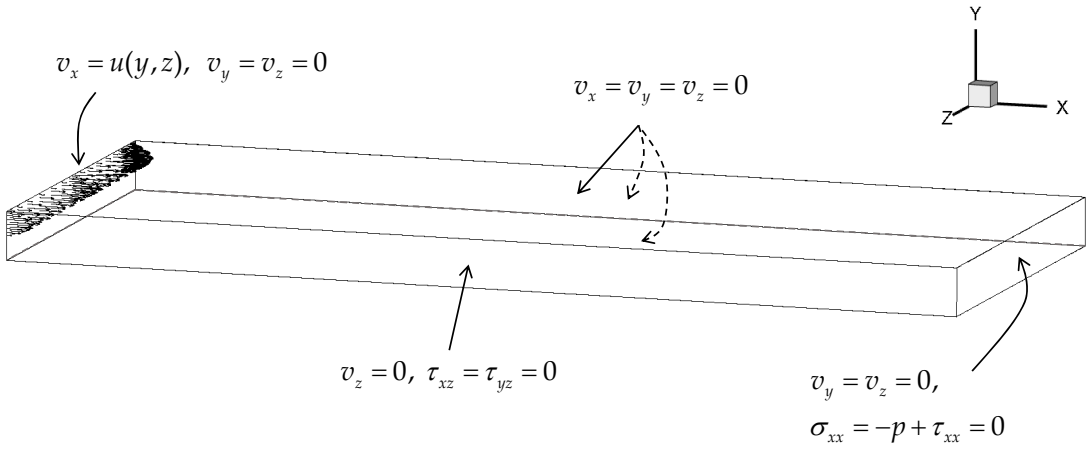

Figure 5.46: Boundary conditions for the problem of 3-D backward-facing step flow.

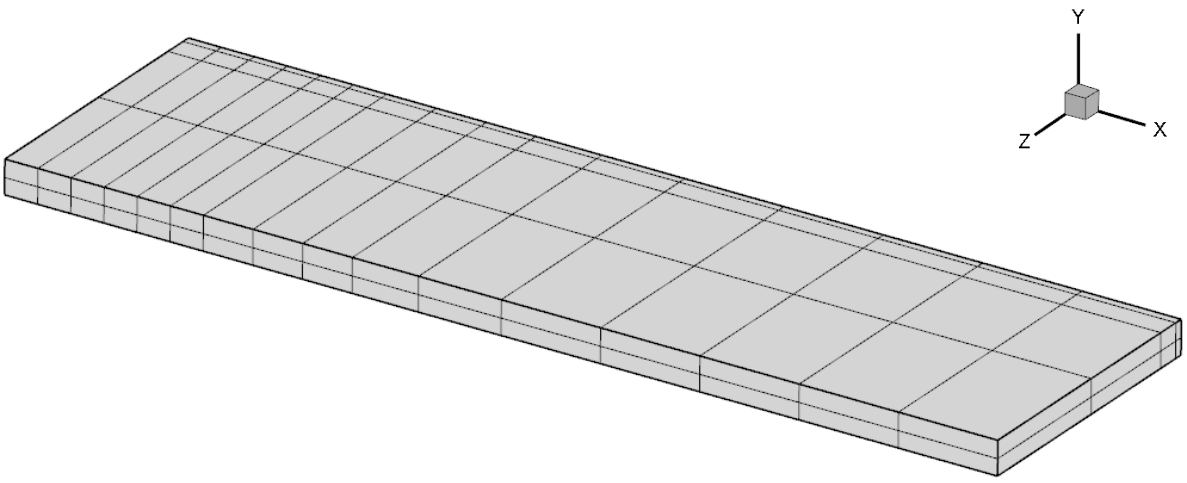

Figure 5.47: Mesh for the problem of 3-D backward-facing step flow.

5.5.2 Verification and validation tests

In order to verify and validate the present code, the results for Newtonian fluids are compared with the numerical results of Gartling [95] first and then with the experimental results of Armaly et al. [96]. Comparing with the work of Gartling [95] who employed a weak-form Galerkin finite element model involving velocities and pressure as variables, we showed the dependency of numerical solutions on the polynomial order, p. Figures 5.48–5.51 present the comparison of the horizontal and vertical velocity curves (v_x and v_y) for Re = 800 at $x = 7$ and $x = 15$ with various p-levels. We can observe that the velocity profiles of the present study are independent of the polynomial order when p is greater than 10, and the converged velocity profiles of p = 11 and 12 demonstrate good agreement with the results of Gartling [95]. For both v_x and v_y, the numerical results at $x = 7$ are more sensitive to p-level than the results at $x = 15$ where the flow is almost fully developed.

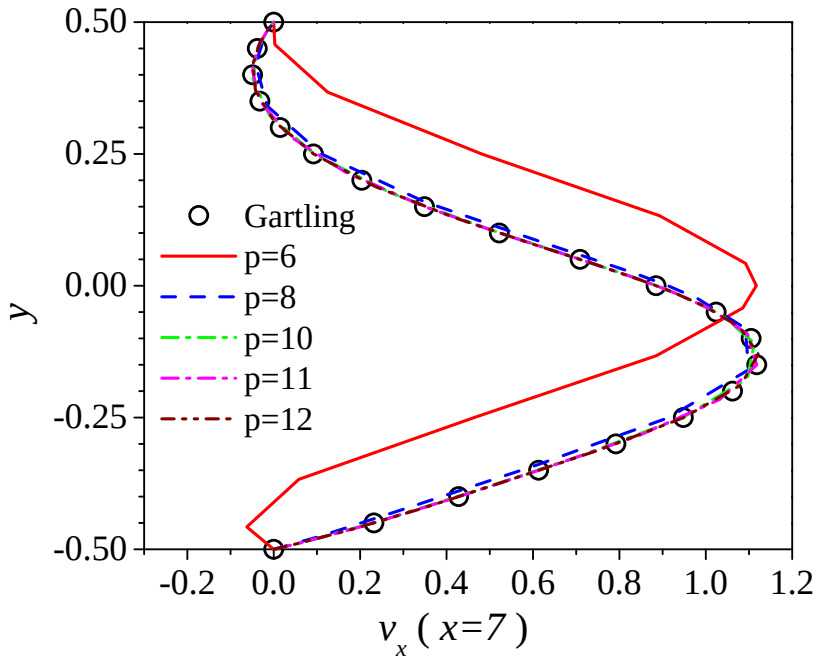

Figure 5.48: Dependency of horizontal velocity at $x = 7$ on p-level (Re=800).

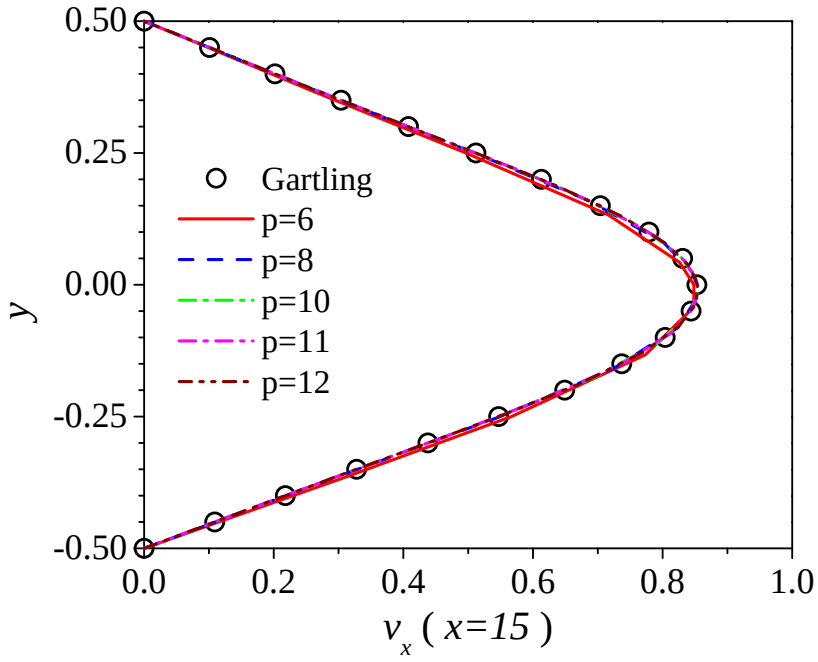

Figure 5.49: Dependency of horizontal velocity at $x = 15$ on on p-level (Re=800).

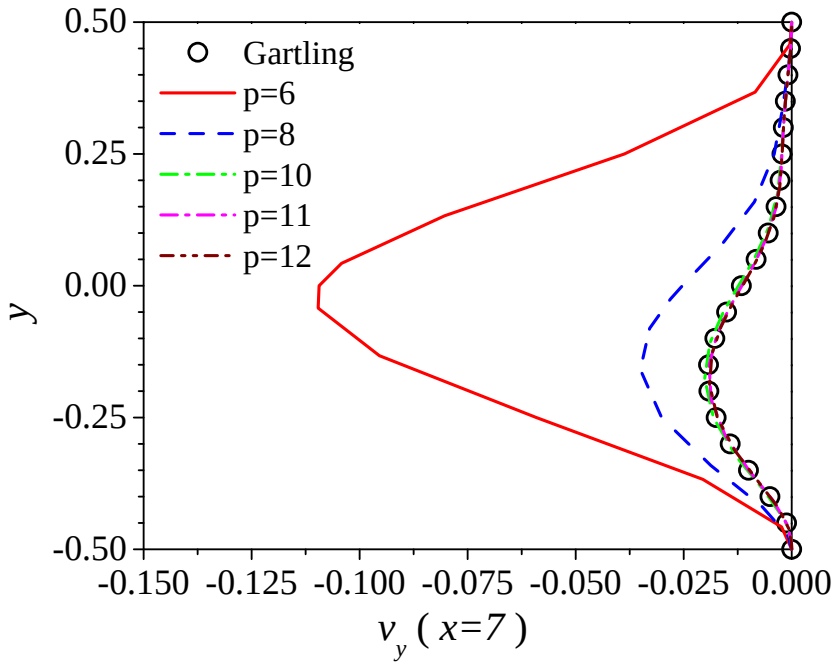

Figure 5.50: Dependency of vertical velocity at $x = 7$ on p-level (Re=800).

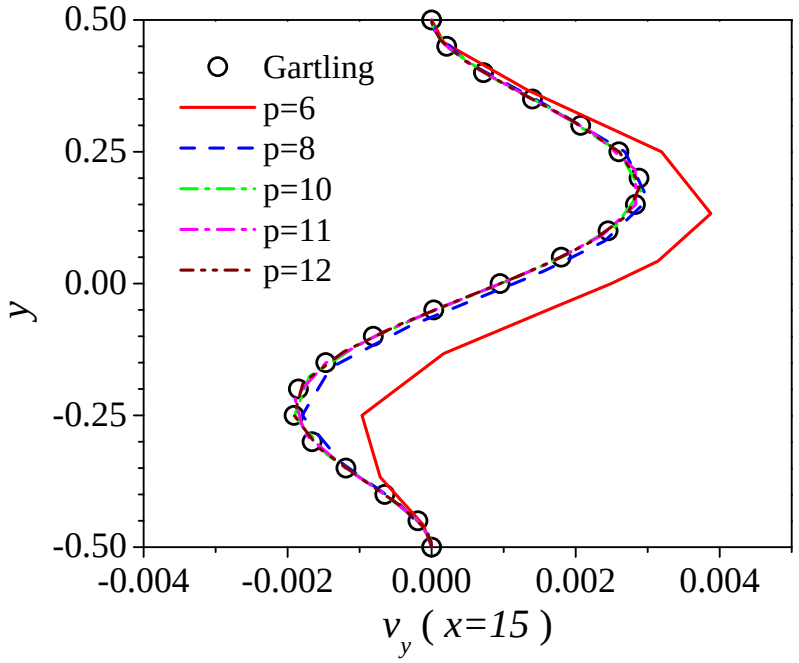

Figure 5.51: Dependency of vertical velocity at $x = 15$ on p-level (Re=800).

To compare with the experimental work of Armaly et al. [96], we set $S = 0.49$ and $h = 0.52$. Figure 5.52 shows the comparison for the horizontal velocity profiles v_x at several axial positions downstream of the step for Re = 100; x/S denotes the dimensionless axial position downstream of the step. In order to obtain solutions near the axial positions given in Armaly et al. [96], we used a more refined mesh, namely, 80×8 mesh of rectangular elements with polynomial order of 8. For the 80×8 mesh, the results show independence of p-level when p is larger than 5. Difference between each axial position of [96] and that of the present study are less than 1%. The numerical solutions demonstrate good agreement with the experimental data.

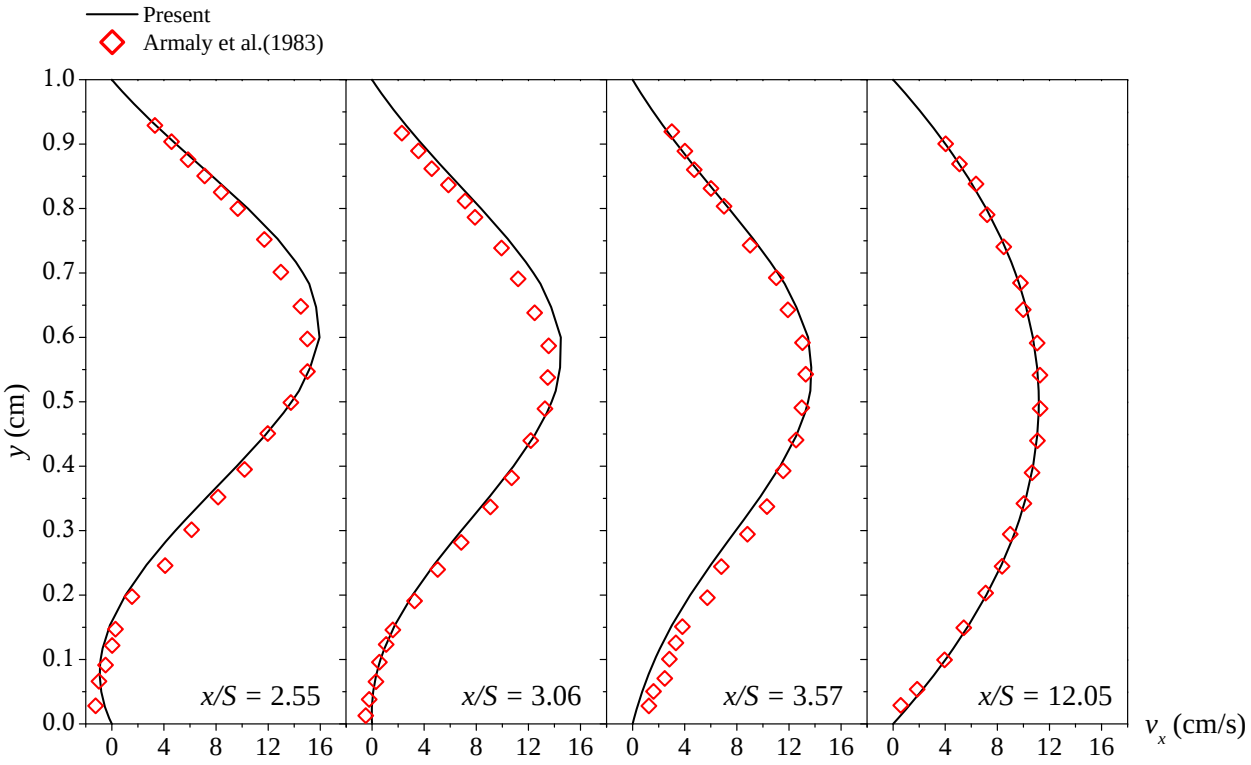

Figure 5.52: Horizontal velocity v_x at several axial positions x/S downstream of the step for Re = 100.

We also tested for reattachment lengths (or, length of the recirculation zone) at the lower wall which is caused by the existence of a backward-facing step and compared them with the data

of [96]. The recirculation zone and reattachment length at lower wall are also called primary recirculation zone (or, separation zone) and primary reattachment length, respectively, because it is the main recirculation zone. The streamlines of backward-facing step flow (Re = 800) for the part of the domain are shown in Figure 5.53, where the reattachment length denoted by x_R is depicted. A reattachment point is assumed to be the point of zero wall shear stress which is located by interpolating between the shear stress values at the lower wall [95]. Armaly et al. [96] investigated that the flow downstream (near the step) was three-dimensional when Re > 400. Hence, both 2-D and 3-D flows were solved to see the effect of three-dimensionality of flow on x_R. We performed convergence test of increasing p-level for x_R using 2-D simulations. The 2-D fluid domain is discretized into a non-uniform 16×2 mesh of rectangular elements, such that it corresponds to 3-D fluid domain which is discretized into a non-uniform $16 \times 2 \times 4$ mesh of rectangular elements. It was found that the results of 16×2 mesh and those of 20×2 mesh which is used for previous tests are similar. Table 5.1 shows that x_R/S for Re = 800 approaches p-independence when p is greater than 9. Due to the memory restriction of the cluster where the code was executed, we used p$= 8$ for 3-D simulation. However, considering that x_R/S of p$= 8$ has small difference (2.2%) from the converged value of x_R/S, solutions of p$= 8$ is not far from the converged solutions.

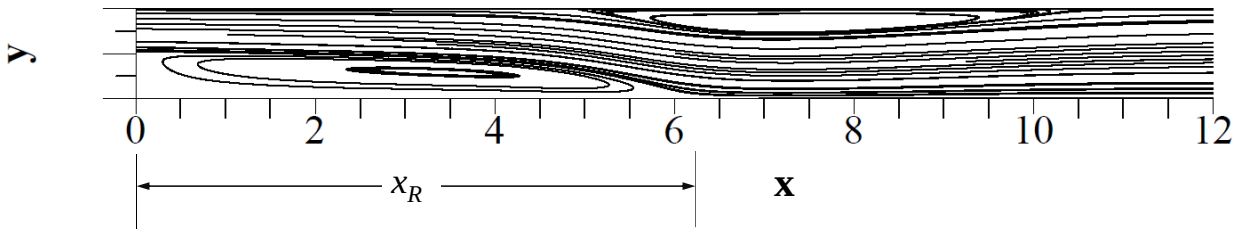

Figure 5.53: Streamlines of backward-facing step flow at Re = 800 (x_R denotes a reattachment length).

x_R/S				
p=7	p=8	p=9	p=10	p=11
13.6	12.9	12.7	12.6	12.6

Table 5.1: Dimensionless reattachment length (x_R/S) for Re = 800 with various polynomial order (p).

In Figures 5.54–5.55, we plot the dimensionless reattachment length, x_R/S, with respect to the Reynolds number for 2-D and 3-D simulations. When comparing between the fit curves of the experimental data and numerical results, the 3-D simulation shows better agreement. The difference between the present results and the experimental results is less than 10% for the 3-D simulation, while the difference for the 2-D simulation is greater than 10% when Re < 140 and Re > 790 and less than 10% in other range of Re. Considering that the reattachment length approaches smaller value as p increases (see Table 5.1), the difference between the experiment data and the 3-D numerical results would be smaller if p greater than 8 is used. The 3-D result becomes different from the 2-D result when Re > 300 and the discrepancy becomes larger as Re increases. In other words, the side wall ($z = 0$) affect the flow structure when Re is above 300 and this side-wall effect increases with Re. Figure 5.56 shows the spiral particle paths from the side wall ($z = 0$) to the symmetry plane ($z = 8.575$). This swirling flow is known to be the reason for the variation of primary reattachment length in z-direction [91, 97]. A wall jet in x-direction at the side wall interacts with recirculation zones at the upper and lower parts of the side wall, which leads to 3-D vortices near the side wall. These vortices move across the main flow stream with spiral motion and join the recirculation zones at the symmetry plane, as mentioned in Williams and Baker's work [97]. Also, they addressed that the reason for longer reattachment length of the 3-D simulation than that of the 2-D simulation is due to the size of upper separation region. In the 2-D simulation, the upper separation region is thicker than in the 3-D simulation and this thicker blockage prevents the primary reattachment length to grow. The comparison between upper/lower

separation regions of the 2-D and 3-D results (see Figure 5.57) confirms this.

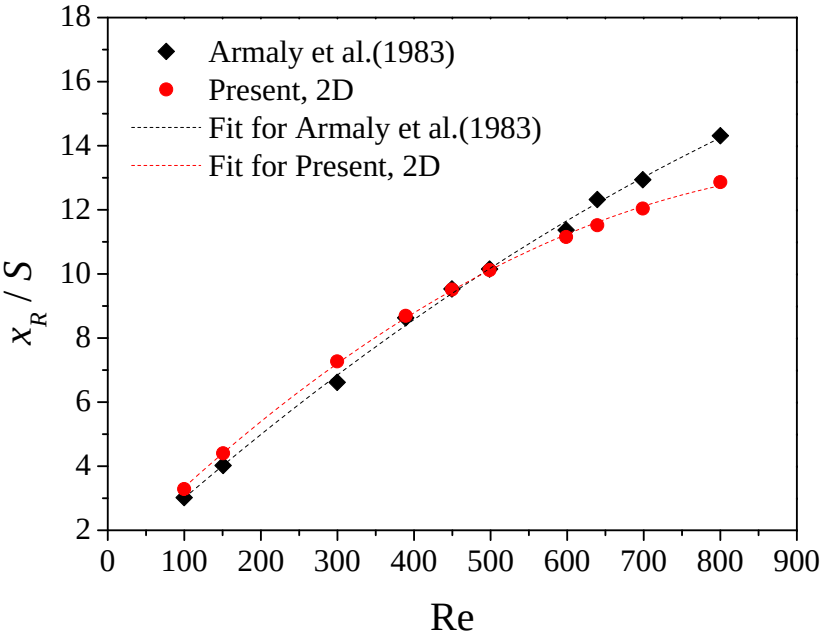

Figure 5.54: Reattachment length (2-D simulation) with respect to the Reynolds number.

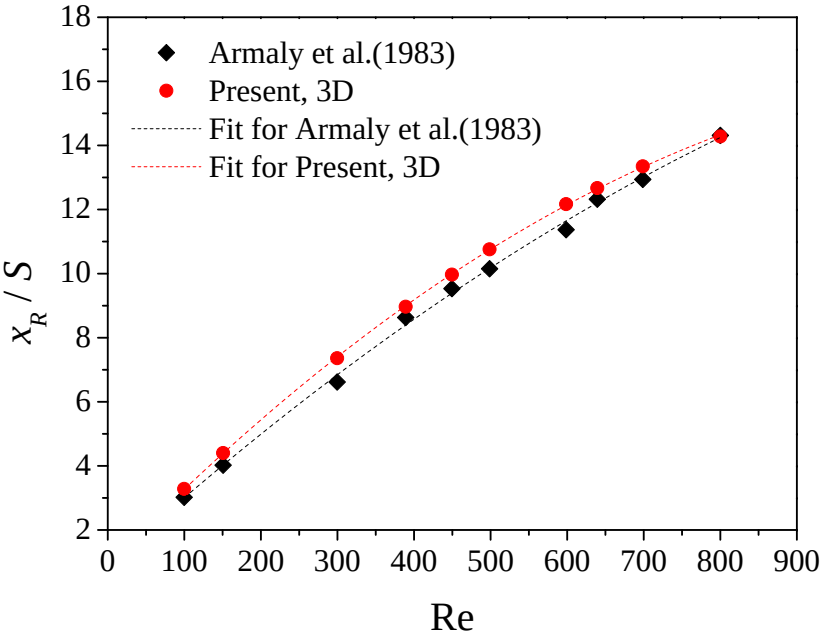

Figure 5.55: Reattachment length (3-D simulation) with respect to the Reynolds number.

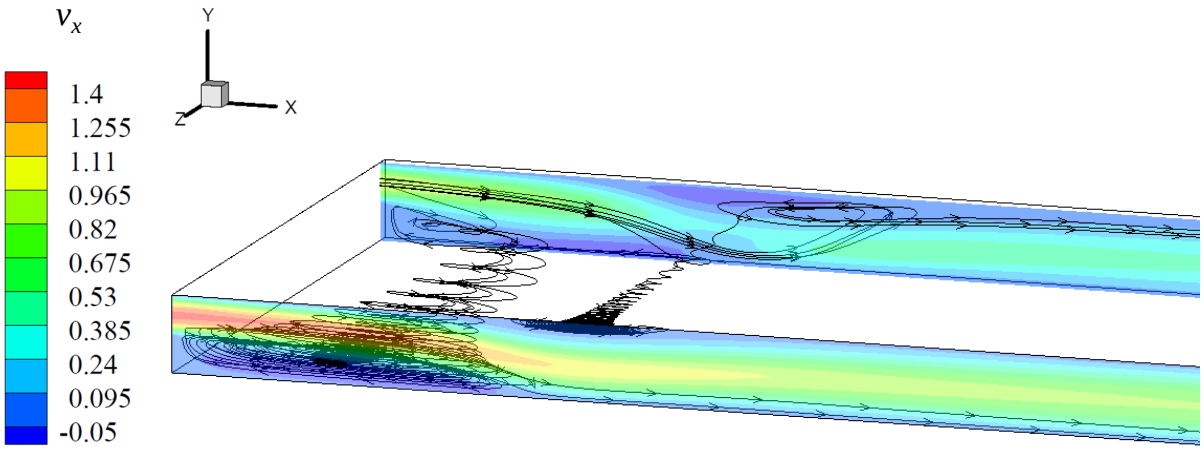

Figure 5.56: Spiral motion from the side wall to the symmetry plane (Re = 800).

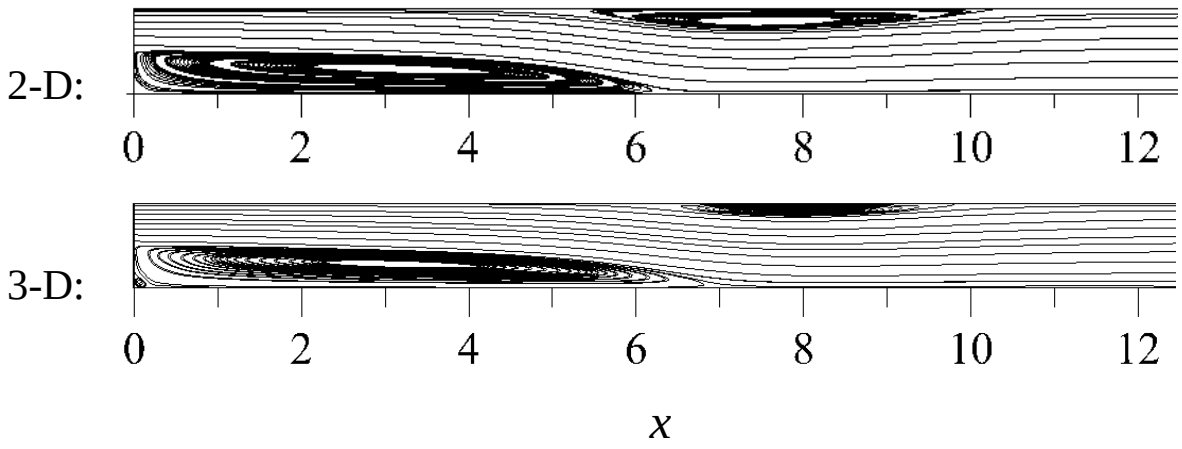

Figure 5.57: Comparison between 2-D and 3-D simulations for primary and secondary recirculation zones (Re = 800).

5.5.3 Parametric study of Carreau–Yasuda fluids

The effects of the three parameters (a, n, λ_{CY}) of the Carreau–Yasuda model, Eq. (2.5), on the flow over a backward-facing step were studied. Since the flow behavior on the symmetry plane of 3-D backward-facing step problem is similar with that of the 2-D problem, we performed 2-D analysis for parametric study. 20×2 mesh of Figure 5.44 and polynomial order of 12 were used for

parametric study. We focused on how the reattachment length x_R is affected by these parameters. Here, the limiting viscosities in Eq. (2.5) are set as $\mu_0 = 100\mu_\infty$ and the Reynolds number (Re) is 100. In Figures 5.58, 5.61, and 5.64, the relation of a, n, λ_{CY} and the dimensionless reattachment length x_R/S are shown, respectively, and Figures 5.59, 5.62, and 5.65 present the viscosity curves with respect to shear rate in the fluid domain for various values of a, n and λ_{CY}, respectively. Figures 5.60, 5.63, and 5.66 present effect of a, n, λ_{CY} on the horizontal velocity (v_x) contour. From Figure 5.58, we see that when the parameter a increases with other parameters fixed ($n = 0.5$, $\lambda_{CY} = 1.0$), the reattachment length x_R reduces. Also, the rate of change of x_R diminishes from $a = 0.2$ to $a = 2.0$ and is close to zero rate for $2.0 \leq a \leq 10.0$. The reason of this relation can be explained by Figure 5.59, where decrease in a makes the viscosity lower with changing the curve shape. Since the fluid with less viscosity has larger recirculation zone downstream the step, the reattachment length becomes longer with decreasing a. Also, in Figure 5.59, the rate of change in the shape of the viscosity curves decreases as a increases. This causes the rate of change in reattachment length to reduce as a grows for $0.2 \leq a \leq 10.0$. From the horizontal velocity contours (see Figure 5.60), we can also see the variation of reattachment length with resect to a. Blue part indicates region with backflow (having negative value of v_x) and the length of this region is similar to x_R. The fluid with smaller a has longer backflow zone (that is, longer x_R), and especially when $a = 0.2$, backflow zone appears at both top and bottom walls. Figure 5.61 shows that the reattachment length is shortened with increasing power index n for $0.25 \leq n \leq 1$ while the other parameters are constant ($a = 2.0$, $\lambda_{CY} = 1.0$). Since decrease in n makes the viscosity less with changing the curve slope in the power-law region (see Figure 5.62; for power-law region, see Figure 2.1), fluid with smaller n has longer reattachment length downstream the step. The horizontal velocity contours in Figure 5.63 also tells that the reattachment length becomes smaller as n decreases. In Figure 5.64, the reattachment length grows with the Carreau number λ_{CY} for $0.01 \leq \lambda_{CY} \leq 1.0$ ($a = 2.0$, $n = 0.5$). Increase in λ_{CY} causes the viscosity to reduce with shifting the transition region (transition from the zero-shear-rate plateau to power-law region; see Figure 2.1) of the curve as in Figure 5.65, which means that fluid with greater λ_{CY} has larger

recirculation zone. In the horizontal velocity contours (Figure 5.66), the fluid with larger λ_{CY} has longer backflow region (or longer x_R).

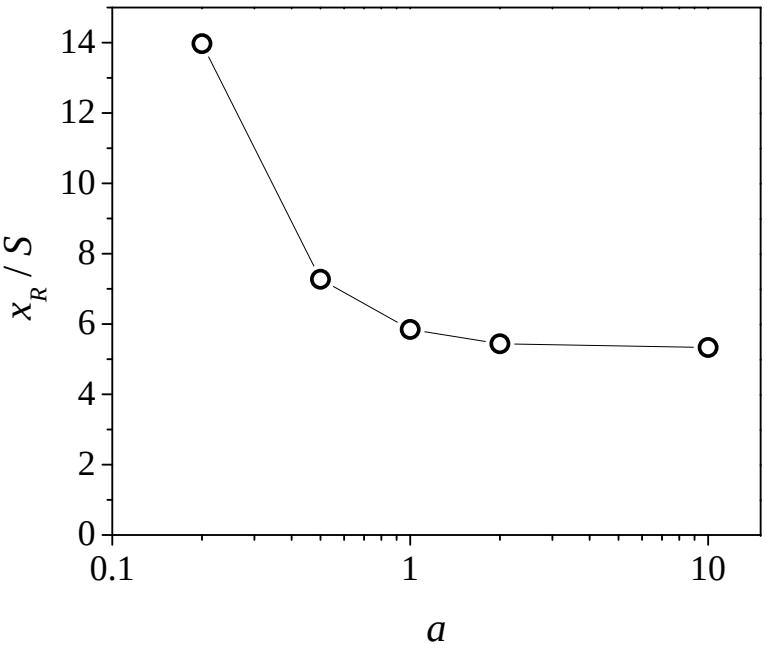

Figure 5.58: Effect of the parameter a on reattachment length x_R ($n = 0.5$, $\lambda_{CY} = 1.0$).

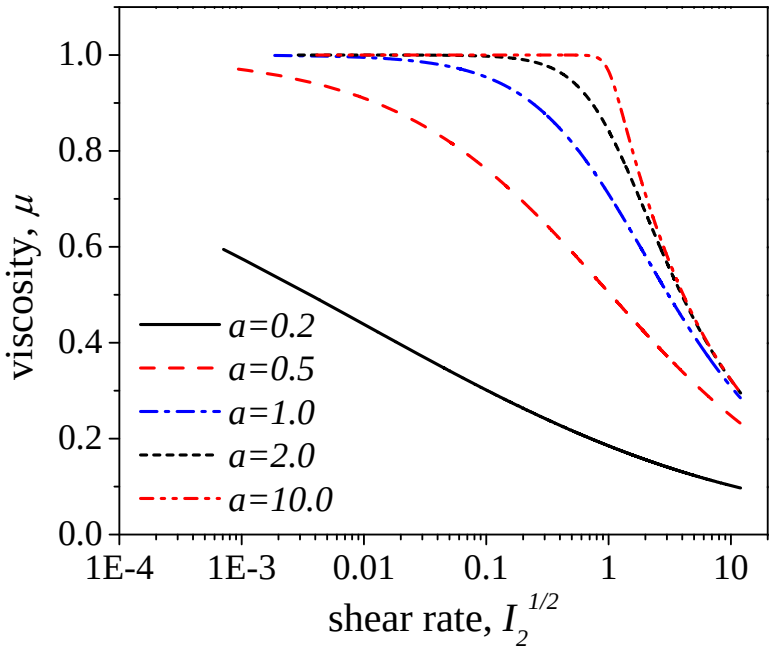

Figure 5.59: Effect of the parameter a on viscosity ($n = 0.5$, $\lambda_{CY} = 1.0$).

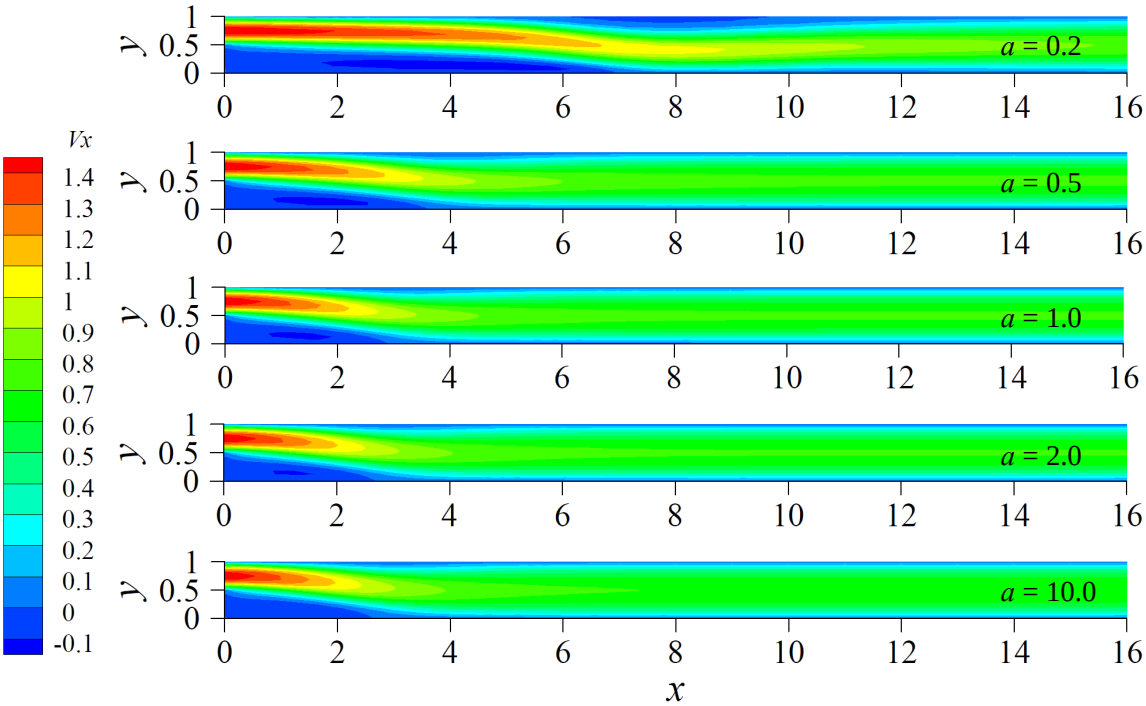

Figure 5.60: Effect of the parameter a on v_x-contour ($n = 0.5$, $\lambda_{CY} = 1.0$).

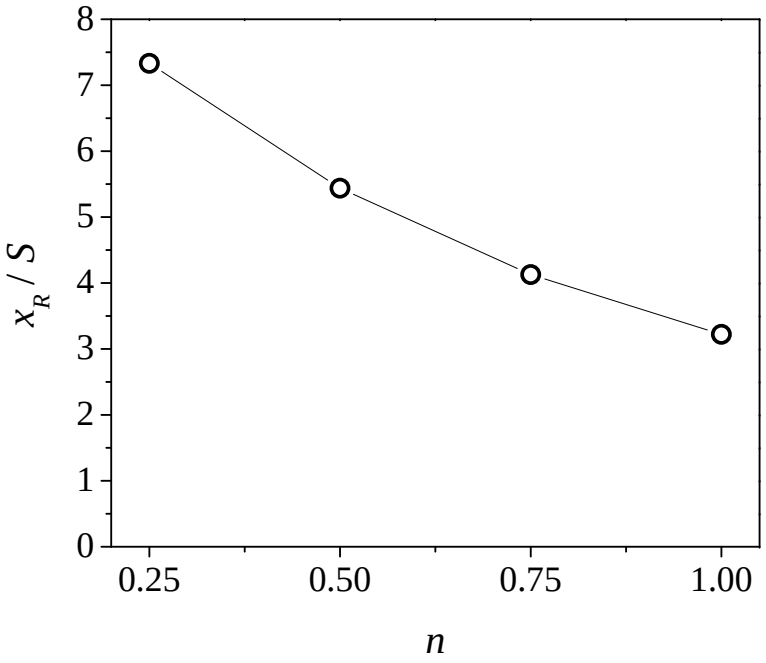

Figure 5.61: Effect of the parameter n on reattachment length x_R ($a = 2.0$, $\lambda_{CY} = 1.0$).

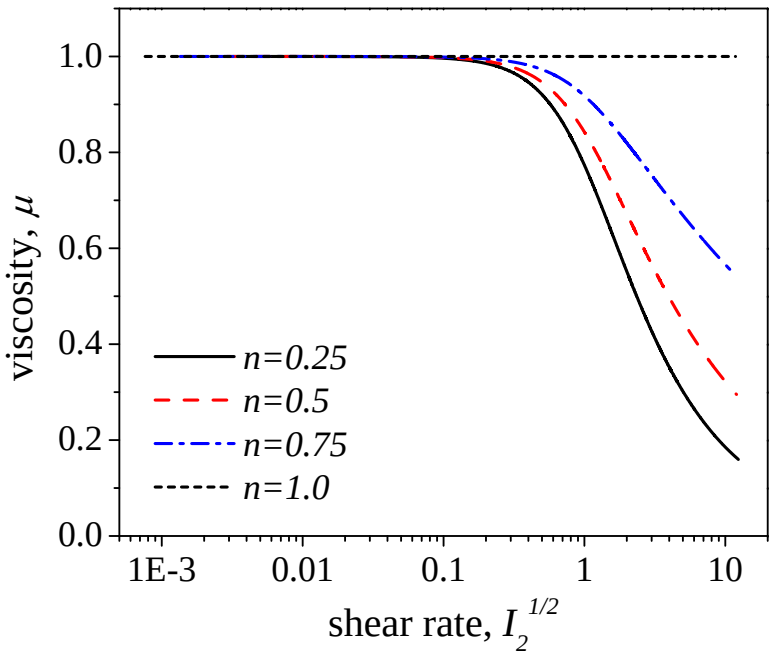

Figure 5.62: Effect of the parameter n on viscosity ($a = 2.0$, $\lambda_{CY} = 1.0$).

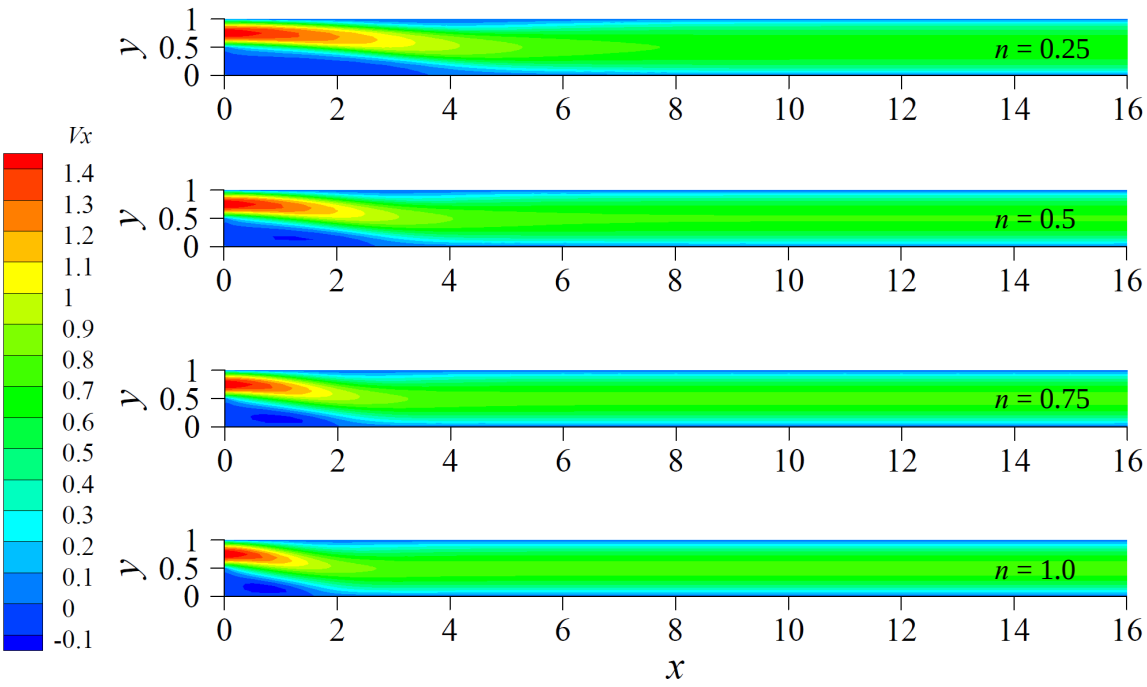

Figure 5.63: Effect of the parameter n on v_x-contour ($a = 2.0$, $\lambda_{CY} = 1.0$).

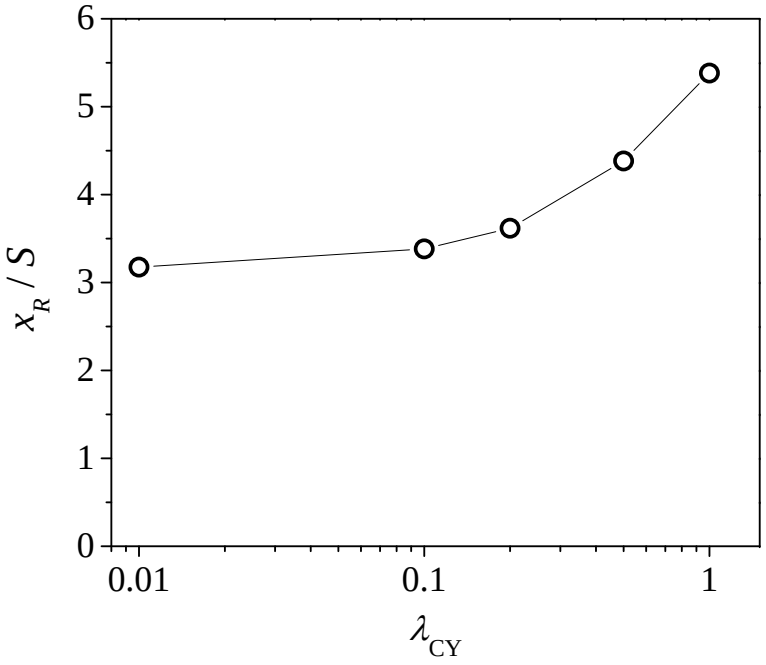

Figure 5.64: Effect of the Carreau number λ_{CY} on reattachment length x_R ($a = 2.0$, $n = 0.5$).

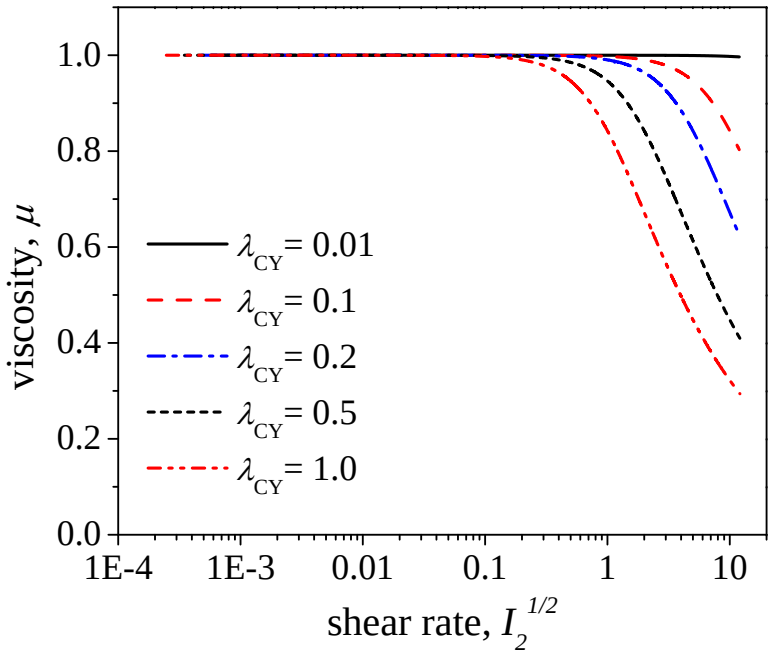

Figure 5.65: Effect of the Carreau number λ_{CY} on viscosity ($a = 2.0$, $n = 0.5$).

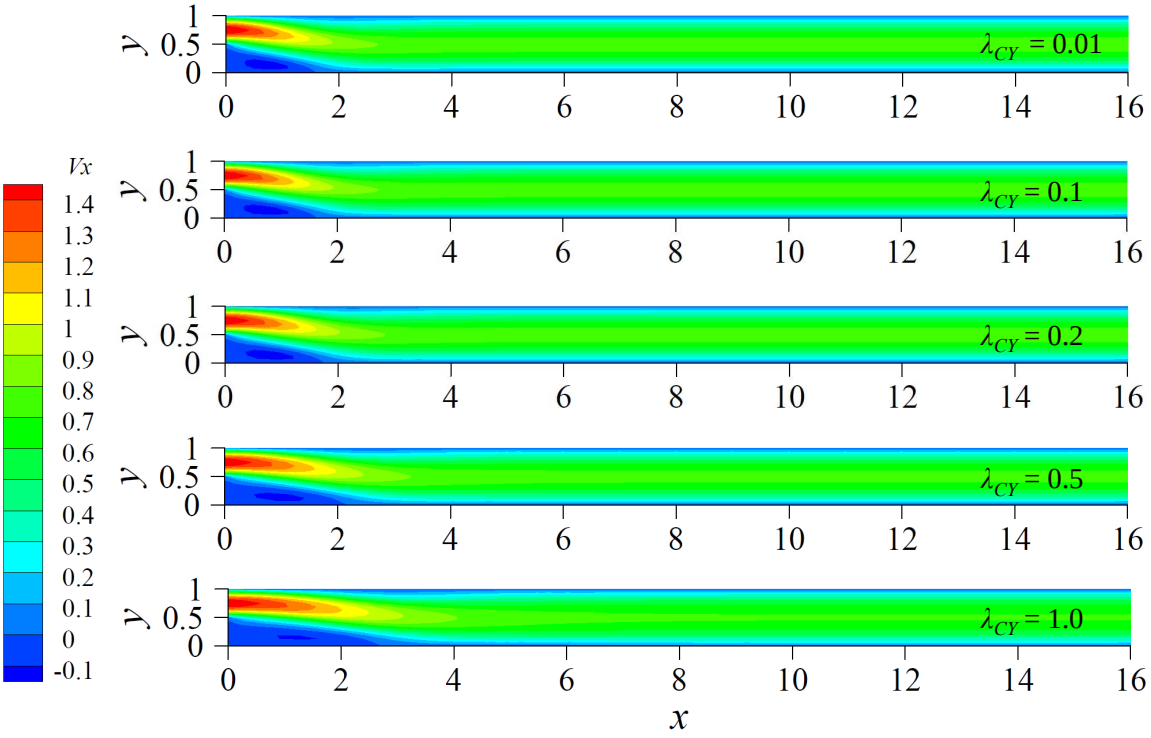

Figure 5.66: Effect of the parameter λ_{CY} on v_x-contour ($a = 2.0$, $n = 0.5$).

5.6 Flow past an unconfined circular cylinder

5.6.1 Problem description

The flow past a circular cylinder has been extensively studied experimentally and numerically. It is well-known that the pattern of laminar flow depends on the Reynolds number (Re) [98]. When Re is less than 40, the flow is steady. For Re < 5, no flow separation occurs. For $5 <$ Re < 40, the flow separates from the rear of the cylinder and a symmetric pair of standing vortices (steady separation bubble) appears. The length of the vortices is proportional to Re. When Re is further increased ($45 <$ Re < 150), the wake becomes unstable and vortices are shed periodically, one from the top and the other from the bottom of cylinder. This oscillating wake is known as *Kármán vortex street* which is transient. Here we consider steady flow where a steady separation bubble appears. The geometry of the computational domain and the boundary conditions for the problem are shown in Figure 5.67. The center of a circular cylinder of unit diameter is located at $(x, y) = (0, 0)$ in the rectangular region $[-15.5, 25.5] \times [-40.5, 40.5]$. The large computational domain is considered so that free-stream boundary conditions at the top and bottom of the domain can be applied without noticeably affecting the numerical solution. The free-stream boundary conditions ($v_x = v_\infty = 1.0$, $v_y = 0$) are applied to the inflow boundary ($x = -15.5$), top, and bottom of the domain. The traction-free boundary condition is imposed at the outflow in a weak sense through the least-squares functional. This traction-free boundary condition is different from what is used for the example of flow over a backward-facing step in Section 5.4, where the outflow condition is strongly imposed by taking $v_y = 0$ and $\sigma_{xx} = -p + \tau_{xx} = 0$. Due to the traction-free boundary condition applied through least-squares functional, the least-squares formulation is slightly different from what we describe in Section 3. One should add the following L_2-norm of residual to the original least-squares functional in Eq. (3.1).

$$\|\mathbf{R_4}\|^2_{\Gamma_t,0} = \hat{\mathbf{n}} \cdot \{-p\underline{\mathbf{I}} + \mu(I_2)\boldsymbol{\nabla}\mathbf{v}\} - \tilde{\mathbf{t}}^{\mathrm{s}}, \tag{5.14}$$

where $\tilde{\mathbf{t}}^{\mathrm{s}}$ denotes the specified pseudo-traction on the boundary Γ_t [99]. At the cylinder surface, the velocity components are set to zero due to the no-slip condition. The domain is discretized into 788 non-uniform finite elements as in Fig. 5.67. The close-up view around the cylinder is shown in Fig. 5.68, for example, when the polynomial order (p) is 3. $\mathrm{p} = 7$ is used in this study and the reason of choosing it will be explained in the following section. The mesh near the cylinder is more refined than other parts to ensure adequate resolution of the vortices at rear side of the cylinder. Nonlinear convergence is declared when the Euclidean norm of the difference between two consecutive iteration solutions is less than 10^{-3}. In this problem, the characteristic velocity and length for the Reynolds number and Carreau number of Eq. (2.8) are the free-stream velocity ($v_0 = v_\infty = 1.0$) and diameter of the cylinder ($L_0 = D = 1.0$), respectively.

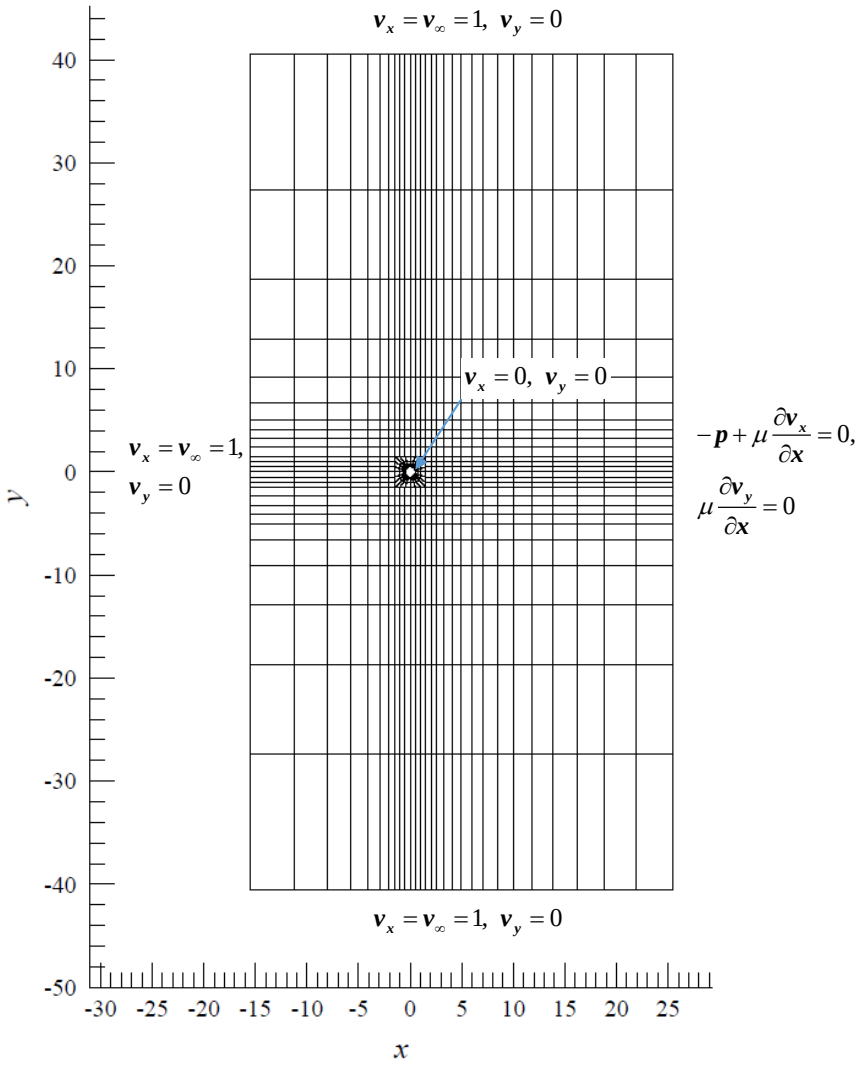

Figure 5.67: Computational domain and mesh for the problem.

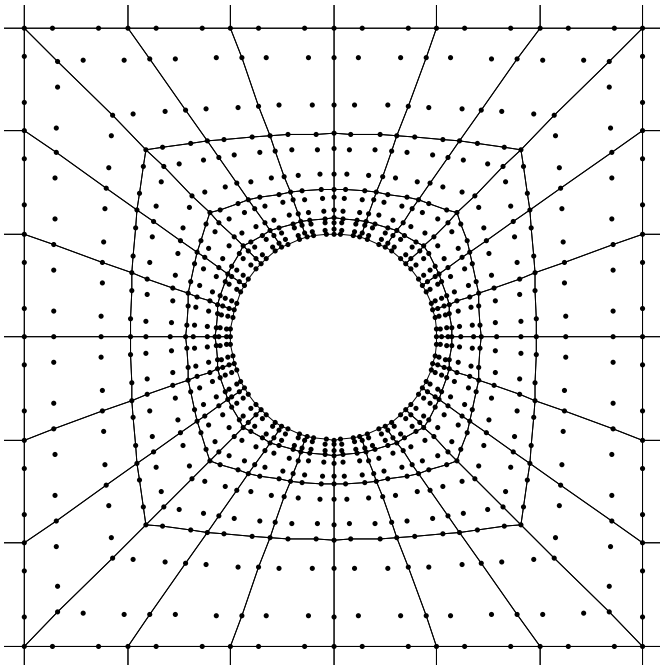

Figure 5.68: Close-up view of the mesh around the cylinder.

5.6.2 Verification test

To verify the present model, we first compared our results with the previous numerical study of Lashgari et al. [100] who used a second-order finite difference method to analyze the flows of Carreau–Yasuda fluids. When comparing with their work, we demonstrate the dependency of our numerical solutions (drag coefficient) on the polynomial order, p. The pressure and drag forces acting on the cylinder are given by

$$\mathbf{F}_p = \oint p\hat{\mathbf{n}}\, ds, \quad \mathbf{F}_v = -\oint \boldsymbol{\tau}\cdot\hat{\mathbf{n}}\, ds = -\oint \mu\left(\boldsymbol{\nabla}\mathbf{v} + \boldsymbol{\nabla}\mathbf{v}^{\mathrm{T}}\right)\cdot\hat{\mathbf{n}}\, ds. \tag{5.15}$$

For this problem, the corresponding force coefficients are the x-components of the pressure force and viscous force, each normalized by the dynamic pressure, $\frac{1}{2}\rho_0 v_\infty^2$.

$$C_{Dp} = \frac{F_{p,x}}{\frac{1}{2}\rho_0 v_\infty^2 D}, \quad C_{Dv} = \frac{F_{v,x}}{\frac{1}{2}\rho_0 v_\infty^2 D}, \tag{5.16}$$

where C_{Dp} is called pressure drag coefficient and C_{Dv} is called viscous drag coefficient. $F_{.,x}$ denotes the x-component of each force. The overall drag coefficient (or drag coefficient), C_D, is the sum of the two:

$$C_D = C_{Dp} + C_{Dv}. \tag{5.17}$$

Table 5.2 show the drag coefficient (C_D) of the cylinder for different polynomial orders, where Re $= 10$ and Carreau–Yasuda parameters of Eq. (2.5) are given by $n = 0.4$, $a = 2.0$, $\lambda_{CY} = 10$, and $\mu_0 = 1000\mu_\infty$. It shows that C_D approaches p-independence when p is greater than 5, and the converged C_D value of the present study is in good agreement with the result of Lashgari et al. [100] whose C_D is 1.24. Based on this, we choose the polynomial order of 7 when comparing with other existing works in the literature and conducting a parameter study of Carreau–Yasuda fluids.

C_D			
p=5	p=6	p=7	p=8
1.238	1.236	1.236	1.236

Table 5.2: Drag coefficient (C_D) with various polynomial order (p).

In Fig. 5.69, we plotted the pressure coefficient along the cylinder surface with the experimental results of Grove, Shair, and Petersen [101] for Newtonian fluids ($n = 1.0$) with Re $= 40$. The pressure coefficient is the dimensionless pressure difference defined as:

$$C_p = \frac{p - p_0}{\frac{1}{2}\rho_0 v_\infty^2}, \tag{5.18}$$

where p_0 is the reference pressure which is set to zero. The angle θ starts from the front stagnation point of the cylinder as depicted in Fig. 5.69. The numerical result is in good agreement with their experimental result. Figure 5.70 shows the pressure contours and streamlines around the cylinder for Newtonian fluids and Re $= 40$. The wake length L is equal to 4.56 cylinder radii, which

shows good agreement with the numerical results of Kawaguti and Jain [102] whose wake length is 4.5 cylinder radii. In the verification and validation tests, the L_2 least-squares functionals are 1.89×10^{-6} for Carreau–Yasuda fluid and 3.01×10^{-7} for Newtonian fluid.

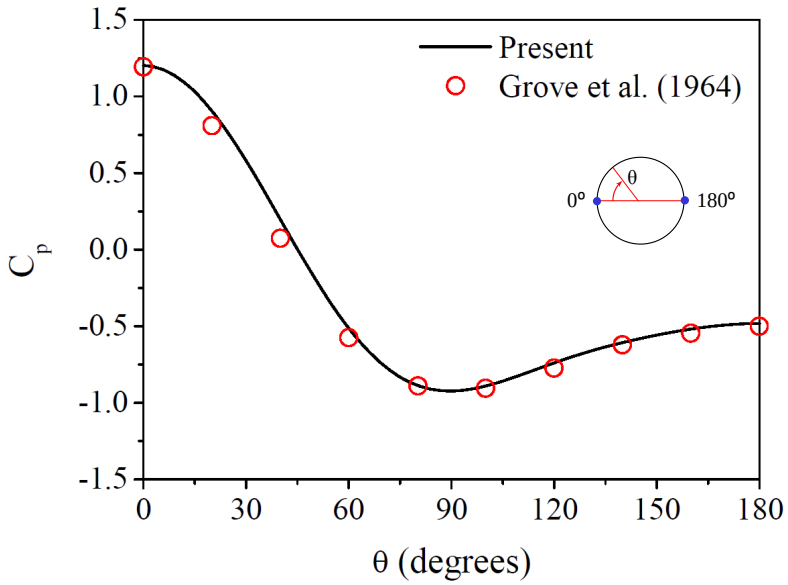

Figure 5.69: Pressure coefficient along the cylinder surface.

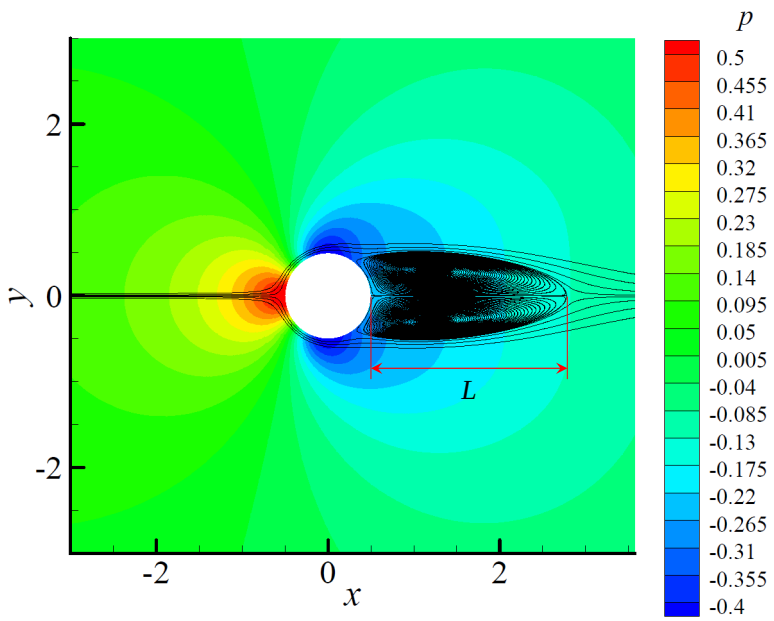

Figure 5.70: Pressure contour and streamlines around the cylinder.

5.6.3 Parametric study of Carreau–Yasuda fluids

The effects of the three parameters (a, n, λ_{CY}) of the Carreau–Yasuda model, Eq. (2.5), on the flow past a circular cylinder are analyzed. We focused on how the pressure coefficient, wake length, and pressure/viscous drag coefficients are affected by these parameters. The limiting viscosities in Eq. (2.5) are set as $\mu_0 = 100\mu_\infty$.

First, we test for the shape parameter a. In Figure 5.71, the viscosity curves for various values of a are plotted with respect to shear rate. As a increases, the viscosity becomes higher with changing the curve shape. Figure 5.72 shows the pressure coefficient, C_p, along the cylinder surface for the same a values. C_p at the front stagnation point ($\theta = 0°$) increases with a and the region of positive pressure gradient starts at larger θ as a is increased. For example, when $a = 0.1$, the positive pressure gradient begins around $\theta = 90°$, while it begins around $\theta = 105°$ for $a = 0.3$. When the positive pressure gradient is strong enough, the flow separates and a wake is formed. Comparing Figure 5.73 and Figure 5.74, we can see that the start point of positive pressure gradient affects the size of wake. The wake length with respect to a is shown in Figure 5.75, where

the wake length reduces as a increases. As a result, Figures 5.71–5.75 demonstrate that the fluid with higher viscosity gives higher pressure at the front stagnation point on the cylinder and makes the flow separate at more rear side of the cylinder which leads to the smaller wake region. We also plot the drag coefficient (Eq. (5.17)) with respect to a in Figure 5.76, where overall drag coefficient (C_D) is the sum of pressure drag coefficient (C_{Dp}) and viscous drag coefficient (C_{Dv}). C_{Dp} increases with a, since the fluid with larger a gives higher pressure along the cylinder surface as can be seen in Figure 5.72. C_{Dv} also increases with a, because the fluid with larger a has higher viscosity (Figure 5.71) and thus exerts more viscous force on the cylinder. In Figure 5.76, C_{Dp} has larger portion than C_{Dv}. This is due to the shape of a circular cylinder. When overall drag mainly comes from pressure drag, as in the circular cylinder case, the body is described as *bluff*. When overall drag is dominated by viscous drag, the body is considered *streamlined* [63].

Secondly, the effect of the power index n is studied. Figure 5.77 shows the viscosity curves with respect to shear rate for various values of n. The viscosity increases with n with changing the curve slope in the power-law region. When $n = 1$, the fluid exhibits constant viscosity, that is, Newtonian fluid. We plot the pressure coefficients, C_p, along the cylinder surface for the same n values in Figure 5.78. C_p at the front stagnation point ($\theta = 0°$) grows larger as n increases and the positive pressure gradient begins at higher θ with increasing n. The wake length is plotted with respect to n in Figure 5.79, where the wake length becomes shorter as n is increased. When the fluid is Newtonian ($n = 1$), the wake length is 0 which means there is no flow separation. Therefore, Figures 5.77–5.79 lead to the same explanation with the test for a; the fluid with higher viscosity exerts higher pressure at the front stagnation point on the cylinder and causes the flow to separate at more rear side of the cylinder which makes the wake smaller. Figure 5.80 presents the coefficients of overall drag (C_D), pressure drag (C_{Dp}) and viscous drag (C_{Dv}) with respect to n. C_{Dp} grows as n increases, since the fluid with larger n exerts more pressure along the cylinder surface as can be seen in Figure 5.78. C_{Dv} increases with n, because the fluid with larger n has higher viscosity (Figure 5.77) and thus gives larger viscous force on the cylinder. Consequently, the overall drag, $C_D\,(= C_{Dp} + C_{Dv})$, increases with n.

Finally, we test the effect of the dimensionless time constant λ_{CY}. The viscosity curves with respect to shear rate for various values of λ_{CY} are shown in Figure 5.81. The viscosity increases as λ_{CY} decreases with shifting the transition region (transition from the power-law region to the infinite-shear-rate plateau) of the curve. Figure 5.82 presents the pressure coefficients, C_p, along the cylinder surface for the same λ_{CY} values. C_p at the front stagnation point ($\theta = 0^\circ$) becomes higher as λ_{CY} decreases and the positive pressure gradient starts at higher θ with decreasing λ_{CY}. The plot of the wake length with respect to λ_{CY} in Figure 5.83 demonstrates that the wake length grows longer as λ_{CY} is increased. Likewise, Figures 5.81–5.83 tells us that the fluid with higher viscosity gives higher pressure at the front stagnation point on the cylinder and causes the flow separation at more rear side of the cylinder which leads to the smaller wake. In Figure 5.84, the coefficients of overall drag (C_D), pressure drag (C_{Dp}) and viscous drag (C_{Dv}) are shown for various λ_{CY}. C_{Dp} decreases as λ_{CY} decreases, because the fluid with larger λ_{CY} gives lower pressure along the cylinder surface as can be seen in Figure 5.82. C_{Dv} also becomes lower with increasing λ_{CY}, since the fluid with larger λ_{CY} has lower viscosity (Figure 5.81) and hence exerts smaller viscous force on the cylinder. Therefore, the overall drag coefficient decreases as λ_{CY} increases.

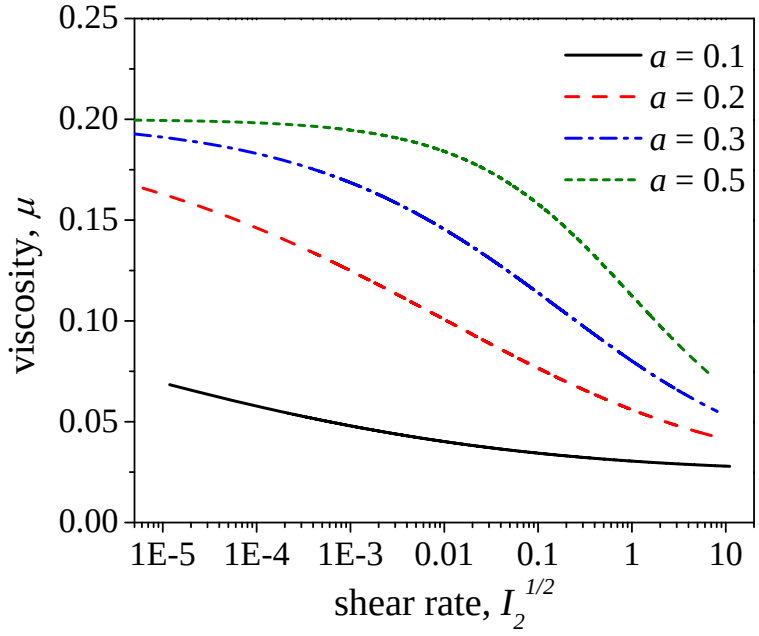

Figure 5.71: Viscosity curves for various a.

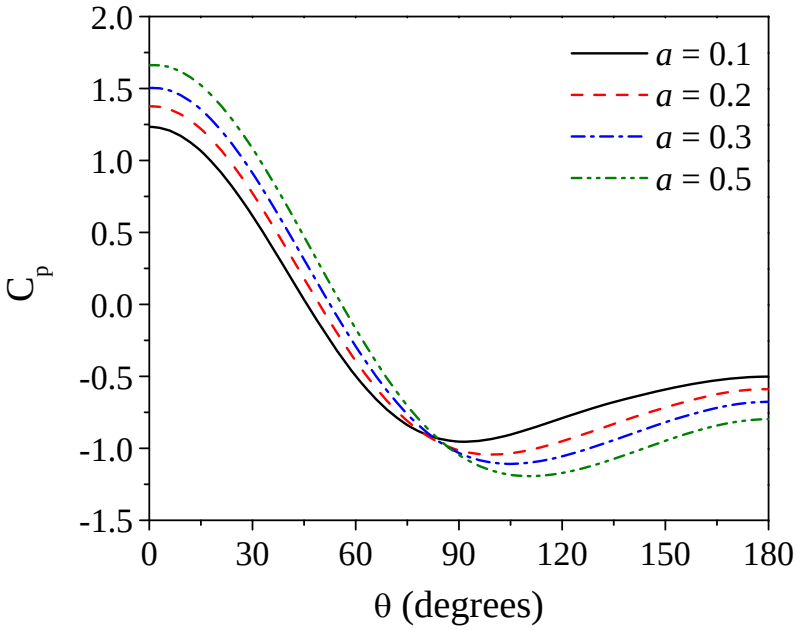

Figure 5.72: Effect of the parameter a on C_p.

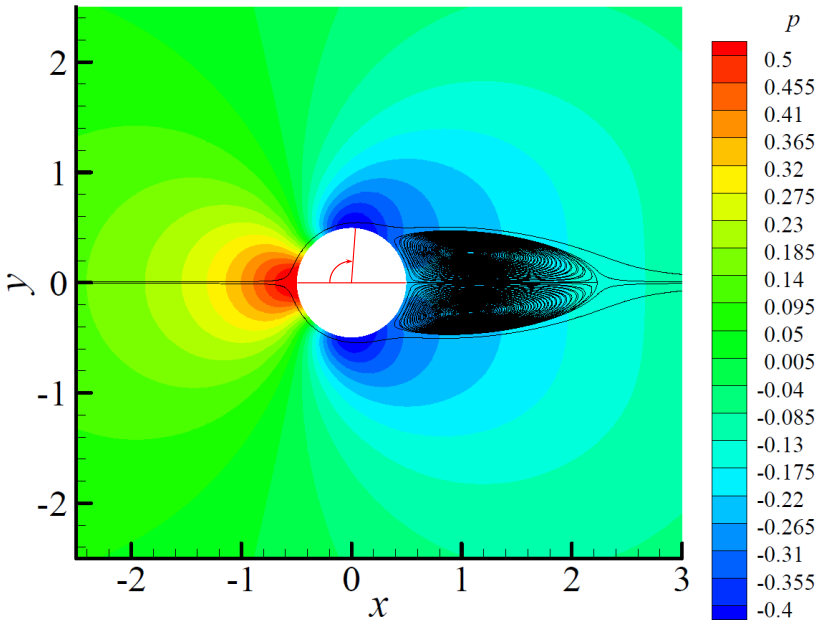

Figure 5.73: Pressure contour and streamlines around the cylinder when $a = 0.1$.

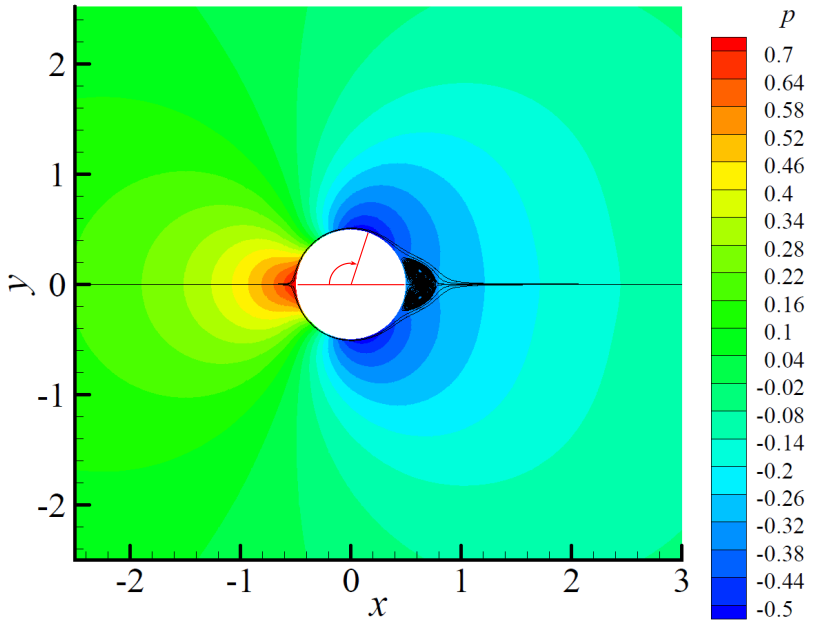

Figure 5.74: Pressure contour and streamlines around the cylinder when $a = 0.3$.

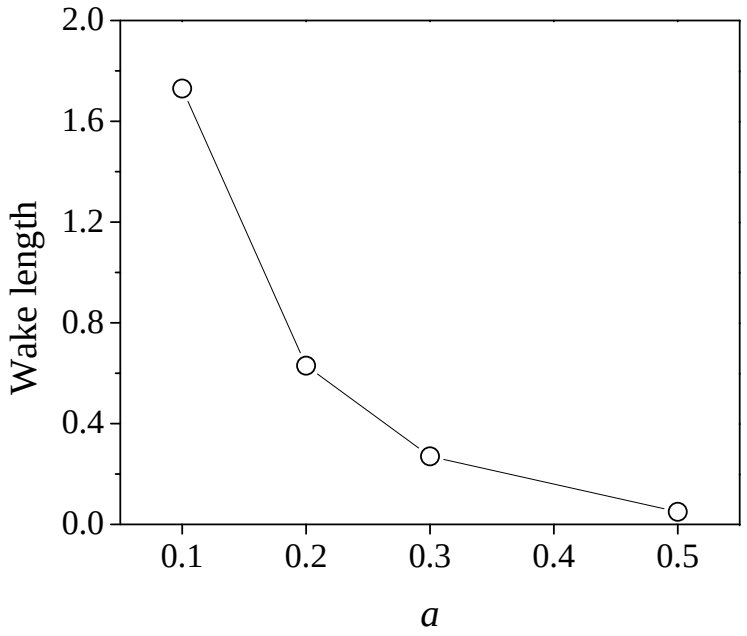

Figure 5.75: Effect of the parameter a on the wake length L.

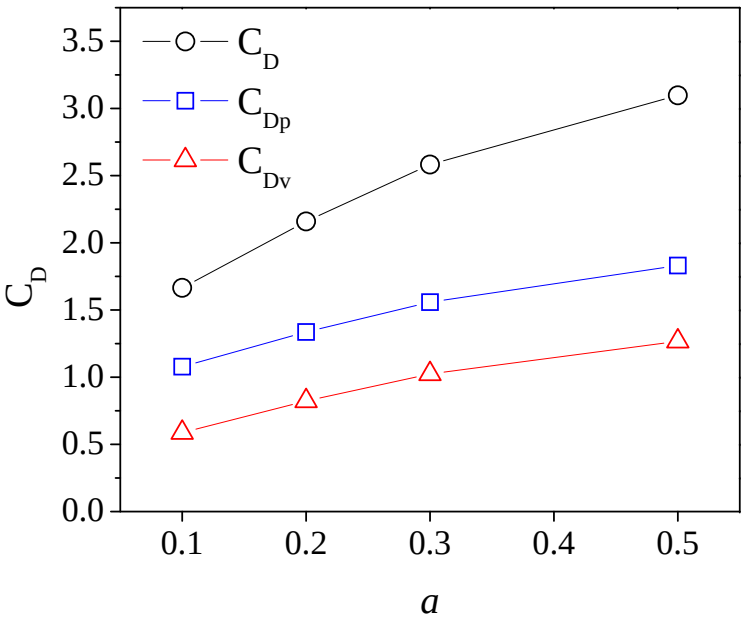

Figure 5.76: Effect of the parameter a on the drag coefficient.

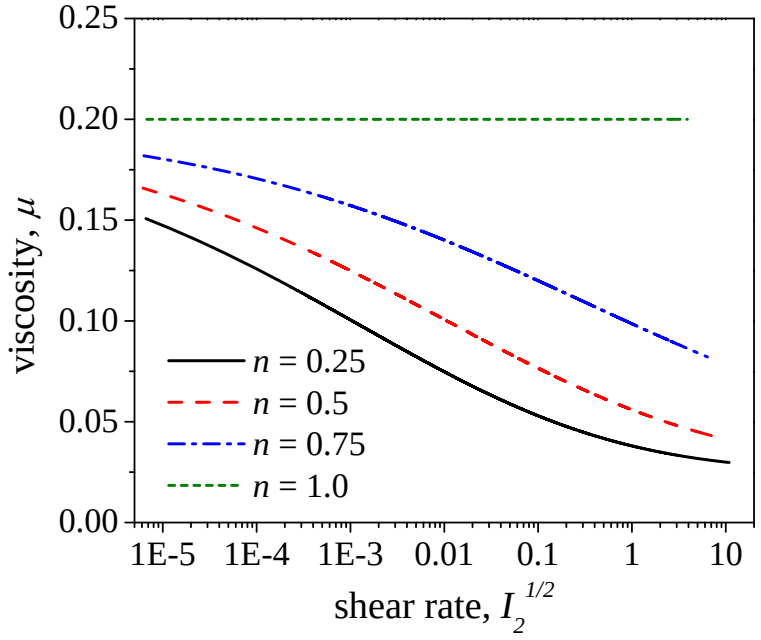

Figure 5.77: Viscosity curves for various n.

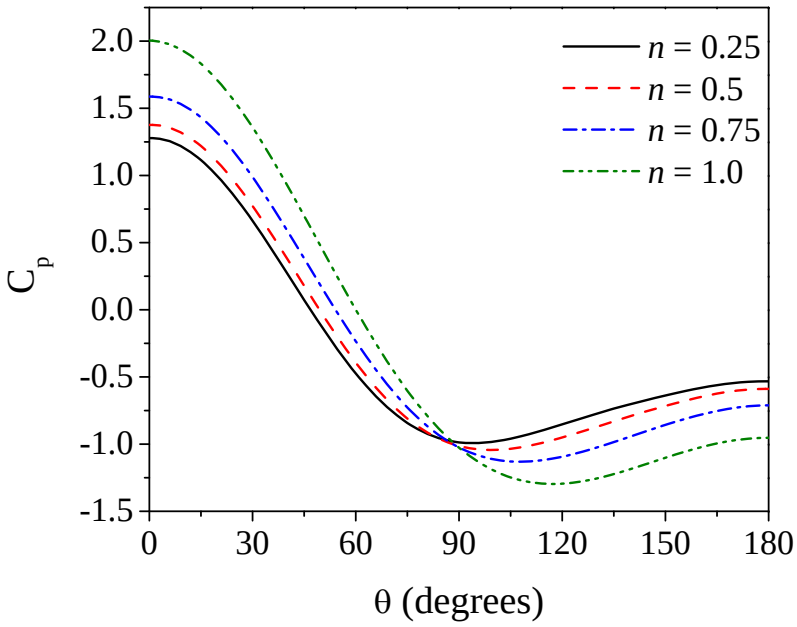

Figure 5.78: Effect of the parameter n on C_p.

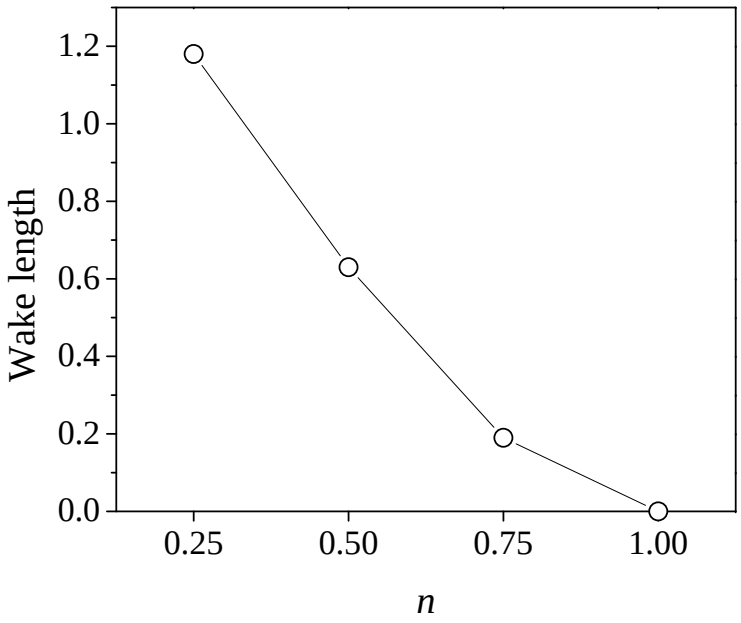

Figure 5.79: Effect of the parameter n on the wake length L.

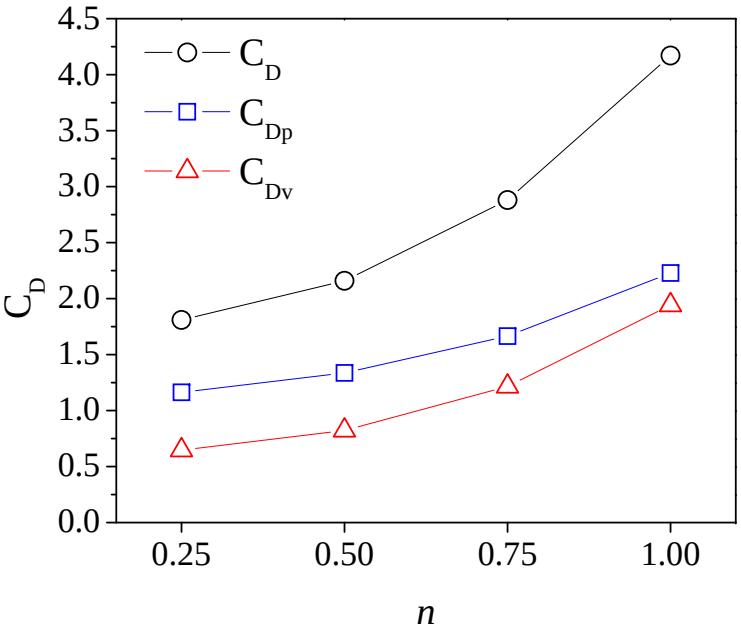

Figure 5.80: Effect of the parameter n on the drag coefficient.

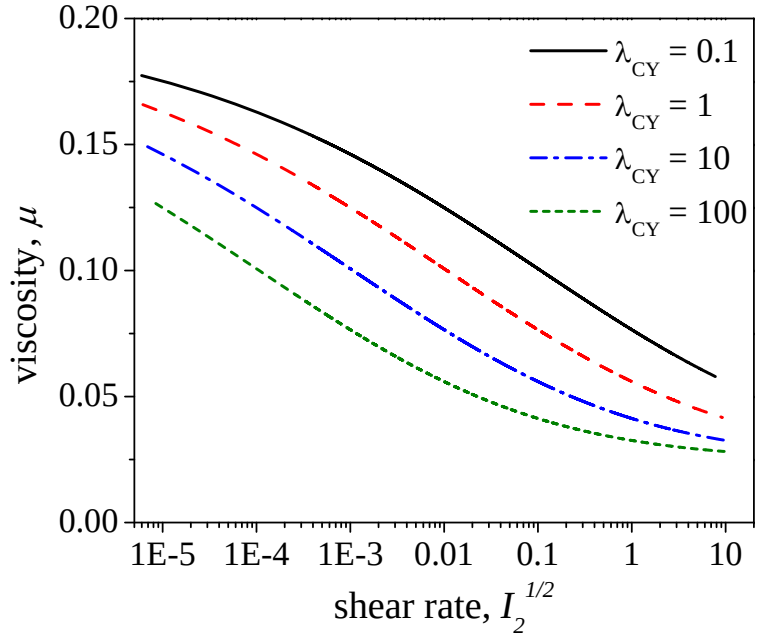

Figure 5.81: Viscosity curves for various λ_{CY}.

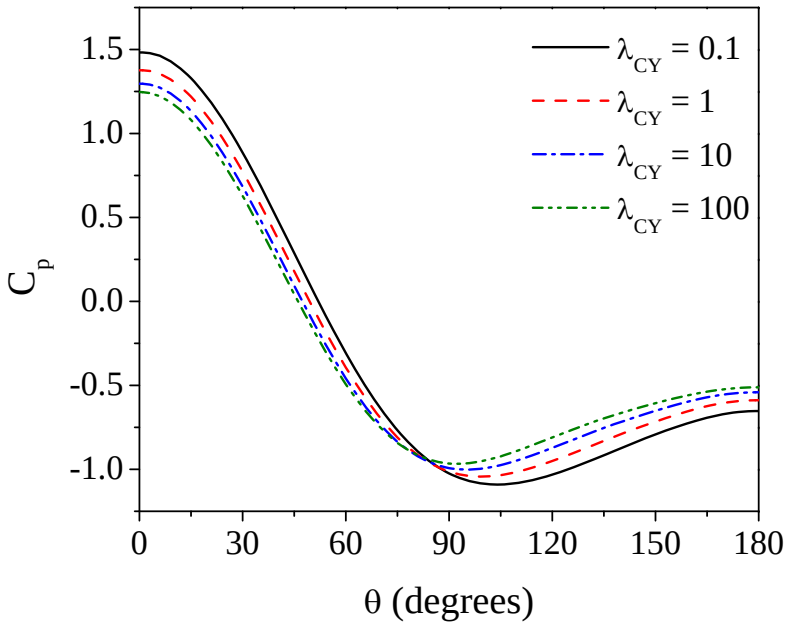

Figure 5.82: Effect of the parameter λ_{CY} on C_p.

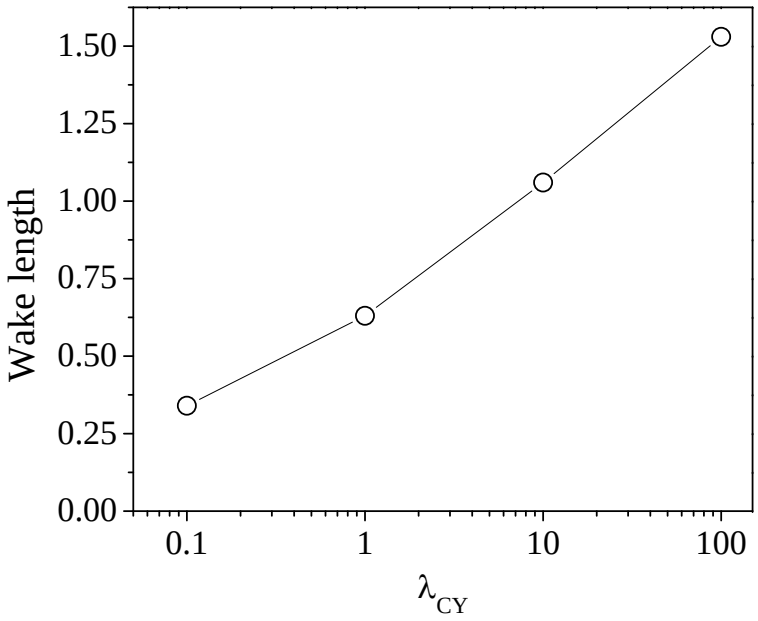

Figure 5.83: Effect of the parameter λ_{CY} on the wake length L.

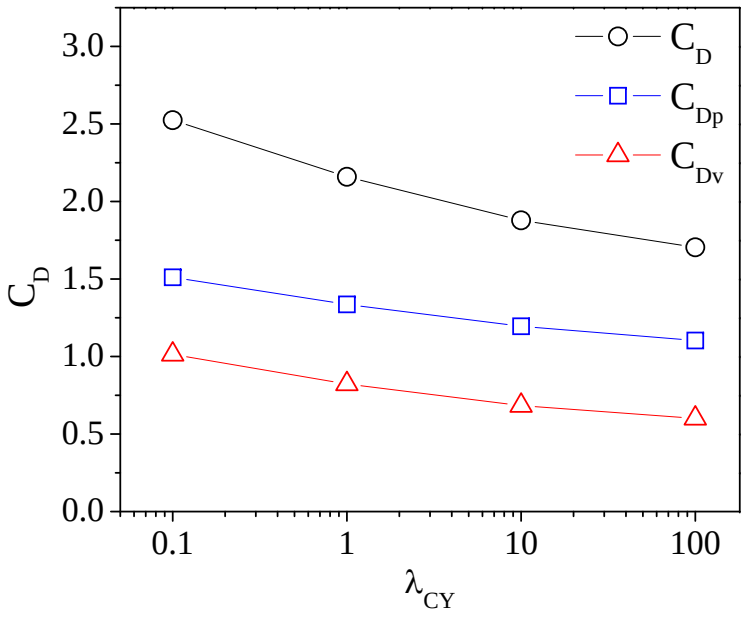

Figure 5.84: Effect of the parameter λ_{CY} on the drag coefficient.

In summary, we have investigated that the variation in the three Carreau–Yasuda parameters $(a,\, n,\, \lambda_{CY})$ makes the viscosity change in different ways, which affects the pressure coefficient along the cylinder surface, wake length, and pressure and viscous drag coefficients. The pressure drag is larger than viscous drag in all test cases because of the shape of a circular cylinder. The L_2 least-squares functionals in all cases of the parameter study are order of 10^{-7}.

5.7 Fully developed flow between parallel plates

5.7.1 Problem description

We consider a two-dimensional non-isothermal fully developed flow between parallel plates where the flow is driven by pressure difference. The viscosity is assumed to be independent of temperature and Eq. (2.5) was used. The temperature field in this problem is purely due to viscous dissipation. The geometry of the computational domain and the boundary conditions for the problems are depicted in Figure 5.85. $2H$ and L denote, respectively, the distance between the plates and the length of the plates. Due to the symmetry about x-axis, only the upper half of the flow domain is considered. Along the top plate, the velocity components are taken to be zero according to the no-slip condition and temperature is fixed to zero. Pressure is specified as zero at the left boundary and $p_{out}(> 0)$ at the right boundary, so that the flow is driven by the pressure difference in the positive x-direction. Since it is fully developed flow (so, the flow does not change in x-direction), y-component of velocity and x-component of heat flux are taken to be zero at the right and left boundaries. The bottom boundary has the symmetry conditions of $v_y = 0$, $\tau_{xy} = 0$, and $q_y = 0$. At the top left and top right corners, the boundary conditions are ($v_x = 0$, $v_y = 0$, $\theta = 0$, $p = 0$) and ($v_x = 0$, $v_y = 0$, $\theta = 0$, $p = p_{out}$), respectively. The characteristic quantities for the Reynolds number and Carreau number of Eq. (2.8) are $v_0 = 1.0$ and $L_0 = D_H = 4H$, where D_H is the hydraulic diameter which is equal to two times the distance between the parallel plates $(D_H = 4H)$, if we assume that the width (into the plane of the page) of the plates is much larger than the distance between the plates ($w \gg 2H$). The computational domain is discretized into a uniform 2×4 mesh of rectangular elements as shown in Figure 5.85. The polynomial order of p=4

is chosen for this problem, since the numerical results (which are presented below) do not show dependence on p-level when it is larger than 3 for the mesh. Nonlinear convergence is declared when the Euclidean norm of the difference between two consecutive iteration solutions is less than 10^{-3}.

5.7.2 Verification and validation tests

To verify the present LSFEM code for non-isothermal flows with viscous dissipation, the numerical results of present study are compared with analytical solutions for Newtonian fluids and with numerical results of previous study for generalized Newtonian fluids. For Newtonian fluids, the analytical solutions of the horizontal velocity (v_x) and temperature field (θ) are given by [61, 69]

$$v_x = -\frac{H^2}{2\mu}\frac{\partial p}{\partial x}\left(1 - \frac{y^2}{H^2}\right) \tag{5.19a}$$

$$\theta = \theta_H + \frac{\mathrm{Re}\,\mathrm{Br}}{12\,\mu}\left(\frac{\partial p}{\partial x}\right)^2 H^4\left(1 - \frac{y^4}{H^4}\right), \tag{5.19b}$$

where the viscosity μ is equal to Eq. (2.5) with $n = 1$ and θ_H denotes the temperature at $y = H$ ($\theta_H = 0$). The dimensionless numbers used are Re = 55.61, Pr = 1.49, Pe = 82.85 and Br = 0.63 (the definitions of these dimensionless numbers are in Eq. (2.13). Fig. 5.86 and Fig. 5.87 show the comparison between the analytical solutions (Eq. (5.19)) and the present numerical results of horizontal velocity and temperature, respectively for two values of $\partial p/\partial x$. The numerical results of x-velocity and temperature profiles for both values of $\partial p/\partial x$ demonstrate good agreement with the analytical solutions. Here, $\partial p/\partial x = (p_{in} - p_{out})/L = -p_{out}$ (see Fig. 5.85). The higher pressure derivative with respect to x gives faster horizontal velocity and higher temperature, as the analytical solutions of Eq. (5.19) indicate.

For generalized Newtonian fluids, we compared the present results with the numerical results of Surana et al. [61]. The parameters of Carreau–Yasuda viscosity model (Eq. (2.5)) are $\mu_0 = 0.18$, $mu_\infty = 0$, $n = 0.729$, $a = 2.0$ and λ_{CY} = 4.8. The same dimensionless numbers with those for Newtonian fluids are used (i.e., Re = 55.61, Pr = 1.49, Pe = 82.85, Br = 0.63). As shown in Fig.

5.88 and 5.89, the present numerical results of x-velocity and temperature profiles for both values of $\partial p/\partial x$ are in good agreement with the results of Surana et al. [61]. Similar with the Newtonian fluids, the results for Carreau–Yasuda fluids also exhibit that increasing the pressure derivative with respect to x leads to faster horizontal velocity and higher temperature.

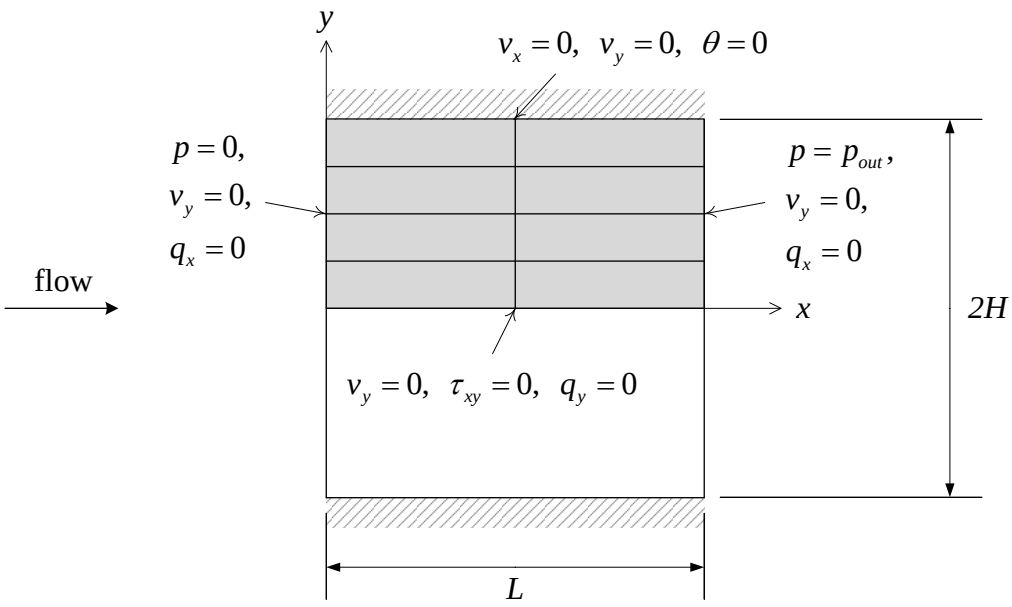

Figure 5.85: Schematic for the problem of fully developed flow between parallel plates ($H = 1$, $L = 1$).

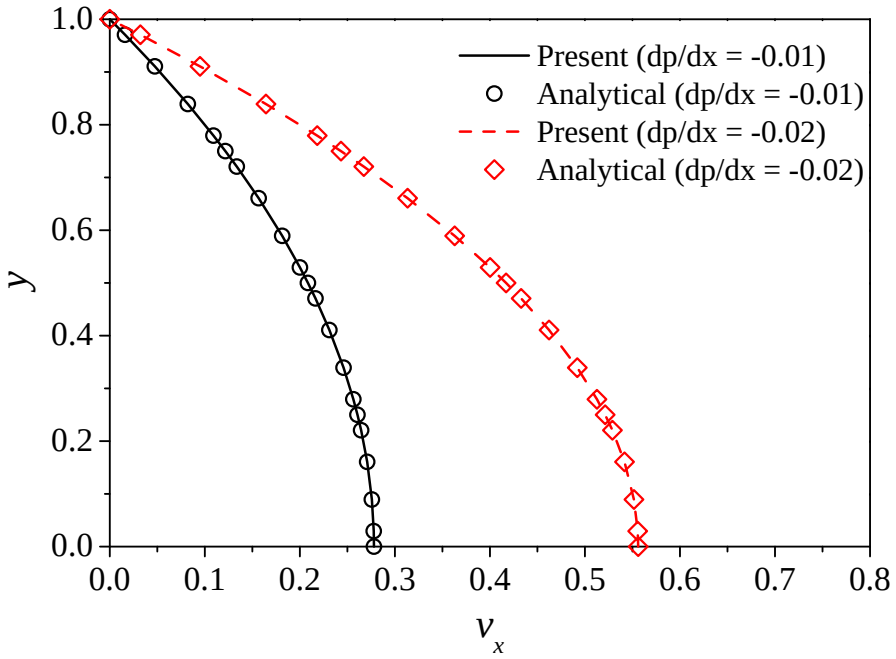

Figure 5.86: Horizontal velocity profiles of Newtonian fluids (Re = 55.6, $n = 1$).

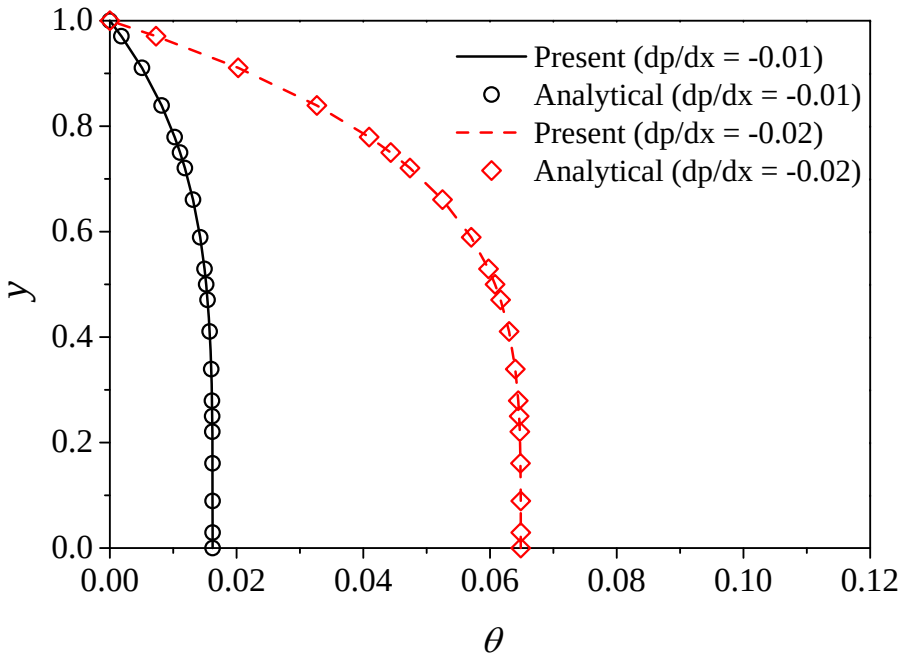

Figure 5.87: Temperature profiles of Newtonian fluids (Re = 55.6, $n = 1$).

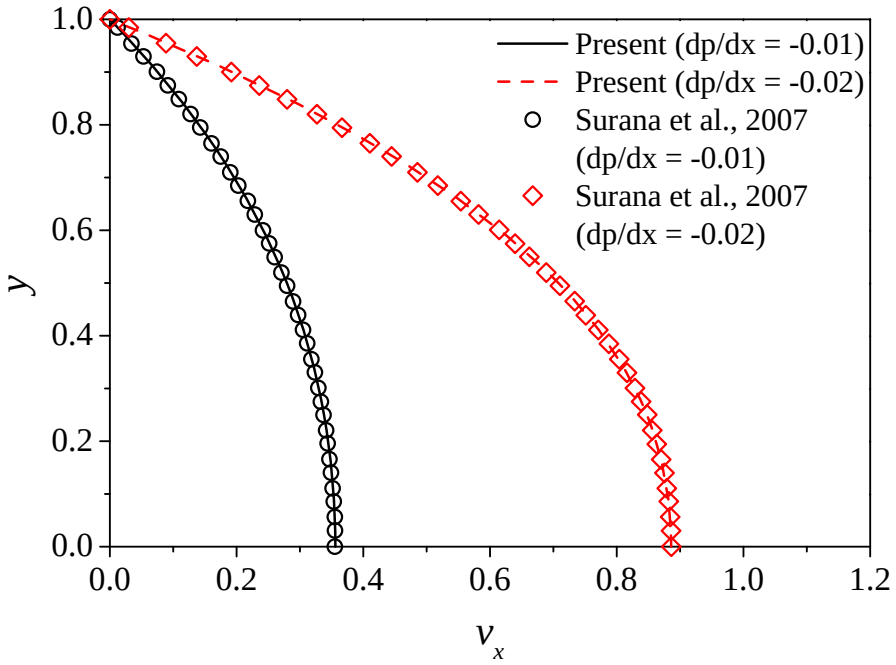

Figure 5.88: Horizontal velocity profiles of Carreau–Yasuda fluids (Re = 55.6, $n = 0.729$, $a = 2.0$, $\lambda_{CY} = 4.8$).

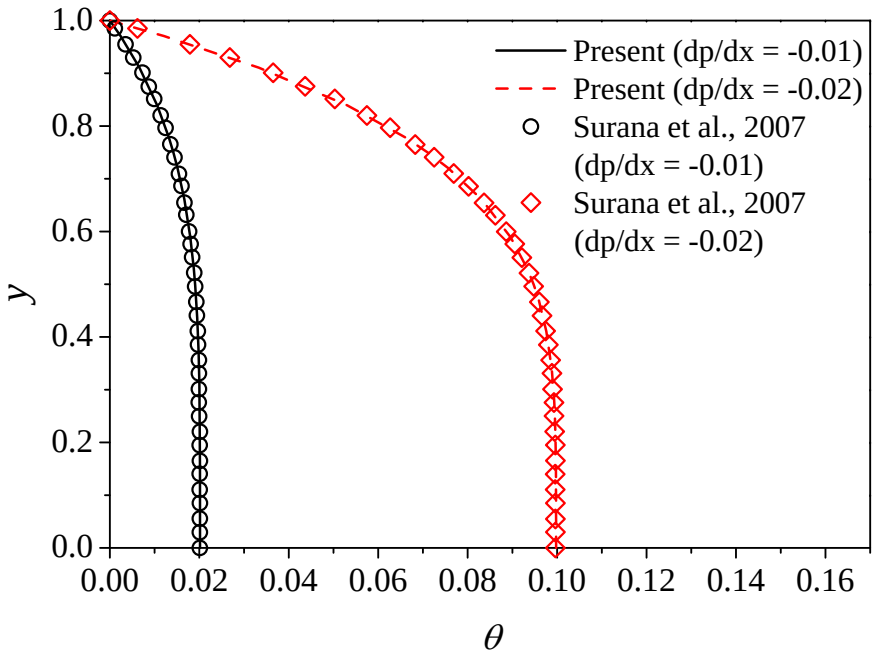

Figure 5.89: Temperature profiles of Carreau–Yasuda fluids (Re = 55.6, $n = 0.729$, $a = 2.0$, $\lambda_{CY} = 4.8$).

5.7.3 Parametric study of Carreau–Yasuda fluids

The effects of the three parameters (a, n, λ_{CY}) of the Carreau–Yasuda model, Eq. (2.5), on the flow between parallel plates were studied. We used $\partial p/\partial x = -0.02$ and the same dimensionless numbers (Re = 55.61, Pr = 1.49, Pe = 82.85, Br = 0.63) as in the verification tests. The upper and lower limiting viscosities of Eq. (2.5) are set to $\mu_0 = 0.18$ and $mu_\infty = 0$, respectively. In Figures 5.90–5.91, 5.94–5.95 and 5.98–5.99 the influence of change in a, n, λ_{CY} on the velocity and temperature profiles are shown, Figures 5.92, 5.96 and 5.100 present the viscosity curves with respect to shear rate in the fluid domain, and Figures 5.93, 5.97 and 5.101 viscous dissipation for various values of a, n and λ_{CY}. As the shape parameter a decreases, the viscosity decreases (Figure 5.92) and the velocity profile (Figure 5.90) shows that the fluid with lower a (that is, lower viscosity) moves faster with higher velocity gradient at wall. Temperature is also increased with decreasing a (Figure 5.91), because viscous dissipation which causes fluid temperature to rise increases as a decreases (Figures 5.93). Although the viscosity is decreased with decreasing a, velocity gradient at wall as shown in Figure 5.90 becomes much higher for smaller a such that the viscous dissipation (see Eq. (2.12)) increases as a decreases. For the power index n, viscosity decreases as n decreases (Figure 5.96) and thus the fluid with lower n moves faster with higher velocity gradient at wall as in Figure 5.94. As viscous dissipation increases with decrease in n (Figures 5.97), temperature rises with decreasing n (Figure 5.95). Increase in time constant λ_{CY} makes viscosity lower (Figure 5.100) and thus the fluid with higher λ_{CY} moves faster with higher velocity gradient at wall as in Figure 5.98. Viscous dissipation increases with λ_{CY} as shown in Figures 5.101, which leads to rise in temperature with increasing λ_{CY} (Figure 5.99).

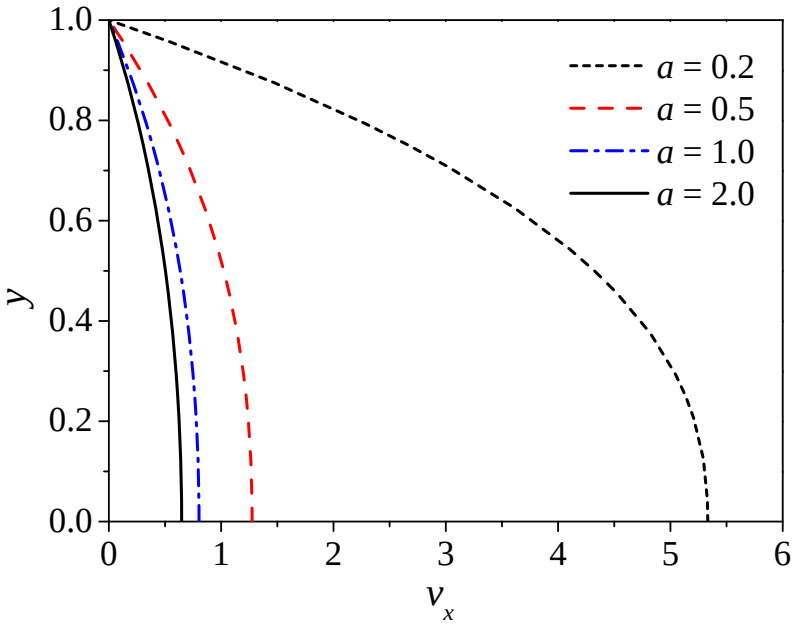

Figure 5.90: Effect of the parameter a on velocity profile ($n = 0.5$, $\lambda_{CY} = 1.0$).

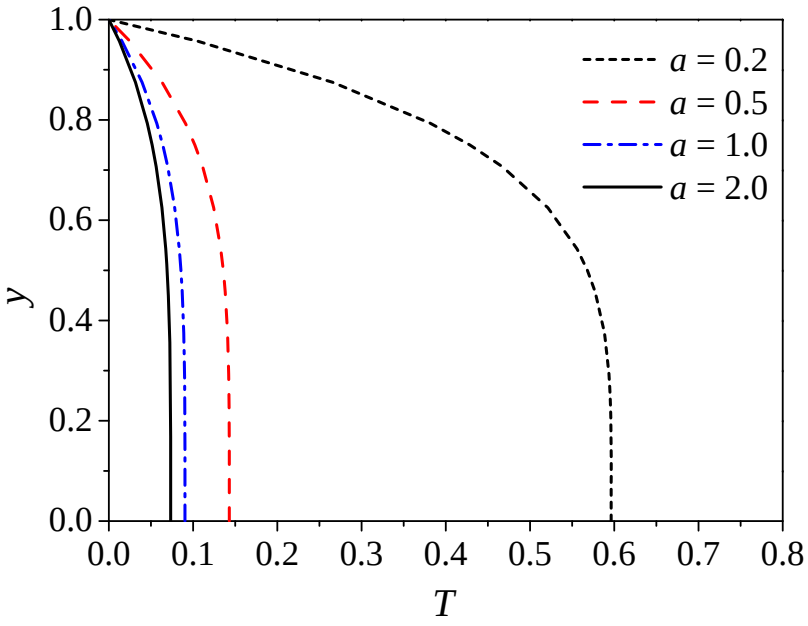

Figure 5.91: Effect of the parameter a on temperature profile ($n = 0.5$, $\lambda_{CY} = 1.0$).

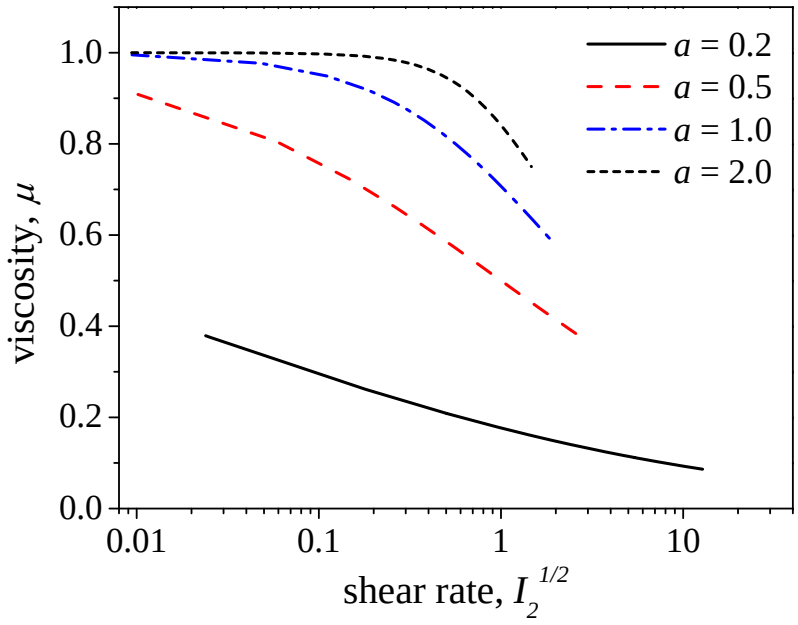

Figure 5.92: Effect of the parameter a on viscosity ($n = 0.5$, $\lambda_{CY} = 1.0$).

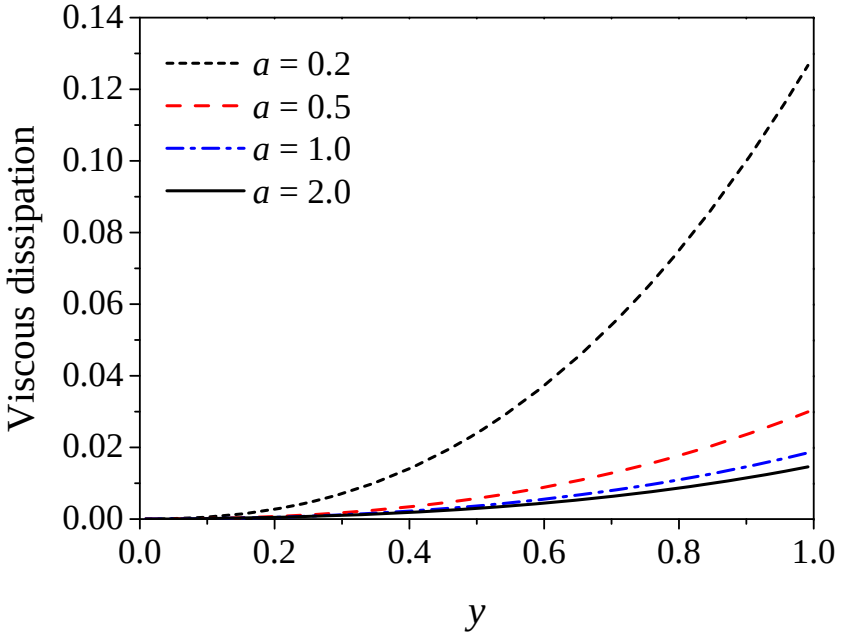

Figure 5.93: Effect of the parameter a on viscous dissipation ($n = 0.5$, $\lambda_{CY} = 1.0$).

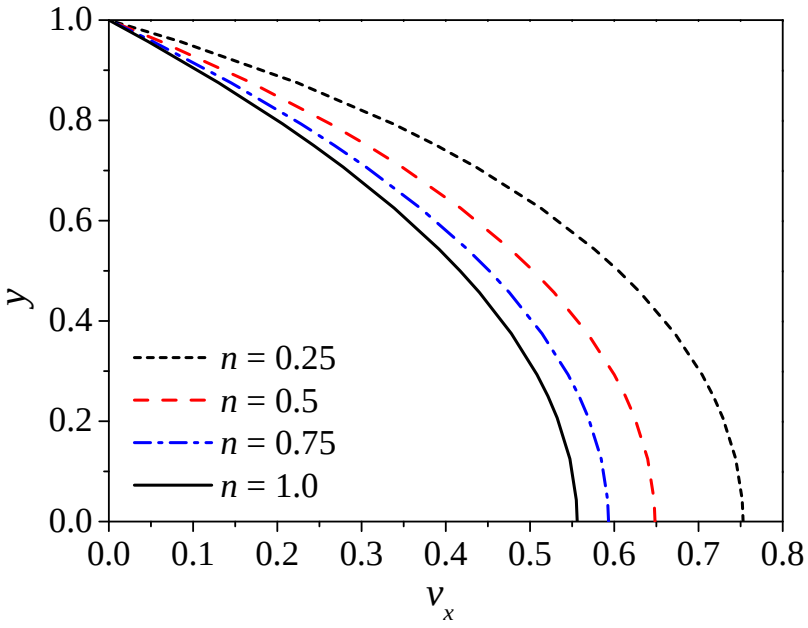

Figure 5.94: Effect of the parameter n on velocity profile ($a = 2.0$, $\lambda_{CY} = 1.0$).

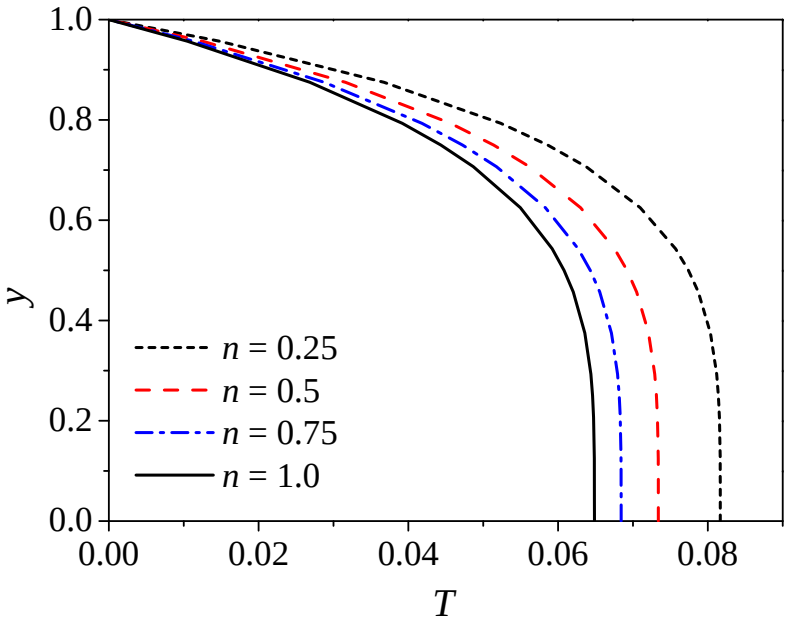

Figure 5.95: Effect of the parameter n on temperature profile ($a = 2.0$, $\lambda_{CY} = 1.0$).

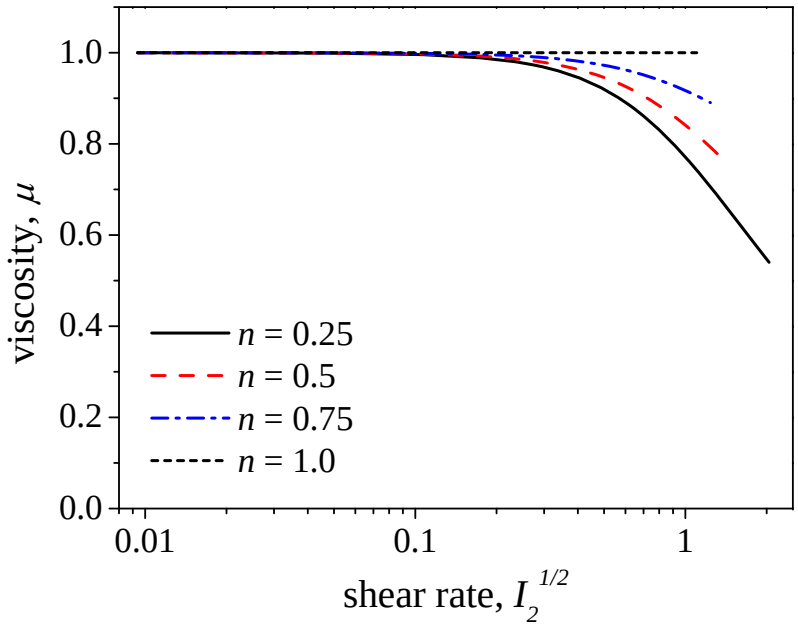

Figure 5.96: Effect of the parameter n on viscosity ($a = 2.0$, $\lambda_{CY} = 1.0$).

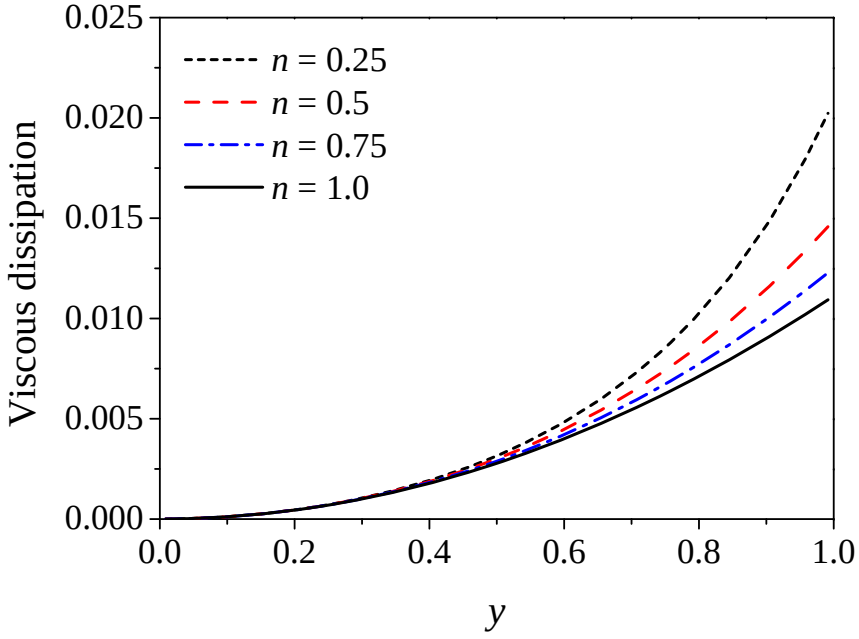

Figure 5.97: Effect of the parameter n on viscous dissipation ($a = 2.0$, $\lambda_{CY} = 1.0$).

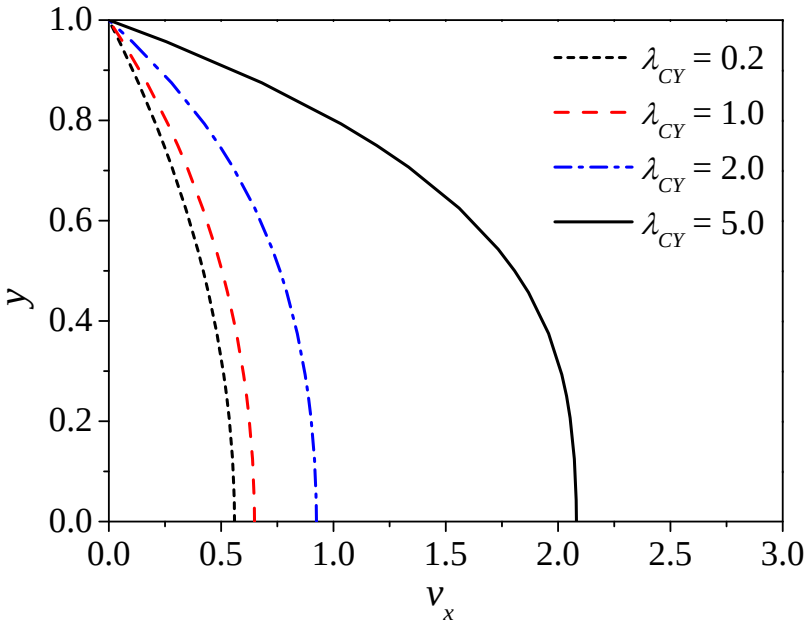

Figure 5.98: Effect of the parameter λ_{CY} on velocity profile ($a = 2.0$, $n = 0.5$).

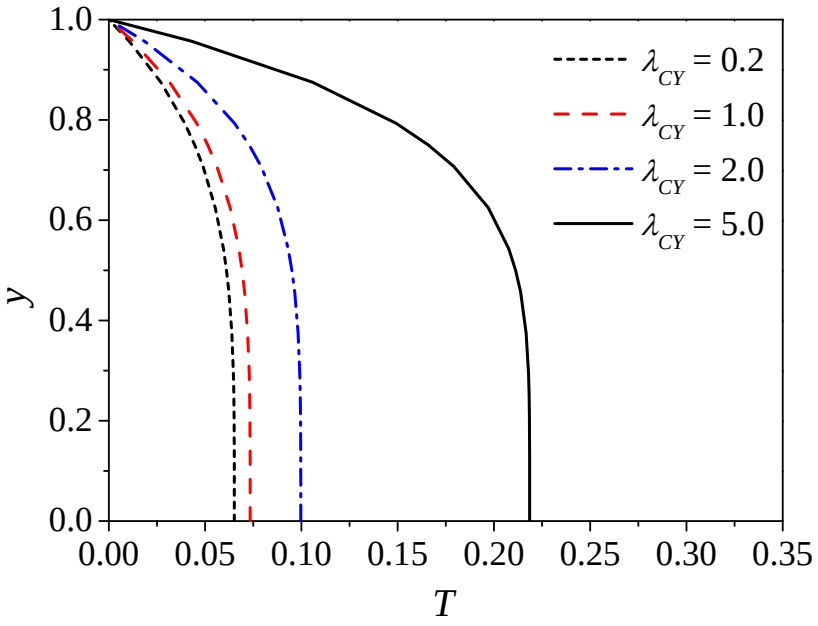

Figure 5.99: Effect of the parameter λ_{CY} on temperature profile ($a = 2.0$, $n = 0.5$).

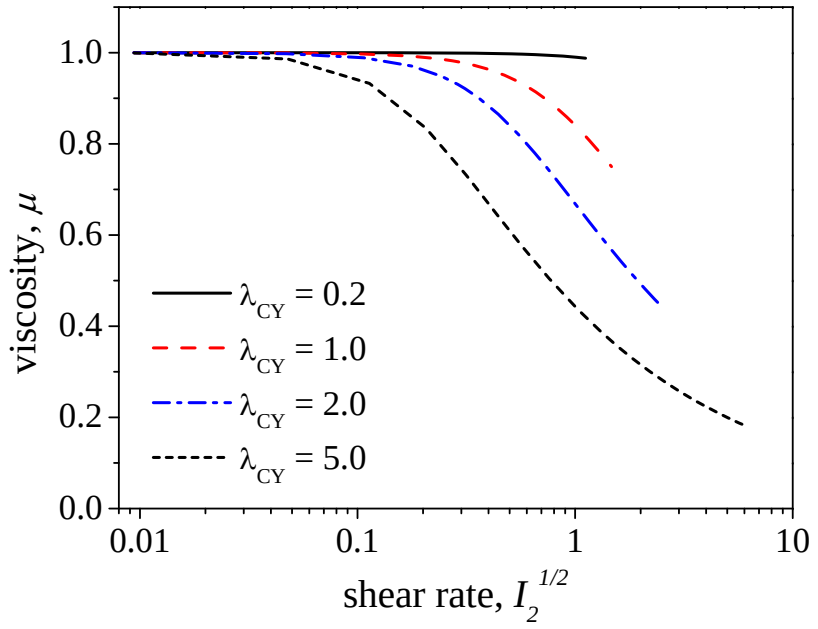

Figure 5.100: Effect of the parameter λ_{CY} on viscosity ($a = 2.0$, $n = 0.5$).

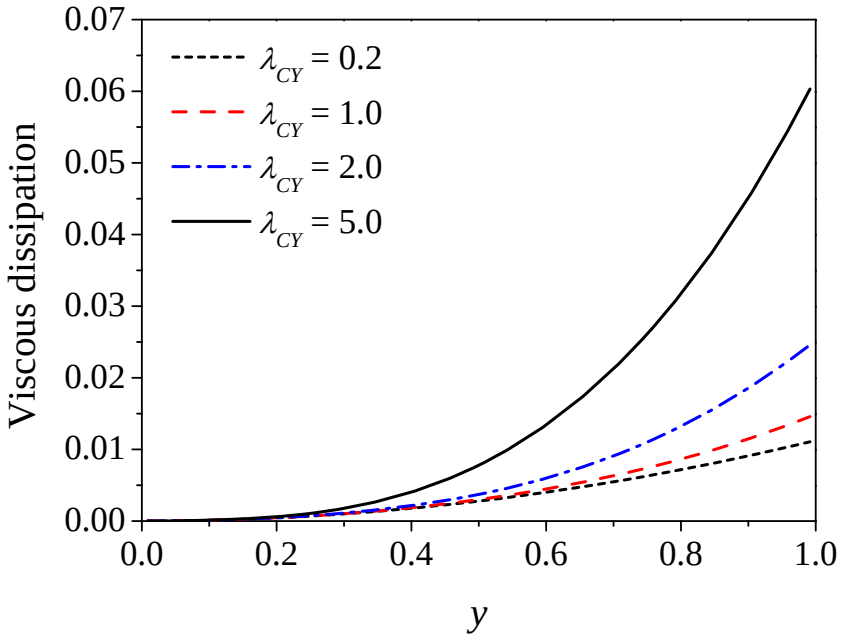

Figure 5.101: Effect of the parameter λ_{CY} on viscous dissipation ($a = 2.0$, $n = 0.5$).

5.8 Buoyancy-driven flow in a cubic cavity

5.8.1 Problem description

Three-dimensional, steady, buoyancy-driven flow in a cubic cavity is considered. Fluid is in a unit cavity, $[0,1] \times [0,1] \times [0,1]$, where two vertical walls are heated differently as shown in Figure 5.102. Temperature at right side is hotter than left side wall ($T_H > T_C$). And remaining four walls are insulated. This temperature difference causes buoyancy force which makes fluid rotate in counter-clock-wise direction (see Figure 5.103). The flow is symmetric about the xy-plane at the center ($z = 0.5$), so only half of the domain ($[0,1] \times [0,1] \times [0,0.5]$) was considered. Figure 5.105 presents the boundary conditions for the problem. Except the symmetry plane ($z = 0.5$), all velocity components are zero at five walls ($v_x = v_y = v_z = 0$). Right and left vertical walls have specified temperatures ($\theta = \theta_H$,$\theta = \theta_C$) and top, bottom and rear walls are insulated ($q_y = 0$, $q_z = 0$). At the symmetry plane, z-component of velocity (v_z), shear stresses (τ_{xz}, τ_{yz}) and z-component of heat flux (q_z) are zero. The computational domain is discretized into a non-uniform $8 \times 8 \times 4$ mesh of rectangular parallelepiped elements. The mesh is graded such that the boundary layer thickness is resolved. Nonlinear convergence is declared when the Euclidean norm of the difference between two consecutive iteration solutions is less than 10^{-3}.

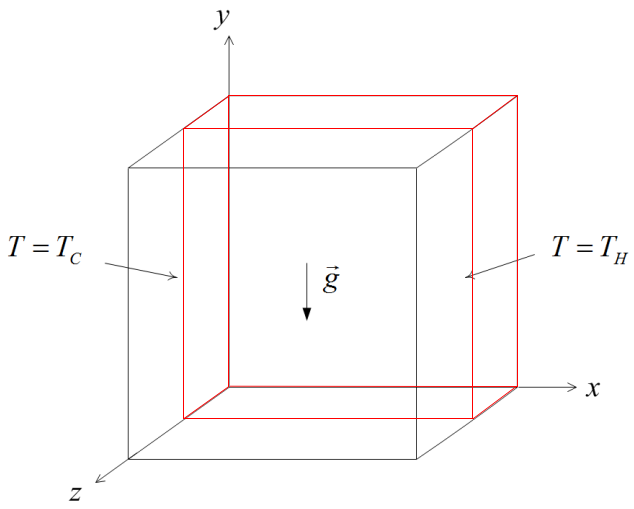

Figure 5.102: Schematic for the problem of 3-D buoyancy-driven cavity flow ($[0,1] \times [0,1] \times [0,1]$).

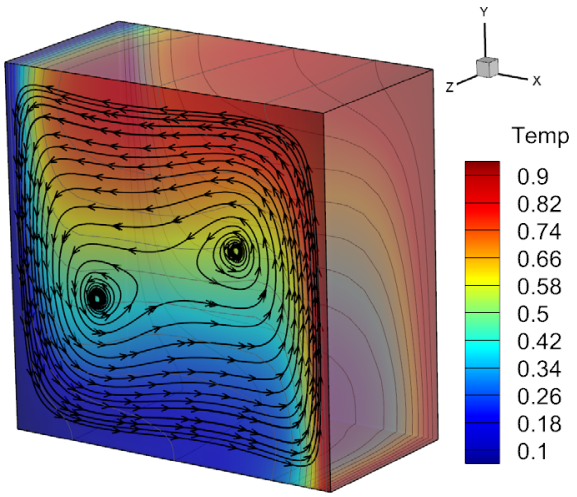

Figure 5.103: Temperature field of half domain ($[0,1] \times [0,1] \times [0,0.5]$) and streamlines at the symmetry plane ($z = 0.5$).

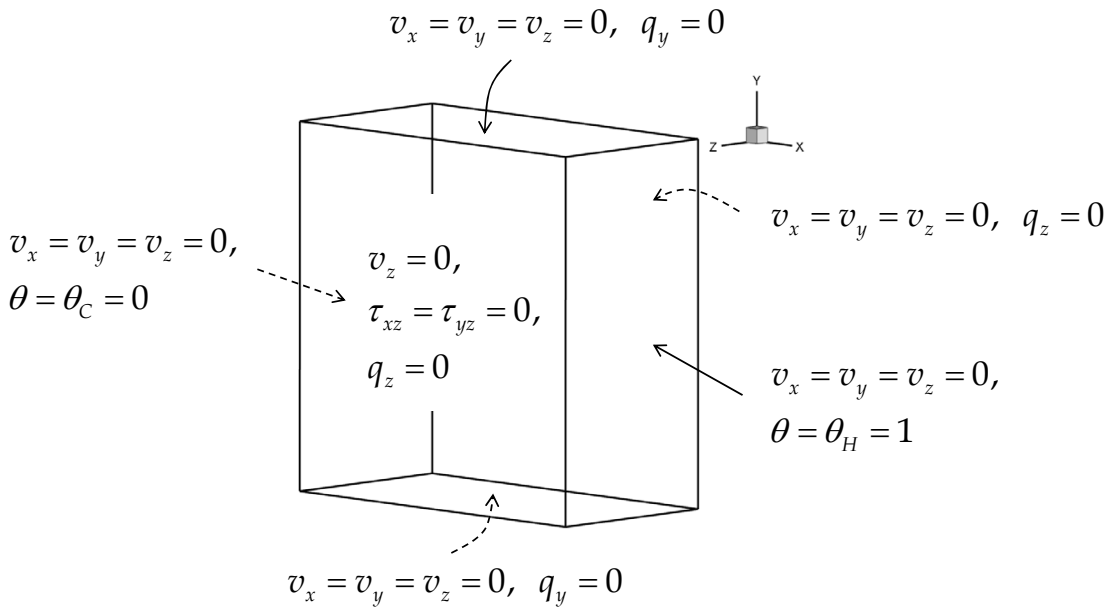

Figure 5.104: Boundary conditions for the problem of 3-D buoyancy-driven cavity flow.

5.8.2 Verification and validation tests

We compared our results for Newtonian fluids with the previous numerical results by Fusegi et al. [103] and experimental results by Krane and Jessee [2] to verify and validate the current least-squares finite element model for 3-D non-isothermal flow with buoyancy effect. By comparing with the work of Fusegi et al. [103] who used 3rd-order finite difference method with 64^3 gird points, we showed the dependency of numerical solutions on polynomial order, p. Since it is for Newtonian fluids, we set $n = 1$ in Eq. (2.5), which makes the viscosity constant ($\mu = \mu_0$). Figure 5.105 and 5.106 show the vertical velocity profiles along the line at $y = 0.5$ and horizontal velocity profiles along the line at $x = 0.5$ on the symmetric plane ($z = 0.5$) of the cavity, respectively, when Ra $= 10^5$ and Pr $= 0.71$. In Figure 5.107 and 5.108, temperature profiles along the line at $y = 0.5$ and the line at $x = 0.5$, respectively, on the symmetric plane are shown with the same values of Ra and Pr. The numerical results for both velocity and temperature approaches p-independence when p> 3 and we used p$= 4$ therefore for the following tests. The converged solutions are in good agreement with [103].

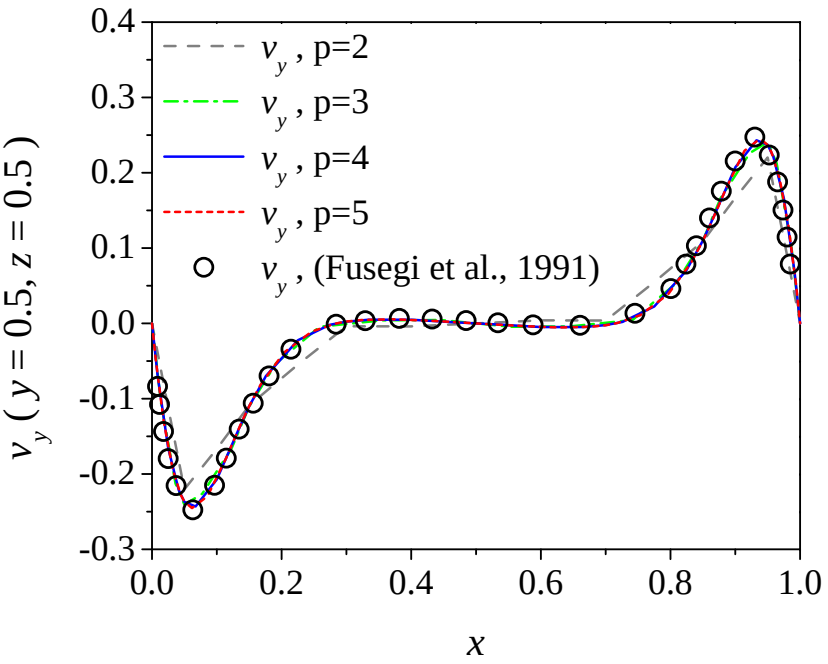

Figure 5.105: Vertical velocity v_y along the line $y = 0.5$ on the symmetric plane ($z = 0.5$) of the cavity for Newtonian fluid (Ra $= 10^5$, Pr $= 0.71$)).

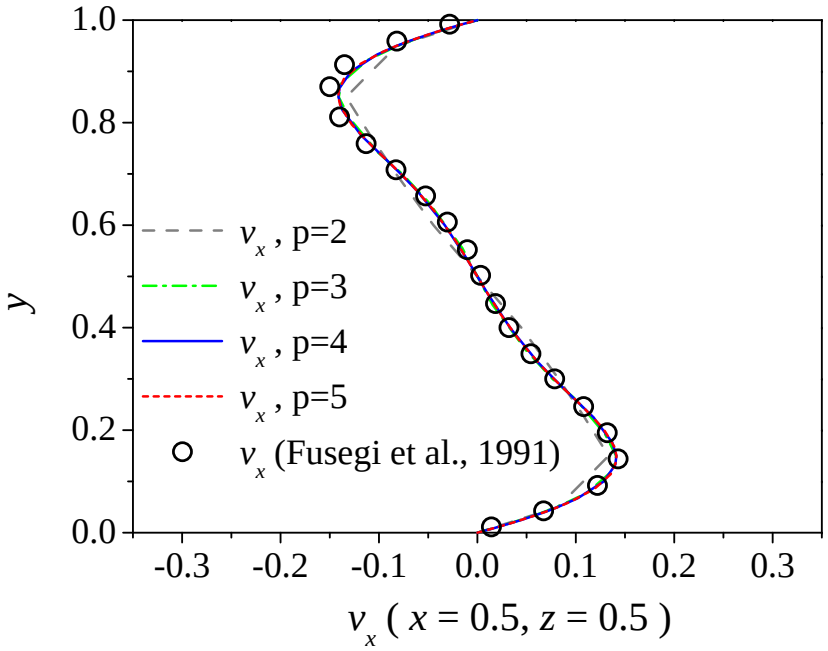

Figure 5.106: Horizontal velocity v_x along the line $x = 0.5$ on the symmetric plane ($z = 0.5$) of the cavity for Newtonian fluid (Ra $= 10^5$, Pr $= 0.71$)).

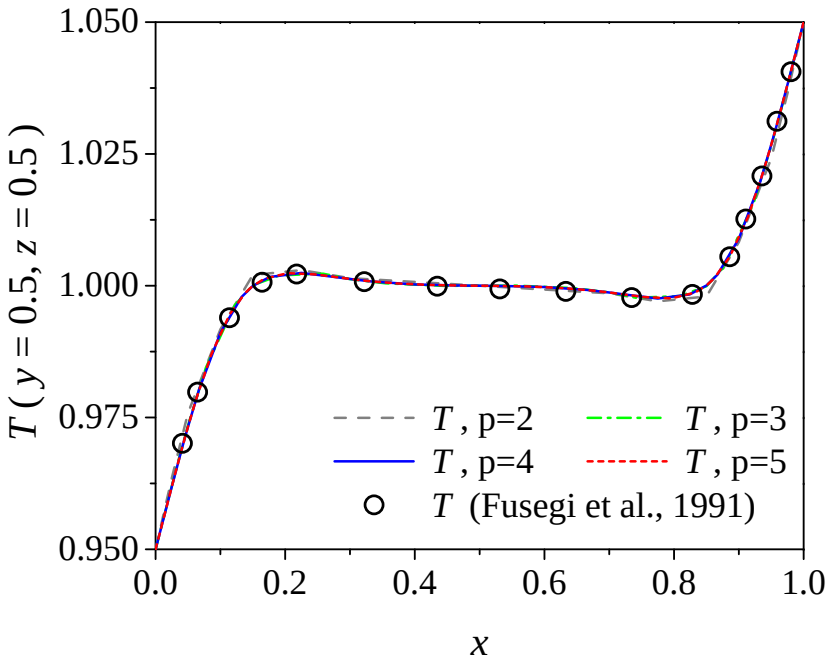

Figure 5.107: Temperature along the line $y = 0.5$ on the symmetric plane ($z = 0.5$) of the cavity for Newtonian fluid (Ra $= 10^5$, Pr $= 0.71$).

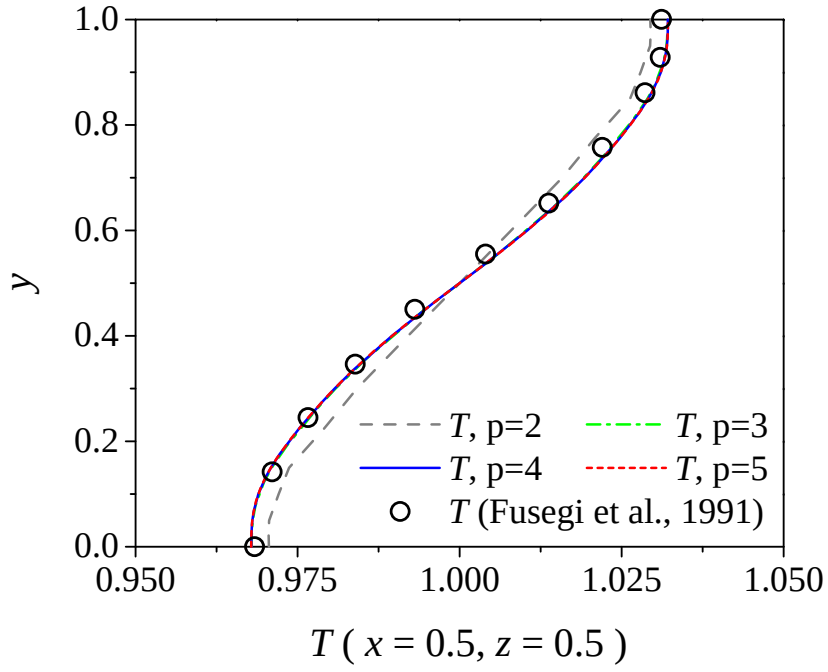

Figure 5.108: Temperature along the line $x = 0.5$ on the symmetric plane ($z = 0.5$) of the cavity for Newtonian fluid (Ra $= 10^5$, Pr $= 0.71$).

Another important quantity is Nusselt number, Nu, which is a dimensionless heat transfer rate or has a meaning of the ratio of convective to conductive heat transfer across the surface. Figure 5.109 shows a x-component of heat flux (q_x) at the heated surface ($x = 1$). Using q_x, we can compute local Nu (Eq. (5.20a)) on the surface. The overall Nu on this surface is then computed by integrating local Nu over the surface as in Eq. (5.20b). The computed $\text{Nu}_{\text{overall}}$ is 4.332 and it shows good agreement with the result of [103] who had $\text{Nu}_{\text{overall}} = 4.361$.

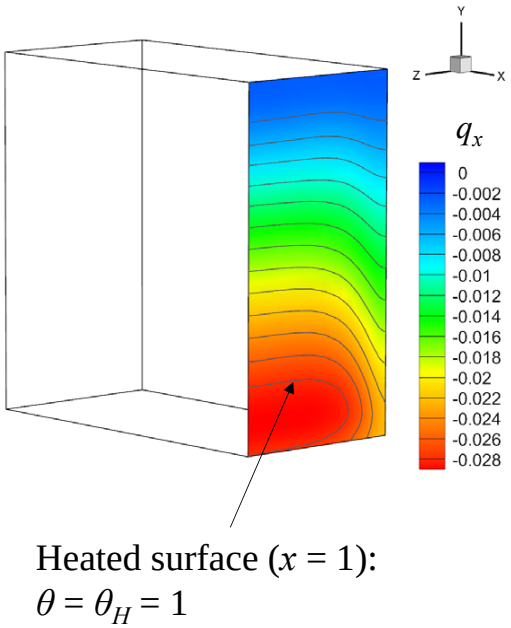

Figure 5.109: q_x contour of the heated surface ($x = 1$) of the cavity.

$$\text{Nu}_{\text{local}}(y,z)_{x=1} = \left[\frac{\partial\theta}{\partial x}\right]_{x=1} \tag{5.20a}$$

$$\text{Nu}_{\text{overall}} = \int_0^1\int_0^1 \text{Nu}_{\text{local}}(y,z)_{x=1}\,dydz = -\int_0^1\int_0^1 (\text{Pe}\,q_x)_{x=1}\,dydz \tag{5.20b}$$

We also compare our numerical results with the experimental results of Krane and Jessee [2]. They used air as fluid in the cavity where the two vertical walls were heated differently with

$T_C = 0.95$ and $T_H = 1.05$ (see Figure 5.102) and the remaining walls were insulated. The dimensionless numbers for their experiment are Ra $= 1.89 \times 10^5$ and Pr $= 0.71$. Although air is a compressible fluid, this buoyancy-driven flow problem can also be simulated well by the governing equations for incompressible flow with Boussinesq approximation. They wanted to have top and bottom wall insulated, but perfect insulation could not be realized in their experiments as in Figure 5.110. The Figure 5.110 shows their experimental temperature profile along the line at $y = 0.5$ and we can see that the slope at top/bottom walls are not zero, that is, they are not insulated. So, to compare with their results, we imposed constant heat flux in y-direction at top ($q_y(y = 1) = 0.00435$) and bottom ($q_y(y = 1) = 0.0045$) walls using their experiment data. Figure 5.111 and 5.112 present the vertical velocity along the line at $y = 0.5$ and horizontal velocity along the line at $x = 0.5$ on the symmetric plane ($z = 0.5$) of the cavity, respectively, and Figure 5.113 and 5.114 shows temperature along the line at $y = 0.5$ and the line at $x = 0.5$, respectively, on the symmetric plane. Both velocity and temperature profiles are in good agreement with the experimental data of [2].

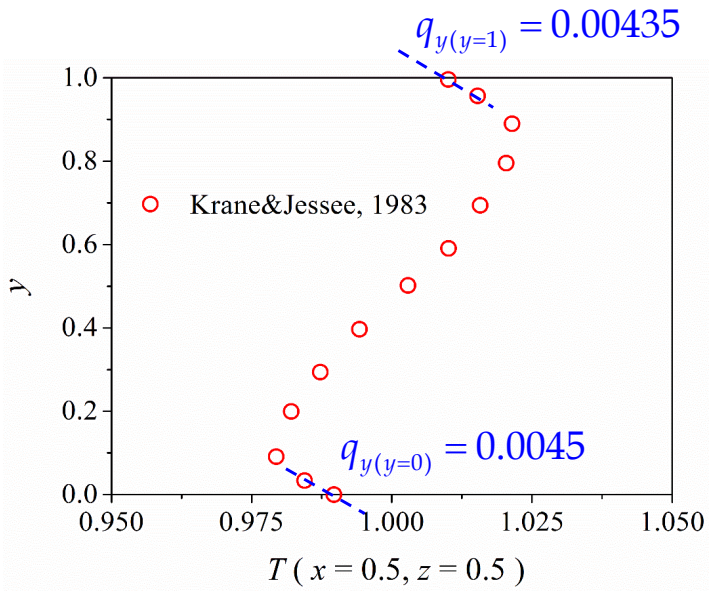

Figure 5.110: Experimental temperature data [2] along the line $x = 0.5$ on the symmetric plane ($z = 0.5$) of the cavity (Ra $= 1.89 \times 10^5$, Pr $= 0.71$).

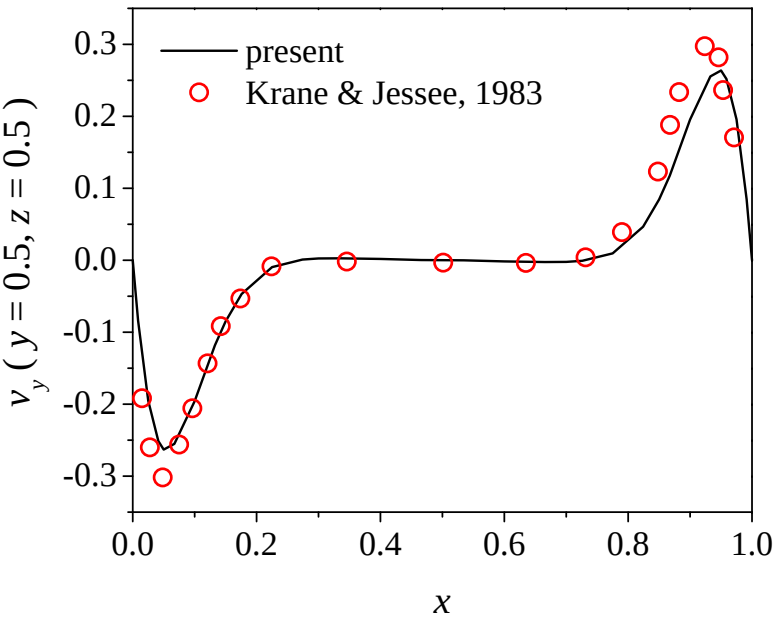

Figure 5.111: Vertical velocity v_y along the line $y = 0.5$ on the symmetric plane ($z = 0.5$) of the cavity (Ra $= 1.89 \times 10^5$, Pr $= 0.71$).

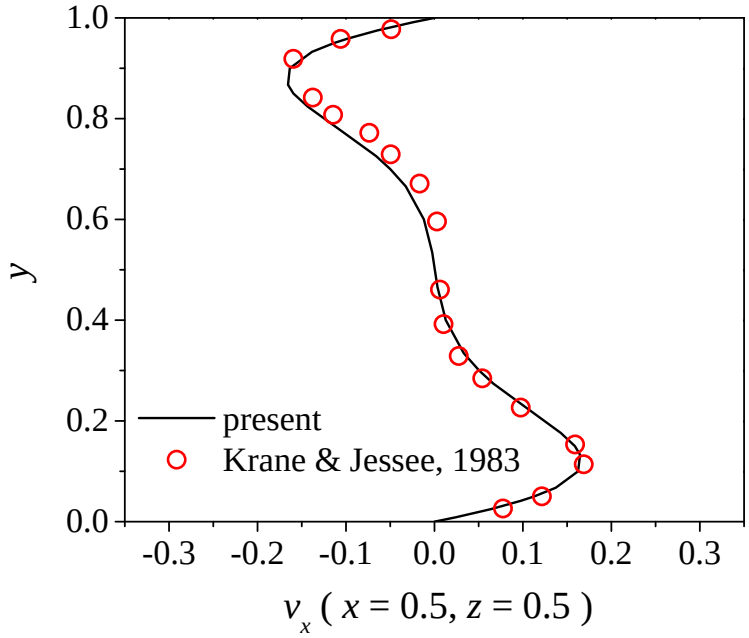

Figure 5.112: Horizontal velocity v_x along the line $x = 0.5$ on the symmetric plane ($z = 0.5$) of the cavity (Ra $= 1.89 \times 10^5$, Pr $= 0.71$).

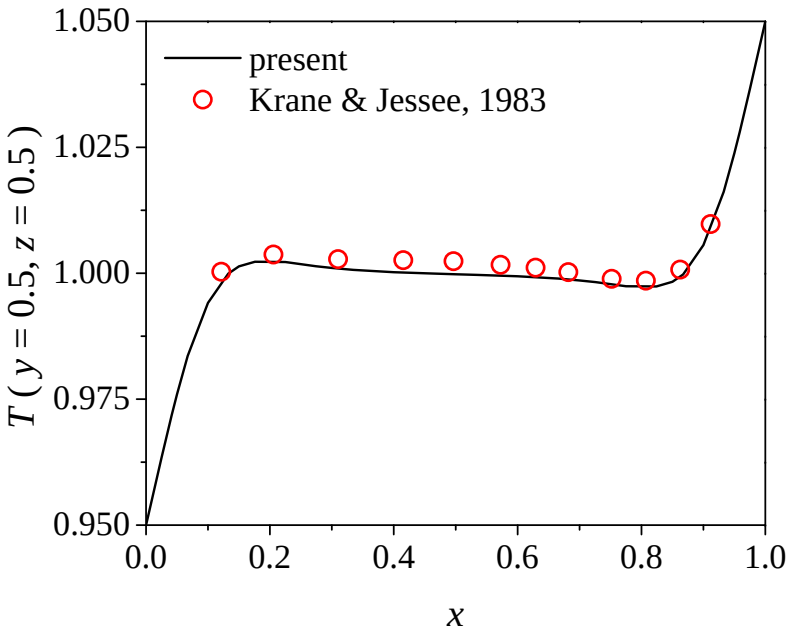

Figure 5.113: Temperature along the line $y = 0.5$ on the symmetric plane ($z = 0.5$) of the cavity (Ra $= 1.89 \times 10^5$, Pr $= 0.71$).

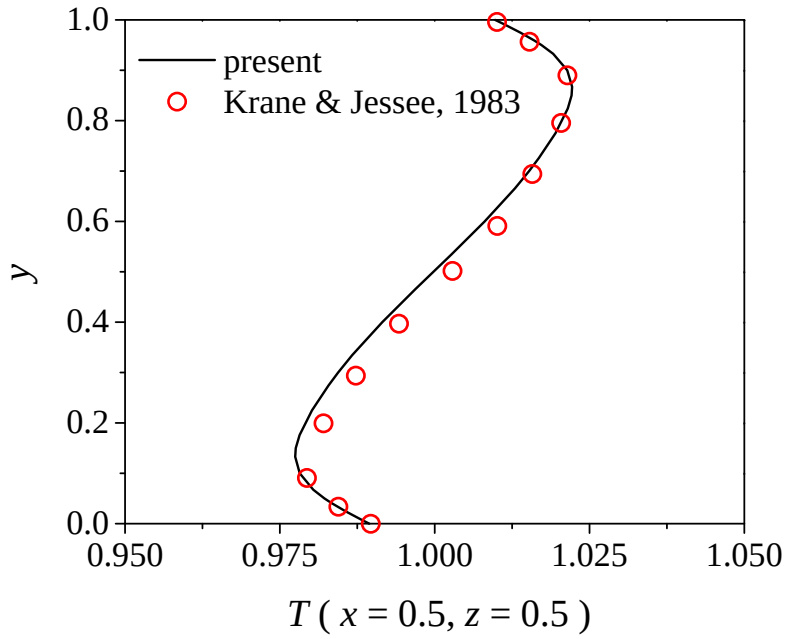

Figure 5.114: Temperature along the line $x = 0.5$ on the symmetric plane ($z = 0.5$) of the cavity (Ra $= 1.89 \times 10^5$, Pr $= 0.71$).

5.8.3 Parametric study of Carreau–Yasuda fluids

After verifying and validating the current model for Newtonian fluids, we examine how the change in parameters (a, n, λ_{CY}) of the Carreau–Yasuda model, Eq. (2.5), affects the buoyancy-driven flow in the differently heated cavity (Figure 5.105). We focus on vertical velocity and temperature profiles along the line $y = 0.5$ at the symmetry plane $z = 0.5$ and overall Nusselt number ($\mathrm{Nu}_{\mathrm{overall}}$) of the heated surface $x = 1.0$. Dimensionless numbers used are $\mathrm{Ra} = 10^4$ and $\mathrm{Pr} = 1.0$. Figures 5.115, 5.119 and 5.123 show the effect of change in a, n, λ_{CY} on vertical velocity v_y along the line $y = 0.5$ on the symmetric plane ($z = 0.5$) of cavity, respectively. Figures 5.116, 5.120 and 5.124 show the viscosity curves with respect to shear rate in the fluid domain for various values of a, n and λ_{CY}. Effect of change in a, n, λ_{CY} on temperature θ along the line $y = 0.5$ on the symmetric plane ($z = 0.5$) of cavity are plotted in Figures 5.117, 5.121 and 5.125, respectively. Figures 5.116, 5.120 and 5.124 present the overall Nusselt number of heated surface $x = 1.0$ with respect to a, n, λ_{CY}, respectively. In Figure 5.116, decreasing the shape parameter a (with $n = 0.5$, $\lambda_{CY} = 1.0$) makes the viscosity decreased with changing the curve shape. Since fluid with lower viscosity is less resistant to the applied buoyancy force, it becomes more attached to the wall as a decreases (Figure 5.115). The variation in a also affects the heat transfer rate. For the temperature profiles at the line at $y = 0.5$ on the symmetry plane ($z = 0.5$) of Figure 5.117, temperature gradient at the surfaces $x = 0.0$ and $x = 1.0$ increases with decreasing a and so the heat flux at the surface increase as a decreases. The overall Nusselt number ($\mathrm{Nu}_{\mathrm{overall}}$) of the heated surface $x = 1.0$ in Figure 5.118 also tells that heat transfer rate becomes higher for lower a. The $\mathrm{Nu}_{\mathrm{overall}}$ of the surface $x = 0.0$ has the same value with that of the surface $x = 1.0$. As the power index n decreases (with $a = 2.0$, $\lambda_{CY} = 1.0$), viscosity decreases with changing its slope (see Figure 5.120). Because fluid with lower viscosity is less resistant to the applied buoyancy force, fluid with lower n is more attached to the wall as shown in Figure 5.119. By decreasing n, temperature profile at the line $y = 0.5$ at the symmetry plane has higher temperature gradient at the surfaces ($x = 0.0$ and $x = 1.0$) as in Figure 5.121. Thus the heat flux at the surface increases with decreasing n, as the plot of $\mathrm{Nu}_{\mathrm{overall}}$ with respect to n shows (Figure 5.122). As λ_{CY} increases (with

$a = 2.0$, $n = 0.5$), viscosity decreases with shifting the curves (Figure 5.124). So, the fluid with higher λ_{CY} is more attached to the wall as shown in Figure 5.123. In Figure 5.125, temperature gradient at the surfaces increases with increasing λ_{CY}, and thus higher λ_{CY} makes the heat flux at the surface increased as $\mathrm{Nu}_{\mathrm{overall}}$ changed by λ_{CY} shows (Figure 5.126).

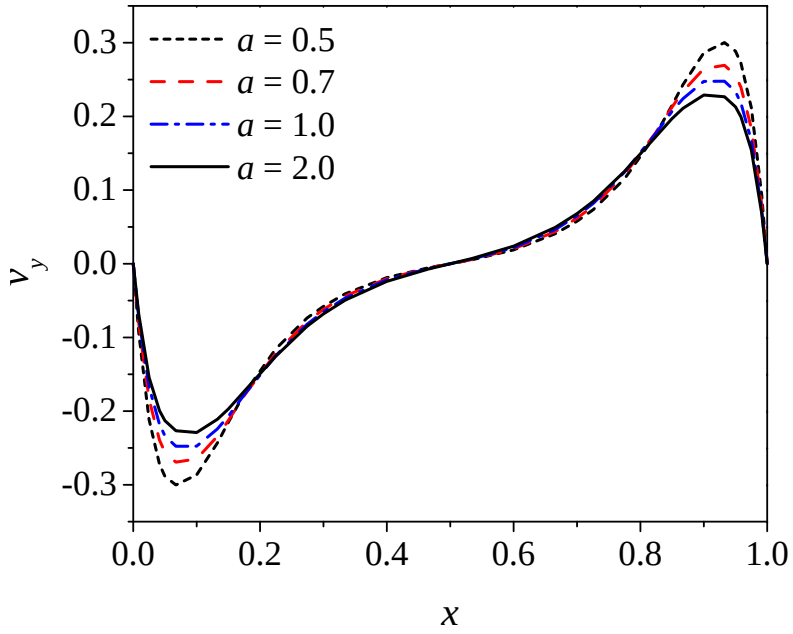

Figure 5.115: Effect of the parameter a on vertical velocity v_y along the line $y = 0.5$ on the symmetric plane ($z = 0.5$) of the cavity ($\mathrm{Ra} = 10^4$, $\mathrm{Pr} = 1.0$, $n = 0.5$, $\lambda_{CY} = 1.0$).

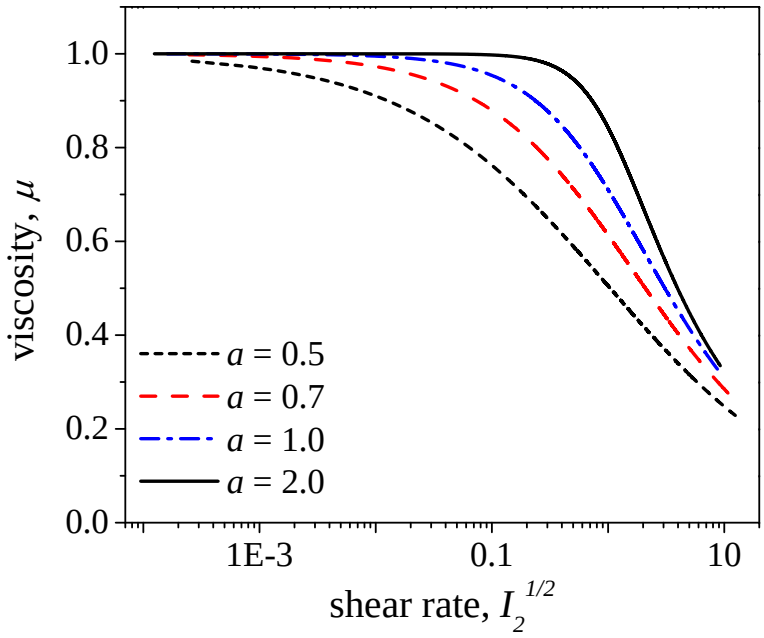

Figure 5.116: Effect of the parameter a on viscosity (Ra $= 10^4$, Pr $= 1.0$, $n = 0.5$, $\lambda_{CY} = 1.0$).

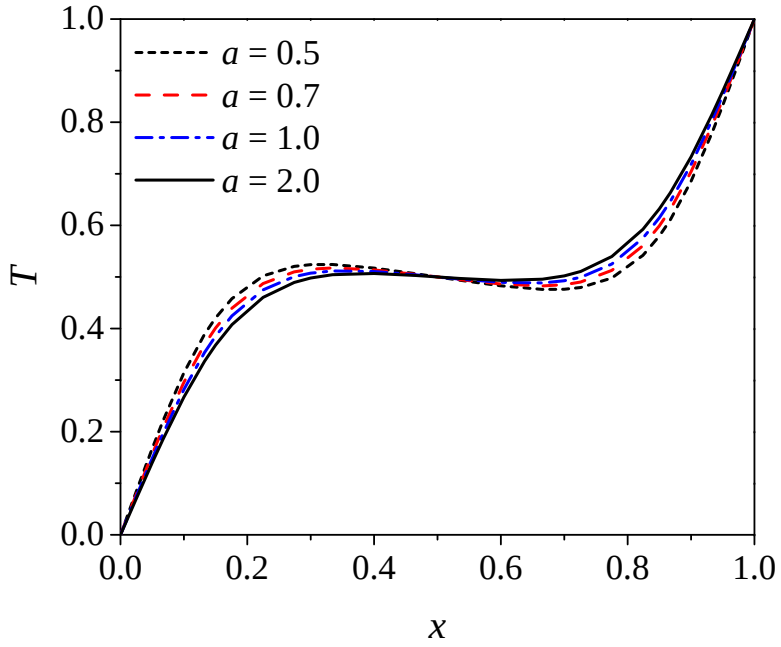

Figure 5.117: Effect of the parameter a on temperature θ along the line $y = 0.5$ on the symmetric plane ($z = 0.5$) of the cavity (Ra $= 10^4$, Pr $= 1.0$, $n = 0.5$, $\lambda_{CY} = 1.0$).

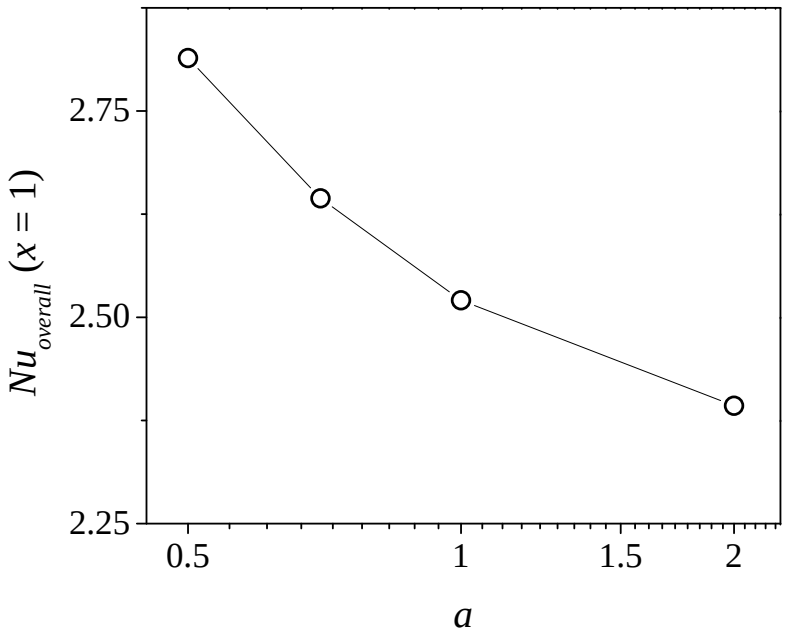

Figure 5.118: Effect of the parameter a on overall Nusselt number of heated surface $x = 1.0$ (Ra $= 10^4$, Pr $= 1.0$, $n = 0.5$, $\lambda_{CY} = 1.0$).

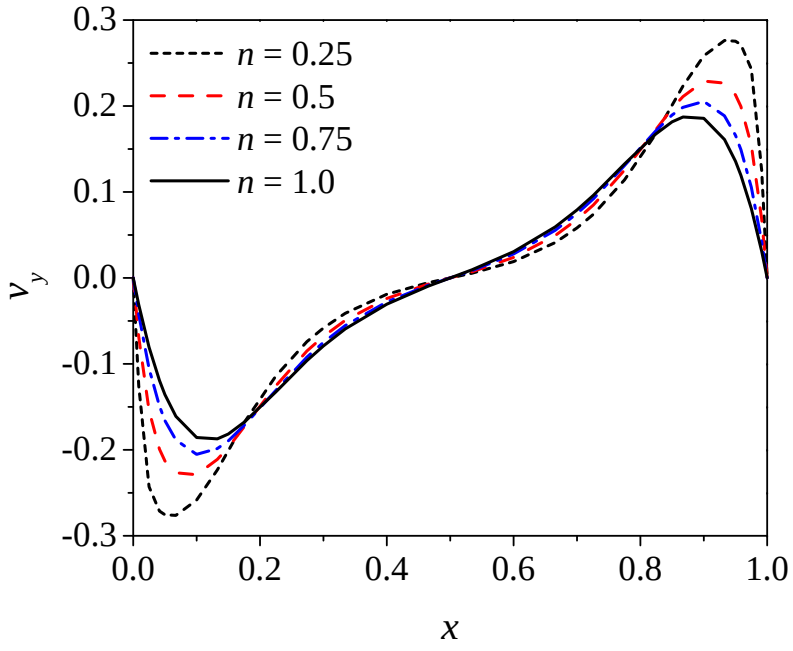

Figure 5.119: Effect of the parameter n on vertical velocity v_y along the line $y = 0.5$ on the symmetric plane ($z = 0.5$) of the cavity (Ra $= 10^4$, Pr $= 1.0$, $a = 2.0$, $\lambda_{CY} = 1.0$).

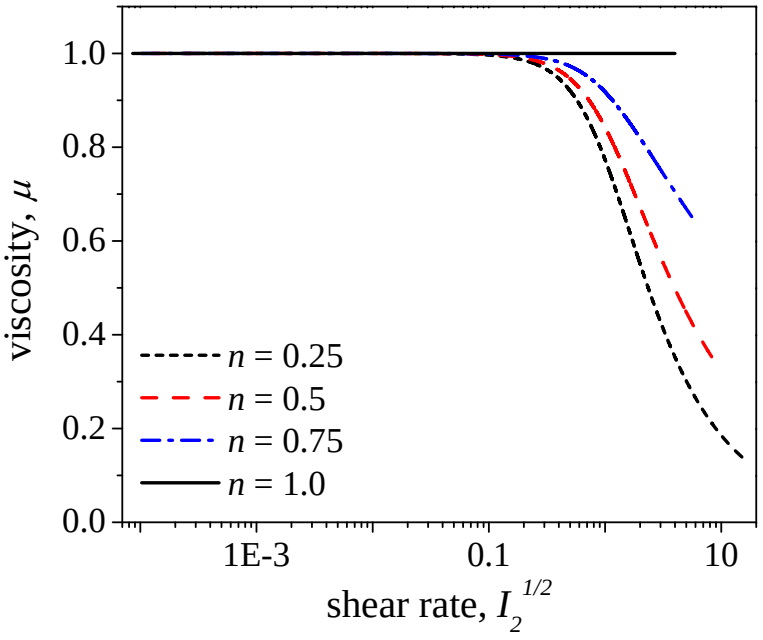

Figure 5.120: Effect of the parameter n on viscosity (Ra $= 10^4$, Pr $= 1.0$, $a = 2.0$, $\lambda_{CY} = 1.0$).

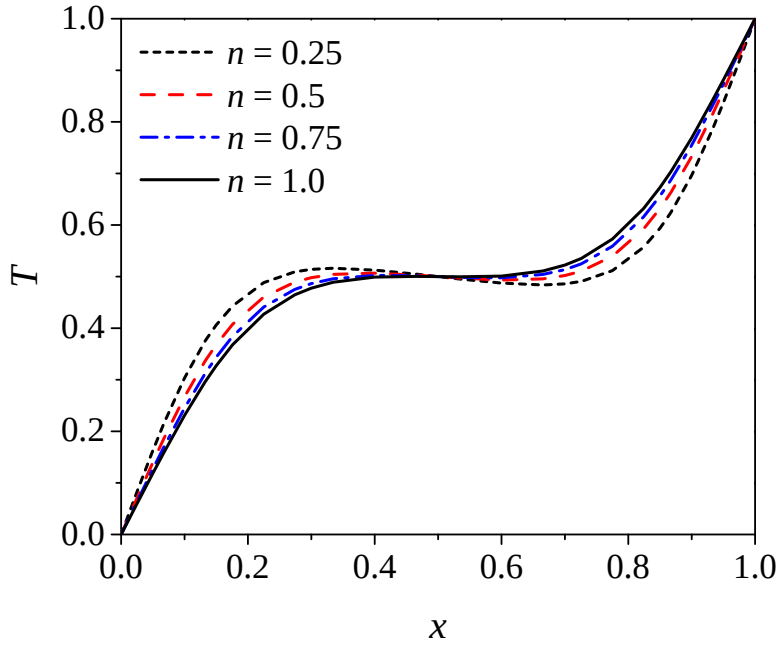

Figure 5.121: Effect of the parameter n on temperature θ along the line $y = 0.5$ on the symmetric plane ($z = 0.5$) of the cavity (Ra $= 10^4$, Pr $= 1.0$, $a = 2.0$, $\lambda_{CY} = 1.0$).

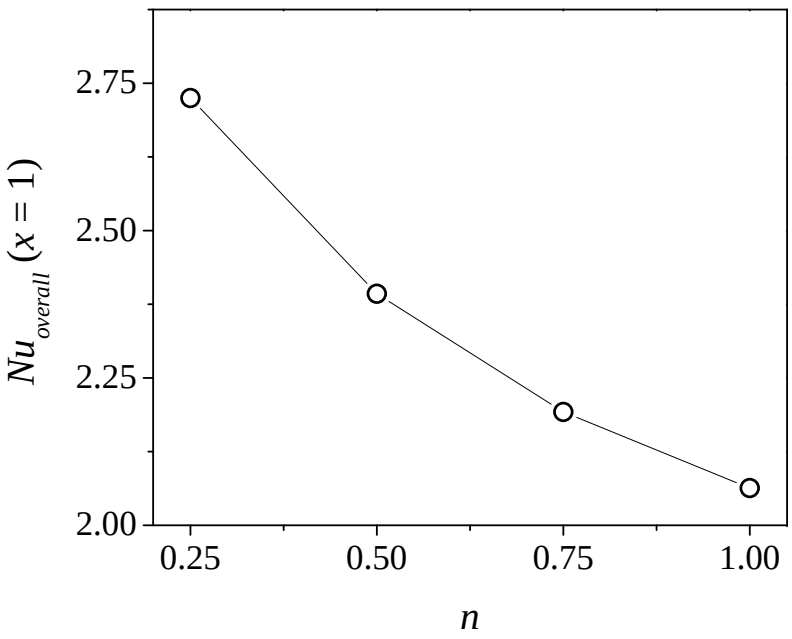

Figure 5.122: Effect of the parameter n on overall Nusselt number of heated surface $x = 1.0$ (Ra $= 10^4$, Pr $= 1.0$, $a = 2.0$, $\lambda_{CY} = 1.0$).

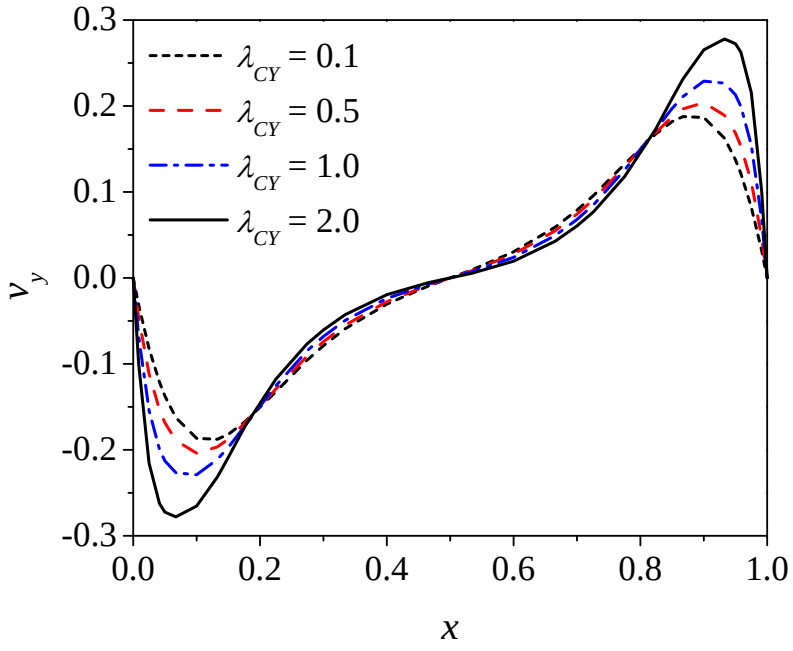

Figure 5.123: Effect of the parameter λ_{CY} on vertical velocity v_y along the line $y = 0.5$ on the symmetric plane ($z = 0.5$) of the cavity (Ra $= 10^4$, Pr $= 1.0$, $a = 2.0$, $n = 0.5$).

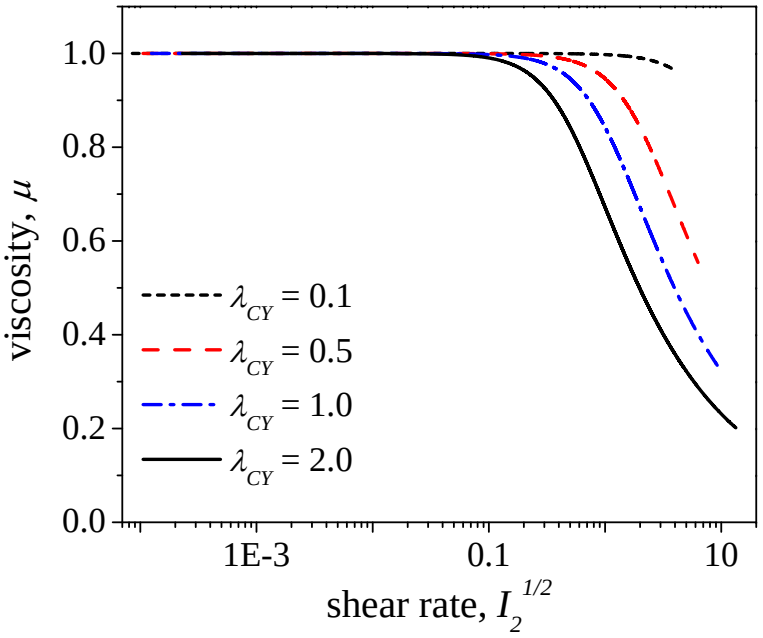

Figure 5.124: Effect of the parameter λ_{CY} on viscosity (Ra $= 10^4$, Pr $= 1.0$, $a = 2.0$, $n = 0.5$).

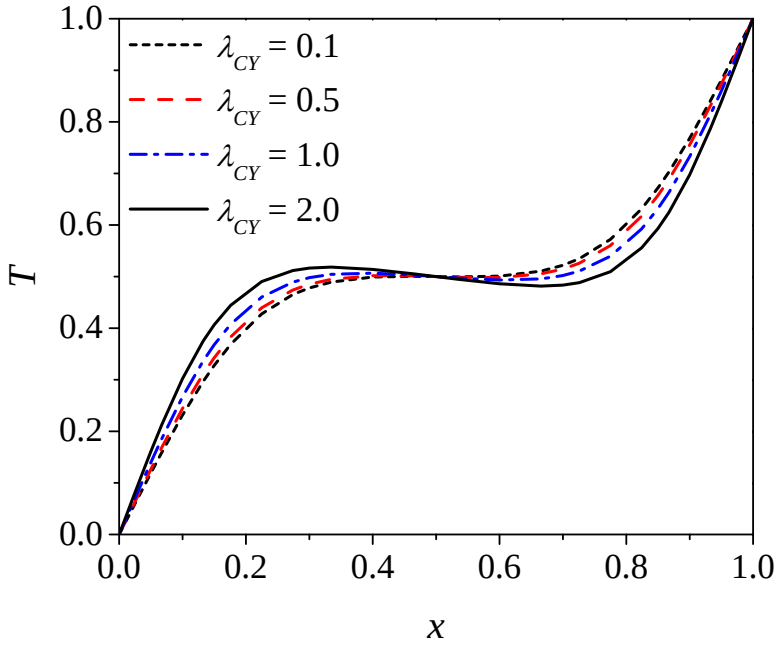

Figure 5.125: Effect of the parameter λ_{CY} on temperature θ along the line $y = 0.5$ on the symmetric plane ($z = 0.5$) of the cavity (Ra $= 10^4$, Pr $= 1.0$, $a = 2.0$, $n = 0.5$).

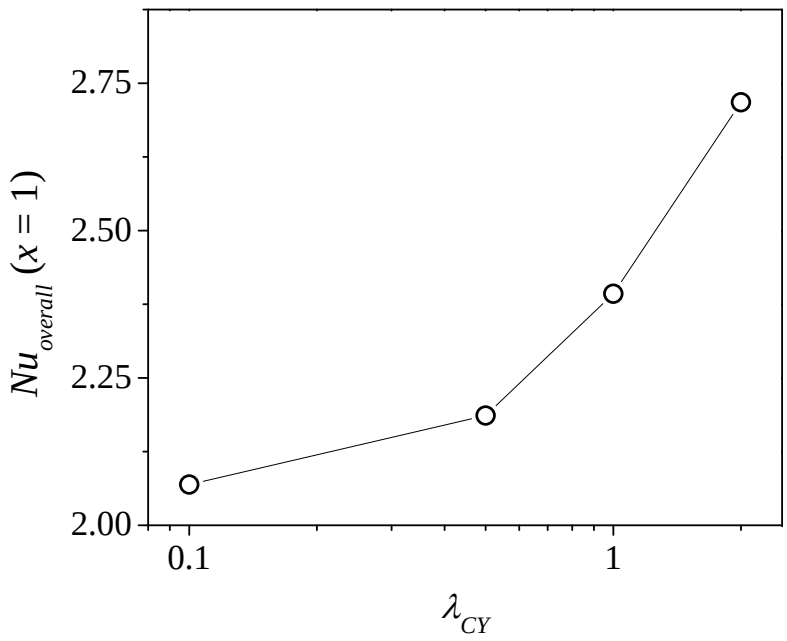

Figure 5.126: Effect of the parameter λ_{CY} on overall Nusselt number of heated surface $x = 1.0$ (Ra $= 10^4$, Pr $= 1.0$, $a = 2.0$, $n = 0.5$).

6. CONCLUSIONS *

The least-squares finite element model with high-order spectral/hp approximations has advantages over conventional weak-form Galerkin model in eliminating any type of locking (which often occurs in low-order LSFEMs of incompressible viscous fluids) and yielding accurate results with exponential convergence. In addition, since the least-squares formulation provides a variational setting for the Navier–Stokes equations, there are no compatibility restrictions placed between approximation spaces when the polynomial order used is sufficiently high (say, $\mathrm{p} > 3$, as determined numerically). We present the formulation of mixed least-squares finite element models using high-order spectral/hp approximation functions to analyze two- and three-dimensional, steady, isothermal and non-isothermal flows of generalized-Newtonian fluids where the viscosity obeys the Carreau–Yasuda constitutive model. The governing equations are recast into the equivalent first-order system of equations, using the viscous stress and heat flux as auxiliary variables. The method of manufactured solutions and several benchmark problems, namely, Kovasznay flow, Jeffery-Hamel flow in a diverging channel, flow over a backward-facing step, lid-driven cavity flow, flow past an unconfined circular cylinder, fully developed flow between parallel plates, and buoyancy-driven flow in a cavity, are considered and the results are compared with the previously known analytical, experimental and computational results. The results showed good agreement with them, thus verifying and validating the present model. The effects of the three parameters $(a,\, n,\, \lambda_{CY})$ of the Carreau–Yasuda model on the kinematics of isothermal and non-isothermal flows were also investigated. Also, we presented how the variation of each parameter $(a,\, n,\, \lambda_{CY})$ affects the flow behaviors which are linked to viscosity change with respect to shear rate.

The Carreau–Yasuda viscosity model is used to study blood flows [55–59] and polymeric flows [48–54], as mentioned earlier. For simulating blood flows, the viscosity which is independent of

*Reprinted with permission from "A spectral/hp least-squares finite element analysis of the Carreau–Yasuda fluids," by Namhee Kim and J. N. Reddy, 2016. International Journal for Numerical Methods in Fluids, Vol. 82, pp. 541–566. Copyright 2016 by John Wiley & Sons, Ltd. and from "3-D least-squares finite element analysis of flows of generalized Newtonian fluids," by Namhee Kim and J. N. Reddy, 2019. *Journal of Non-Newtonian Fluid Mechanics*, Vol. 266, pp. 143–159. Copyright 2019 by Elsevier, B.V.

temperature as in Eq. (2.5) is used, while for simulating polymeric flows, temperature-dependency is included in the viscosity model, since high temperature is required for polymer melt processing. We are interested in solving these application examples for blood and polymer melts as future works.

REFERENCES

[1] R. B. Bird, R. C. Armstrong, and O. Hassager, *Dynamics of polymeric liquids. Vol. 1: Fluid mechanics*. John Wiley & Sons, New York, NY, 1987.

[2] R. J. Krane and J. Jessee, "Some detailed field measurements for a natural convection flow in a vertical square enclosure," in *Proceedings of the First ASME-JSME Thermal Engineering Joint Conference, 1983*, vol. 1, pp. 323–329, 1983.

[3] J. N. Reddy, *An Introduction to the Finite Element Method*. McGraw-Hill New York, 4th ed., 2019.

[4] J. N. Reddy, *An Introduction to Nonlinear Finite Element Analysis: with applications to heat transfer, fluid mechanics, and solid mechanics*. Oxford University Press, 2nd ed., 2015.

[5] G. S. Payette, *Spectral/hp finite element models for fluids and structures*. Ph.D. Dissertation, Texas A&M University, 2012.

[6] T. J. R. Hughes and A. Brooks, "A multidimensional upwind scheme with no crosswind diffusion," *Finite Element Methods for Convection Dominated Flows*, vol. 34, pp. 19–35, 1979.

[7] A. N. Brooks and T. J. R. Hughes, "Streamline upwind/Petrov-Galerkin formulations for convection dominated flows with particular emphasis on the incompressible Navier-Stokes equations," *Computer Methods in Applied Mechanics and Engineering*, vol. 32, no. 1, pp. 199–259, 1982.

[8] J. N. Reddy, "Penalty-finite-element analysis of 3-D Navier-Stokes equations," *Computer Methods in Applied Mechanics and Engineering*, vol. 35, no. 1, pp. 87–106, 1982.

[9] J. N. Reddy and D. K. Gartling, *The Finite Element Method in Heat Transfer and Fluid Dynamics*. CRC press, 3rd ed., 2010.

[10] T. J. R. Hughes, L. P. Franca, and G. M. Hulbert, "A new finite element formulation for computational fluid dynamics: Viii. the Galerkin/least-squares method for advective-diffusive equations," *Computer Methods in Applied Mechanics and Engineering*, vol. 73, no. 2,

pp. 173–189, 1989.

[11] J. H. Bramble and A. H. Schatz, "Least squares methods for 2*m*th order elliptic boundary-value problems," *Mathematics of Computation*, vol. 25, no. 113, pp. 1–32, 1971.

[12] E. D. Eason, "A review of least-squares methods for solving partial differential equations," *International Journal for Numerical Methods in Engineering*, vol. 10, no. 5, pp. 1021–1046, 1976.

[13] B. N. Jiang, *The Least-squares Finite Element Method: theory and applications in computational fluid dynamics and electromagnetics*. Springer Science & Business Media, 1998.

[14] P. B. Bochev and M. D. Gunzburger, *Least-squares Finite Element Methods*, vol. 166. Springer Science & Business Media, 2009.

[15] B. N. Jiang and C. L. Chang, "Least-squares finite elements for the Stokes problem," *Computer Methods in Applied Mechanics and Engineering*, vol. 78, no. 3, pp. 297–311, 1990.

[16] B. N. Jiang and L. A. Povinelli, "Least-squares finite element method for fluid dynamics," *Computer Methods in Applied Mechanics and Engineering*, vol. 81, no. 1, pp. 13–37, 1990.

[17] B. N. Jiang, T. L. Lin, and L. A. Povinelli, "Large-scale computation of incompressible viscous flow by least-squares finite element method," *Computer Methods in Applied Mechanics and Engineering*, vol. 114, no. 3, pp. 213–231, 1994.

[18] B. N. Jiang and V. Sonnad, "Least-squares solution of incompressible Navier-Stokes equations with the p-version of finite elements," *Computational Mechanics*, vol. 15, no. 2, pp. 129–136, 1994.

[19] P. B. Bochev, Z. Cai, T. A. Manteuffel, and S. F. McCormick, "Analysis of velocity-flux first-order system least-squares principles for the Navier-Stokes equations: Part i," *SIAM Journal on Numerical Analysis*, vol. 35, no. 3, pp. 990–1009, 1998.

[20] B. N. Jiang, "On the least-squares method," *Computer Methods in Applied Mechanics and Engineering*, vol. 152, no. 1, pp. 239–257, 1998.

[21] M. M. J. Proot and M. I. Gerritsma, "A least-squares spectral element formulation for the Stokes problem," *Journal of Scientific Computing*, vol. 17, no. 1-4, pp. 285–296, 2002.

[22] M. M. J. Proot and M. I. Gerritsma, "Least-squares spectral elements applied to the Stokes problem," *Journal of Computational Physics*, vol. 181, no. 2, pp. 454–477, 2002.

[23] J. P. Pontaza and J. N. Reddy, "Spectral/hp least-squares finite element formulation for the Navier–Stokes equations," *Journal of Computational Physics*, vol. 190, no. 2, pp. 523–549, 2003.

[24] J. P. Pontaza and J. N. Reddy, "Space–time coupled spectral/hp least-squares finite element formulation for the incompressible Navier–Stokes equations," *Journal of Computational Physics*, vol. 197, no. 2, pp. 418–459, 2004.

[25] J. P. Pontaza, X. Diao, J. N. Reddy, and K. S. Surana, "Least-squares finite element models of two-dimensional compressible flows," *Finite Elements in Analysis and Design*, vol. 40, no. 5, pp. 629–644, 2004.

[26] J. P. Pontaza, "Least-squares variational principles and the finite element method: theory, formulations, and models for solid and fluid mechanics," *Finite Elements in Analysis and Design*, vol. 41, no. 7, pp. 703–728, 2005.

[27] V. Prabhakar and J. N. Reddy, "Spectral/hp penalty least-squares finite element formulation for the steady incompressible Navier–Stokes equations," *Journal of Computational Physics*, vol. 215, no. 1, pp. 274–297, 2006.

[28] M. I. Gerritsma, "Direct minimization of the discontinuous least-squares spectral element method for viscoelastic fluids," *Journal of Scientific Computing*, vol. 27, no. 1-3, pp. 245–256, 2006.

[29] V. Prabhakar and J. N. Reddy, "A stress-based least-squares finite-element model for incompressible Navier–Stokes equations," *International Journal for Numerical Methods in Fluids*, vol. 54, no. 11, pp. 1369–1385, 2007.

[30] V. Prabhakar and J. N. Reddy, "Spectral/hp penalty least-squares finite element formulation for unsteady incompressible flows," *International Journal for Numerical Methods in Fluids*, vol. 58, no. 3, pp. 287–306, 2008.

[31] V. Prabhakar, J. P. Pontaza, and J. N. Reddy, "A collocation penalty least-squares finite

element formulation for incompressible flows," *Computer Methods in Applied Mechanics and Engineering*, vol. 197, no. 6, pp. 449–463, 2008.

[32] G. S. Payette and J. N. Reddy, "On the roles of minimization and linearization in least-squares finite element models of nonlinear boundary-value problems," *Journal of Computational Physics*, vol. 230, no. 9, pp. 3589–3613, 2011.

[33] V. P. Vallala, *Higher-Order Spectral/HP Finite Element Technology for Structures and Fluid Flows*. Texas A&M University, 2013.

[34] V. P. Vallala, R. Sadr, and J. N. Reddy, "Higher order spectral/hp finite element models of the Navier–Stokes equations," *International Journal of Computational Fluid Dynamics*, vol. 28, no. 1-2, pp. 16–30, 2014.

[35] C. L. Chang and J. J. Nelson, "Least-squares finite element method for the Stokes problem with zero residual of mass conservation," *SIAM Journal on Numerical Analysis*, vol. 34, no. 2, pp. 480–489, 1997.

[36] M. M. J. Proot and M. I. Gerritsma, "Mass-and momentum conservation of the least-squares spectral element method for the stokes problem," *Journal of Scientific Computing*, vol. 27, no. 1-3, pp. 389–401, 2006.

[37] J. M. Deang and M. D. Gunzburger, "Issues related to least-squares finite element methods for the stokes equations," *SIAM Journal on Scientific Computing*, vol. 20, no. 3, pp. 878–906, 1998.

[38] J. P. Pontaza, "A least-squares finite element formulation for unsteady incompressible flows with improved velocity–pressure coupling," *Journal of Computational Physics*, vol. 217, no. 2, pp. 563–588, 2006.

[39] J. J. Heys, E. Lee, T. A. Manteuffel, and S. F. McCormick, "An alternative least-squares formulation of the Navier-Stokes equations with improved mass conservation," *Journal of Computational Physics*, vol. 226, no. 1, pp. 994–1006, 2007.

[40] P. B. Bochev and M. D. Gunzburger, "Finite element methods of least-squares type," *SIAM review*, vol. 40, no. 4, pp. 789–837, 1998.

[41] B. C. Bell and K. S. Surana, "A space–time coupled p-version least-squares finite element formulation for unsteady fluid dynamics problems," *International Journal for Numerical Methods in Engineering*, vol. 37, no. 20, pp. 3545–3569, 1994.

[42] B. C. Bell and K. S. Surana, "A space-time coupled p-version least squares finite element formulation for unsteady two-dimensional Navier-Stokes equations," *International Journal for Numerical Methods in Engineering*, vol. 39, no. 15, pp. 2593–2618, 1996.

[43] K. S. Surana and J. S. Sandhu, "Investigation of diffusion in p-version LSFE and STLSF formulations," *Computational Mechanics*, vol. 16, no. 3, pp. 151–169, 1995.

[44] N. Kim and J. N. Reddy, "A spectral/hp least-squares finite element analysis of the Carreau–Yasuda fluids," *International Journal for Numerical Methods in Fluids*, vol. 82, no. 9, pp. 541–566, 2016.

[45] A. T. Patera, "A spectral element method for fluid dynamics: laminar flow in a channel expansion," *Journal of Computational Physics*, vol. 54, no. 3, pp. 468–488, 1984.

[46] G. E. Karniadakis and S. J. Sherwin, *Spectral/hp element methods for computational fluid dynamics*. Oxford University Press, 2nd ed., 2013.

[47] M. O. Deville, P. F. Fischer, and E. H. Mund, *High-order methods for incompressible fluid flow*, vol. 9. Cambridge University Press, 2002.

[48] J. Aho and S. Syrjälä, "On the measurement and modeling of viscosity of polymers at low temperatures," *Polymer Testing*, vol. 27, no. 1, pp. 35–40, 2008.

[49] J. Aho, "Rheological characterization of polymer melts in shear and extension: measurement reliability and data for practical processing," *Tampereen teknillinen yliopisto. Julkaisu-Tampere University of Technology. Publication; 964*, 2011.

[50] T. A. L. Harris, *Design methodology, science, and technology to manufacture high temperature polymer electrolyte membranes for fuel cells*. ProQuest, 2006.

[51] T. A. L. Harris and D. Walczyk, "A study of the rheological behavior of high-temperature polymer electrolyte membrane solutions," *Journal of Applied Polymer Science*, vol. 111, no. 3, pp. 1286–1292, 2009.

[52] T. Ishikawa, S. Kihara, and K. Funatsu, "3-d non-isothermal flow field analysis and mixing performance evaluation of kneading blocks in a co-rotating twin srew extruder," *Polymer Engineering & Science*, vol. 41, no. 5, pp. 840–849, 2001.

[53] X. M. Zhang, L. F. Feng, W. X. Chen, and G. H. Hu, "Numerical simulation and experimental validation of mixing performance of kneading discs in a twin screw extruder," *Polymer Engineering & Science*, vol. 49, no. 9, pp. 1772–1783, 2009.

[54] H. Sobhani, P. D. Anderson, H. H. E. Meijer, M. H. R. Ghoreishy, and M. Razavi-Nouri, "Non-isothermal modeling of a non-newtonian fluid flow in a twin screw extruder using the fictitious domain method," *Macromolecular Theory and Simulations*, vol. 22, no. 9, pp. 462–474, 2013.

[55] F. J. H. Gijsen, F. N. van de Vosse, and J. D. Janssen, "The influence of the non-newtonian properties of blood on the flow in large arteries: steady flow in a carotid bifurcation model," *Journal of Biomechanics*, vol. 32, no. 6, pp. 601–608, 1999.

[56] F. J. H. Gijsen, E. Allanic, F. N. Van de Vosse, and J. D. Janssen, "The influence of the non-newtonian properties of blood on the flow in large arteries: unsteady flow in a 90 curved tube," *Journal of Biomechanics*, vol. 32, no. 7, pp. 705–713, 1999.

[57] J. Boyd, J. M. Buick, and S. Green, "Analysis of the Casson and Carreau-Yasuda non-Newtonian blood models in steady and oscillatory flows using the lattice Boltzmann method," *Physics of Fluids*, vol. 19, no. 9, p. 093103, 2007.

[58] D. Wang and J. Bernsdorf, "Lattice boltzmann simulation of steady non-newtonian blood flow in a 3d generic stenosis case," *Computers & Mathematics with Applications*, vol. 58, no. 5, pp. 1030–1034, 2009.

[59] J. Biasetti, F. Hussain, and T. C. Gasser, "Blood flow and coherent vortices in the normal and aneurysmatic aortas: a fluid dynamical approach to intra-luminal thrombus formation," *Journal of The Royal Society Interface*, p. rsif20110041, 2011.

[60] M. T. Schobeiri, *Fluid Mechanics for Engineers: A Graduate Textbook*. Springer Science & Business Media, 2010.

[61] K. S. Surana, M. K. Engelkemier, J. N. Reddy, and P. W. Tenpas, "k-version least squares finite element processes for 2-D generalized Newtonian fluid flows," *International Journal for Computational Methods in Engineering Science and Mechanics*, vol. 8, no. 4, pp. 243–261, 2007.

[62] R. B. Bird, W. E. Stewart, and E. N. Lightfoot, *Transport Phenomena. 2002*.

[63] A. J. Smits, *A Physical Introduction to Fluid Mechanics*. Wiley, 2000.

[64] J. N. Reddy, *An Introduction to Continuum Mechanics*. Cambridge University Press, 2nd ed., 2013.

[65] T. E. Twardowski, *Introduction to nanocomposite materials: properties, processing, characterization*. DEStech publications, Inc, 2007.

[66] F. A. Morrison, *Understanding Rheology*. Oxford University Press, 2001.

[67] H. S. Dalimunthe and K. S. Surana, "p-version least squares finite element formulation for three-dimensional, incompressible, non-isothermal, non-Newtonian fluid flow," *Computers & Structures*, vol. 58, no. 1, pp. 85–105, 1996.

[68] X. Han and X. Li, "An iterative stabilized CNBS–CG scheme for incompressible non-isothermal non-Newtonian fluid flow," *International Journal of Heat and Mass Transfer*, vol. 50, no. 5, pp. 847–856, 2007.

[69] J. C. Han, *Analytical Heat Transfer*. CRC Press, 2012.

[70] V. Prabhakar, *Least squares based finite element formulations and their applications in fluid mechanics*. PhD thesis, 2009.

[71] D. J. Tritton, *Physical fluid dynamics*. Springer Science & Business Media, 2012.

[72] T. A. Davis, "Algorithm 832: Umfpack v4.3—an unsymmetric-pattern multifrontal method," *ACM Transactions on Mathematical Software (TOMS)*, vol. 30, no. 2, pp. 196–199, 2004.

[73] T. A. Davis, "A column pre-ordering strategy for the unsymmetric-pattern multifrontal method," *ACM Transactions on Mathematical Software (TOMS)*, vol. 30, no. 2, pp. 165–195, 2004.

[74] T. A. Davis and I. S. Duff, "An unsymmetric-pattern multifrontal method for sparse lu factorization," *SIAM Journal on Matrix Analysis and Applications*, vol. 18, no. 1, pp. 140–158, 1997.

[75] T. A. Davis and I. S. Duff, "A combined unifrontal/multifrontal method for unsymmetric sparse matrices," *ACM Transactions on Mathematical Software (TOMS)*, vol. 25, no. 1, pp. 1–20, 1999.

[76] L. I. G. Kovasznay, "Laminar flow behind a two-dimensional grid," in *Mathematical Proceedings of the Cambridge Philosophical Society*, vol. 44, pp. 58–62, Cambridge Univ Press, 1948.

[77] G. B. Jeffery, "L. the two-dimensional steady motion of a viscous fluid," *The London, Edinburgh, and Dublin Philosophical Magazine and Journal of Science*, vol. 29, no. 172, pp. 455–465, 1915.

[78] G. Hamel, "Spiralförmige bewegungen zäher flüssigkeiten.," *Jahresbericht der deutschen mathematiker-vereinigung*, vol. 25, pp. 34–60, 1917.

[79] M. T. Schobeiri, "Geschwindigkeits-und temperaturverteilung in hamelscher spiralströmung," *ZAMM-Journal of Applied Mathematics and Mechanics/Zeitschrift für Angewandte Mathematik und Mechanik*, vol. 60, no. 4, pp. 195–200, 1980.

[80] M. T. Schobeiri, "The influence of curvature and pressure gradient on the flow temperature and velocity distribution," *International Journal of Mechanical Sciences*, vol. 32, no. 10, pp. 851–861, 1990.

[81] K. Millsaps and K. Pohlhausen, "Thermal distributions in jeffery-hamel flows between nonparallel plane walls," *J. Aeronaut. Sci*, vol. 20, no. 3, pp. 187–196, 1953.

[82] J. C. Heinrich and R. S. Marshall, "Viscous incompressible flow by a penalty function finite element method," *Computers & Fluids*, vol. 9, no. 1, pp. 73–83, 1981.

[83] D. K. Gartling, R. E. Nickell, and R. I. Tanner, "A finite element convergence study for accelerating flow problems," *International Journal for Numerical Methods in Engineering*, vol. 11, no. 7, pp. 1155–1174, 1977.

[84] P. E. Haines, R. E. Hewitt, and A. L. Hazel, "The jeffery–hamel similarity solution and its relation to flow in a diverging channel," *Journal of Fluid Mechanics*, vol. 687, pp. 404–430, 2011.

[85] K. Salari and P. Knupp, "Code verification by the method of manufactured solutions," tech. rep., Sandia National Labs., Albuquerque, NM (US); Sandia National Labs., Livermore, CA (US), 2000.

[86] P. N. Shankar and M. D. Deshpande, "Fluid mechanics in the driven cavity," *Annual Review of Fluid Mechanics*, vol. 32, no. 1, pp. 93–136, 2000.

[87] A. Shamekhi and K. Sadeghy, "Cavity flow simulation of Carreau–Yasuda non-Newtonian fluids using PIM meshfree method," *Applied Mathematical Modelling*, vol. 33, no. 11, pp. 4131–4145, 2009.

[88] S. Haque, I. Lashgari, F. Giannetti, and L. Brandt, "Stability of fluids with shear-dependent viscosity in the lid-driven cavity," *Journal of Non-Newtonian Fluid Mechanics*, vol. 173, pp. 49–61, 2012.

[89] E. Leriche and S. Gavrilakis, "Direct numerical simulation of the flow in a lid-driven cubical cavity," *Physics of Fluids*, vol. 12, no. 6, pp. 1363–1376, 2000.

[90] U. Ghia, K. N. Ghia, and C. T. Shin, "High-Re solutions for incompressible flow using the Navier-Stokes equations and a multigrid method," *Journal of Computational Physics*, vol. 48, no. 3, pp. 387–411, 1982.

[91] G. Biswas, M. Breuer, and F. Durst, "Backward-facing step flows for various expansion ratios at low and moderate Reynolds numbers," *Journal of Fluids Engineering*, vol. 126, no. 3, pp. 362–374, 2004.

[92] H. W. Choi and A. I. Barakat, "Numerical study of the impact of non-Newtonian blood behavior on flow over a two-dimensional backward facing step," *Biorheology*, vol. 42, no. 6, pp. 493–509, 2005.

[93] J. Kim and P. Moin, "Application of a fractional-step method to incompressible Navier-Stokes equations," *Journal of Computational Physics*, vol. 59, no. 2, pp. 308–323, 1985.

[94] A. Shamekhi, K. Sadeghy, M. Nik-Khah Bahrami, and N. Hasan, "Using mesh free method for numerical simulation of non-Newtonian fluid flow over a step," *Journal of the Society of Rheology, Japan*, vol. 36, no. 1, pp. 19–27, 2008.

[95] D. K. Gartling, "A test problem for outflow boundary conditions–flow over a backward-facing step," *International Journal for Numerical Methods in Fluids*, vol. 11, no. 7, pp. 953–967, 1990.

[96] B. F. Armaly, F. Durst, J. C. F. Pereira, and B. Schönung, "Experimental and theoretical investigation of backward-facing step flow," *Journal of Fluid Mechanics*, vol. 127, pp. 473–496, 1983.

[97] P. T. Williams and A. J. Baker, "Incompressible computational fluid dynamics and the continuity constraint method for the three-dimensional Navier-Stokes equations," *Numerical Heat Transfer*, vol. 29, no. 2, pp. 137–273, 1996.

[98] R. D. Blevins, *Flow-induced vibration*. New York, NY, Van Nostrand Reinhold Co., Inc., 1977.

[99] N. Kim and J. N. Reddy, "Least-squares finite element analysis of flow of a generalized Newtonian fluid past a circular cylinder," *Mechanics of Advanced Materials and Structures*, vol. 25, no. 14, pp. 1186–1196, 2018.

[100] I. Lashgari, J. O. Pralits, F. Giannetti, and L. Brandt, "First instability of the flow of shear-thinning and shear-thickening fluids past a circular cylinder," *Journal of Fluid Mechanics*, vol. 701, pp. 201–227, 2012.

[101] A. S. Grove, F. H. Shair, and E. E. Petersen, "An experimental investigation of the steady separated flow past a circular cylinder," *Journal of Fluid Mechanics*, vol. 19, no. 01, pp. 60–80, 1964.

[102] M. Kawaguti and P. Jain, "Numerical study of a viscous fluid flow past a circular cylinder," *Journal of the Physical Society of Japan*, vol. 21, no. 10, pp. 2055–2062, 1966.

[103] T. Fusegi, J. M. Hyun, K. Kuwahara, and B. Farouk, "A numerical study of three-dimensional natural convection in a differentially heated cubical enclosure," *International*

Journal of Heat and Mass Transfer, vol. 34, no. 6, pp. 1543–1557, 1991.